66 Wissenschaftliche Berichte des Instituts für Meteorologie und Klimaforschung des Karlsruher Instituts für Technologie

GIORGIA FOSSER

Precipitation statistics from regional climate model at resolutions relevant for soil erosion

KIT Scientific Publishing

Giorgia Fosser

Precipitation statistics from regional climate model at resolutions relevant for soil erosion

Wissenschaftliche Berichte des Instituts für Meteorologie und Klimaforschung des Karlsruher Instituts für Technologie (KIT)
Band 66

Herausgeber: Prof. Dr. Ch. Kottmeier

Institut für Meteorologie und Klimaforschung
am Karlsruher Institut für Technologie (KIT)
Kaiserstr. 12, 76128 Karlsruhe

Eine Übersicht über aller bisher in dieser Schriftenreihe erschienenen Bände finden Sie am Ende des Buches.

Precipitation statistics from regional climate model at resolutions relevant for soil erosion

by
Giorgia Fosser

KIT Scientific Publishing

Dissertation, Karlsruher Institut für Technologie (KIT)
Fakultät für Bauingenieur-, Geo- und Umweltwissenschaften, 2013
Referenten: Prof. Dr. Erwin Zehe, Prof. Dr. Christoph Kottmeier

Impressum

Karlsruher Institut für Technologie (KIT)
KIT Scientific Publishing
Straße am Forum 2
D-76131 Karlsruhe

www.ksp.kit.edu

Print on Demand 2014

ISSN 0179-5619
ISBN 978-3-7315-0227-2
DOI: 10.5445/KSP/1000041271

Precipitation statistics from regional climate model at resolutions relevant for soil erosion

Zur Erlangung des akademischen Grades einer
DOKTOR-INGENIEURIN
von der Fakultät für
Bauingenieur-, Geo- und Umweltwissenschaften

des Karlsruher Instituts für Technologie (KIT)
genehmigte
DISSERTATION

von
Ing. Giorgia Fosser
aus Padova (Italien)

Tag der mündlichen Prüfung: 21.11.2013
Referent: Prof. Dr. Erwin Zehe
Korreferent: Prof. Dr. Christoph Kottmeier

Karlsruhe 2013

Abstract

Climate change is an unequivocal reality that policy makers need to take into account for their future adaptation strategies. Regional climate models (RCMs) are often used to bridge the gap between GCMs resolution and effective adaptation strategies at national level. However, most RCMs at coarse resolution fail in representing convective precipitation, which is responsible for some of the most damaging weather phenomena like heavy rainfall, large hail, and tornadoes. The parameterisation of convection is known to be a major source of uncertainty and often blamed for the misrepresentation of the diurnal cycle of summer precipitation. Convection-permitting scale defines a spatial resolution below 3 km, which gives the possibility to switch off a major part of the convective parameterisations. Several studies prove the benefits of this spatial scale, particularly in the case of moist convection and/or for regions with strong orography, but none of them is available on climatological time-scale (i.e. 30 years).

This research bridges the gap between the numerical weather forecast (NWP) knowledge on convection-permitting scale and real climate scale. In this context, 30-year simulations are performed with the RCM COSMO-CLM, driven first with ERA40 reanalysis data and then with ECHAM5 for the recent past (1971-2000) and near future (2021-2050). A triple nesting strategy is used to reach 2.8 km resolution from the GCM resolution. The investigation area is located around the Weiherbach catchment, in the north-western part of Baden-Württemberg in southwestern Germany. Here, the Deutsche Wetterdienst (DWD) operates a dense network of high temporal resolution rain gauge stations, which is used together with the HYRAS dataset for the validation of the model performances.

The study, first determines the added value of higher resolution versus coarser resolution using the ERA 40 simulations. In particular, the analysis examines the differences between resolutions in the representation of precipitation statistics and the atmospheric conditions leading to convection. The investigation uses probability distributions on both daily and hourly bases as well as event-based analysis. Diurnal cycles, instability of the atmosphere and vertical profiles of temperature and humidity as well as cloud cover, radiation budget and triggering mechanisms, are all considered in evaluating the status of the atmosphere. The results show that the convection-permitting scale reduces the drizzle problem affecting coarser resolutions, and better represents the hourly intensity distribution as well as the diurnal cycle of precipitation. Moreover, the convection parameterisation seems to cause a detachment between the boundary layer conditions and the occurrence of convection, while this connection is maintained at higher resolution. These findings imply a large improvement in the physical consistency of precipitation at convection-permitting scale. Moreover, the improved representation of the hourly precipitation statistics has a high value not only within the scientific community but also for many impact assessment models, which need both high spatial and temporal resolution (e.g. soil erosion models). On the other hand, the model, especially at higher resolution, tends to surround the events with low intensity precipitation above 0.1 mm/h. This leads to a strong overestimation of higher intensities on daily basis.

In the second part, the study investigates the climate change signal at both convection-permitting and coarser spatial scale using ECHAM5 driven simulations to determine if higher resolution can provide more reliable information on the expected changes in precipitation. The most interesting findings are found in summer, when the simulations project an increase of higher precipitation intensities on daily but not on hourly bases. Event-based

analysis has proved to be a good methodology to bridge the large temporal gap between daily and hourly resolution. In this context, convection-permitting simulations project a decrease in the number of short events with low intensities and an increase in those lasting between 10 and 20 hours with intensities between 20 and 90 mm/event. Moreover, events longer than 30 hours as well as the total number of events will reduce substantially in the near future in good agreement with the increase in the length and frequency of the dry periods. The diurnal cycles of precipitation calculated for different precipitation thresholds show an increase in the morning precipitation, probably linked to an intensification of large-scale weather patterns in the near future. The analysis also projects no relevant changes or even a decrease in convective precipitation. Both resolutions provide similar results in terms of climate change signal and relative magnitude of the changes. Differences in absolutes values and in the representation of the diurnal cycle of precipitation, CAPE and cloud cover are due to the possibility to resolve convection at 2.8 km and not to a different climate change signal between resolutions. However, having the diurnal cycle of precipitation correctly represented for the right reasons makes convection-permitting scale more reliable for investigating the climate change signal and in general should be the way to follow in regional climate modelling.

Zusammenfassung

Der Klimawandel ist eine nicht zu leugnende Tatsache, die von politischen Entscheidungsträgern für die Entwicklung zukünftiger Anpassungsstrategien berücksichtigt werden muss. Regionale Klimamodelle (RCMs) werden dabei oft dazu verwendet die Lücke, zwischen der Auflösung globaler Klimamodelle (GCMs) und den Anforderungen regionaler Planungen, zu schließen. Den meisten RCMs gelingt es allerdings nicht konvektive Niederschläge, welche für einige der schadensreichsten Wetterphänomene, wie Starkniederschläge, Hagel und Tornados, verantwortlich sind, zufriedenstellend abzubilden. Die Konvektionsparametrisierung ist dabei ein Hauptgrund für Unsicherheiten in den Modellergebnissen und in hohem Maße dafür verantwortlich, dass der Tagesgang sommerlicher Niederschläge nicht korrekt wiedergeben werden kann. Bei räumlichen Auflösungen unter 3 km kann ein Großteil dieser Konvektionsparametrisierung ausgeschaltet werden. Diesen Skalenbereich nennt man Wolken-auflösend oder Konvektions-erlaubend. Die Ergebnisse verschiedener Studien zeigen dabei den Mehrwert dieser räumlichen Auflösung für feuchte Konvektion und/oder Regionen mit hoher Orographie. Derartige Studien existieren allerdings nicht auf einer klimatologischen Zeitskala.

In dieser Arbeit werden die Erkenntnisse aus der numerischen Wettervorhersage (NWP) über die Wolken-auflösende Skala auf Klimasimulationen übertragen. In diesem Zusammenhang werden 30 jährige Simulationen mit dem RCM COSMO-CLM durchgeführt, die zuerst durch ERA40 Reanalysen und danach mit ECHAM5 für die Zeiträume 1971-2000 und 2021-2050, angetrieben werden. Die globalen Antriebsdaten werden dabei durch ein dreifaches Nesting auf eine 2,8 km Auflösung dynamisch regionalisiert. Das Untersuchungsgebiet umfasst das Weiherbach-Einzugsgebiet im Nordwesten Baden-Württembergs, im Südwesten Deutschlands. Der Deutsche Wetterdienst

(DWD) betreibt hier ein dichtes, zeitlich hochaufgelöstes Regenmessnetz. Die dort gemessenen Daten wurden zusammen mit dem HYRAS Datensatz zur Validierung des Modells verwendet.

Innerhalb der vorliegenden Arbeit wurde zunächst der Mehrwert einer höheren Auflösung im Vergleich zu einer gröberen, anhand der ERA40 Simulationen, bestimmt. Ein besonderes Augenmerk der Analysen lag dabei auf den Auswirkungen die unterschiedliche Auflösungen auf die Niederschlagsstatistik und die atmosphärischen Bedingungen haben die Konvektion auslösen. Für diese Untersuchungen wurden Wahrscheinlichkeitsverteilungen auf stündlicher und täglicher Basis, sowie ereignisbezogene Analysen, verwendet. Zur Untersuchung des Atmosphärenzustands wurden der Tagesgang, die Instabilität der Atmosphäre, Vertikalprofile der Temperatur und der Feuchte, die Wolkenbedeckung, die Strahlungsbilanz und Auslösermechanismen, berücksichtigt.

Die Ergebnisse zeigen dabei, dass auf der Wolken-auflösenden Skala das Problem des Nieselregens, wie es bei gröberen Auflösungen auftritt, reduziert wird. Darüber hinaus wird die stündliche Intensitätsverteilung des Niederschlags sowie dessen Tagesgang besser dargestellt. Des Weiteren scheint durch die Konvektionsparametrisierung kein Zusammenhang mehr zwischen den Grenzschichtbedingungen und dem Auftreten von Konvektion zu bestehen. Bei einer höheren Auflösung ist diese Beziehung allerdings klar zu erkennen. Dies führt zu dem Schluss, dass auf der Wolken-auflösenden Skala mit hoher zeitlicher Auflösung eine deutliche Verbesserung innerhalb der physikalischen Konsistenz des Niederschlages erreicht wird, was nicht nur für die regionale Modellierung von großer Bedeutung ist, sondern auch für die regionale Planung. Andererseits neigt das Model dazu, besonders bei höheren Auflösungen, Niederschlagsereignisse mit geringen Intensitäten (0,1 mm/h) zu verstärken. Dies führt zu einer starken Überschätzung der hohen

Intensitäten auf täglicher Basis. Zudem werden auf der Wolken-auflösenden Skala die Anzahl der Trockentage im Winter weiterhin deutlich unterschätzt.

Im zweiten Teil der Arbeit wurde, anhand von ECHAM5 angetriebenen Simulationen, untersucht wie gut sowohl die Wolken-auflösende, als auch gröbere Auflösungen, in der Lage sind den Klimatrend wiederzugeben. Bei beiden Auflösungen wurden ähnliche Ergebnisse bezüglich der Veränderung der relativen Niederschlagsstatistik erzielt. Besonders interessant war dabei das Verhalten in den Sommermonaten, wo die Simulationen einen Anstieg in den hohen Niederschlagsintensitäten auf täglicher Basis, aber nicht auf stündlicher simulierten. Ereignisbezogene Analysen sind dabei nachgewiesenermaßen eine Gute Methode um die zeitliche Lücke zwischen der täglichen und der stündlichen Auflösung zu schließen. In diesem Zusammenhang projizierten Wolken-auflösende Simulationen einen Rückgang der kurzen Ereignisse mit geringen Intensitäten und einen Anstieg derer die zwischen 10 und 20 Stunden andauern und dabei eine Intensität von 20 bis 90 mm/Ereignis aufweisen. Darüber hinaus ergab sich, dass sich Ereignisse die länger als 30 Stunden andauern wie auch die Gesamtzahl der Ereignisse, in Zukunft deutlich verringern werden. Dies geht mit einer Zunahme der Dauer und der Frequenz von Trockenperioden einher. Der Tagesgang des Niederschlages, berechnet für unterschiedliche Niederschlagsgrenzwerte, zeigt einen Anstieg in den morgendlichen Niederschlägen an, was sehr wahrscheinlich mit einer Intensivierung großskaliger Wetterprozesse in naher Zukunft zusammen hängt. Die Analysen zeigen des Weiteren keine bedeutenden Veränderungen in den konvektiven Niederschlägen auf. In einigen Fällen ist eine Abnahme zu erkennen.

Contents

List of figures

List of tables

1. Introduction

According to the Fifth Assessment Report (AR5) of the Intergovernmental Panel on Climate Change (IPCC), climate change is an unequivocal reality that policy makers need to take into account for their future planning (IPCC 2013). Besides a global warming of at least 0.2 K per decade, AR5 global circulation models (GCMs) predict a precipitation increase in winter in Northern Europe and a decrease in Southern Europe for the future summers of the 21st century. However, these climate projections present high uncertainties for Central Europe where the models disagree on both distribution and magnitude of the climate change signals (Christensen et al. 2007). Moreover, GCMs have a typical spatial resolution of more than 100 km, which is too coarse to develop an effective adaptation strategy at national level.

Regional climate models (RCMs) give the possibility of increased spatial resolution and provide better insight into the future climate in Europe, especially in summer when the climate change signal for precipitation is more heterogeneous (Déqué et al. 2007; Feldmann et al. 2012; Wagner et al. 2012). For southwestern Germany, RCMs simulations agree on a future increase in the more intense events and a decrease in light and moderate precipitation (Boberg et al. 2010; Boberg et al. 2009; Feldmann et al. 2012; Wagner et al. 2012). In the same area, the number of dry days and dry periods are projected to increase by + 20% on annual scale (Wagner et al. 2012), in line with the trend over western and central Europe (Giorgi et al. 2004).

The total amount of the precipitation, its intensities and the alternation of dry and wet periods are the main direct reasons for changes in soil erosion rates (e.g. Favis-Mortlock and Savabi 1996). A climate scenario with more frequent and heavier precipitation on a drier soil is likely to enhance soil erosion. This process reduces the fertility of the land and thus its agricultural

productivity, causing economic loss. In this context, the KLIWA (Klimaveränderung und Konsequenzen für die Wasserwirtschaft) project "Bodenabtrag durch Wassererosion in Folge von Klimaveränderungen" has been established with the idea of coupling RCMs with soil erosion models in order to investigate how erosion will be modified under climate change in the south of Germany. In general, impact assessment models, e.g. hydrological river catchment models, require meteorological forcing data with high spatial resolution. In particular, soil erosion occurs on a scale of a few 100 metres and with temporal scales of minutes to hours. For an effective coupling of atmospheric and soil processes, erosion models need meteorological forcing data with high temporal and spatial resolution (Michael et al. 2005).

From a RCMs point of view, increasing horizontal resolution not only enables a more detailed representation of topographical and land use features but may also lead to better results in simulating extreme events (Giorgi 2006), spatial patterns and intensity distributions of precipitation (Boberg et al. 2010). Moreover, recent studies start recognizing the importance of also increasing the temporal resolution for a correct interpretation of precipitation statistics, especially in evaluating convective events (Berg et al. 2013; Haerter et al. 2010; Haerter and Berg 2009; Lenderink and van Meijgaard 2008).

Deep moist convection acts mainly in summer and is responsible for some of the most damaging weather phenomena such as heavy rainfall, large hail, damaging wind gusts, and tornadoes. In southwestern Germany, severe convection events causing hail damages increased between 1974 and 2003 (Kunz et al. 2009). At coarser resolution (i.e. spatial resolution above 3 km) most RCMs struggle to correctly represent convective precipitation, which usually occurs too early in the day and with overestimated amplitude of its diurnal cycle (Brockhaus et al. 2008; Dai 2006; Dai and Trenberth 2004; Yang

and Slingo 2001). The reasons behind this seem to be related to the model parameterisation of convection. Deep convection acts on a scale of only a few kilometres, while the typical grid resolution for RCMs simulations ranges between 5 and 50 km. Thus, on one hand, RCMs need a parameterisation to represent convection; on the other, the parameterisation is recognized as a major source of uncertainties and it is often blamed for the misrepresentation of the diurnal cycle of summer precipitation (Bechtold et al. 2004; Brockhaus et al. 2008; Hohenegger et al. 2008).

Convection-permitting scale defines a spatial resolution below 3 km, which gives the possibility of switching off a major part of the convective parameterisations. Several studies prove the benefits of this spatial scale in the representation of the precipitation field, mainly when moist convection and/or regions with strong orography are involved (Baldauf et al. 2011; Grell et al. 2000; Hohenegger et al. 2008; Mass et al. 2002; Miura et al. 2007; Richard et al. 2007; Roberts and Lean 2008; Schwartz et al. 2009; Weusthoff et al. 2010). Moreover, Giorgi et al. (2004) underlined the importance of the models' internal physics and resolution in predicting climate changes in summer when convection becomes dominant.

At the moment, simulations at convective-permitting scale are limited to numerical weather prediction (NWP) or to shorter periods of up to a season. This strongly limits the possibility of reaching sound conclusions on the added value of higher resolution since improvements due to a better resolved land–atmosphere interaction might not appear in short time scale (Prein et al. 2013). Moreover, long-term simulations are necessary to separate anthropogenic climate change from natural variability and to obtain robust findings on the climate change signal. Additionally, longer datasets allow reliable statistical analysis. Research performed for this thesis aims to bridge the gap between the NWP knowledge on convection-permitting scale and

real climate time scale (i.e. 30 years). This would have a great value not only within the scientific community, but especially at a policy-makers level (as in the case of this KLIWA project). In fact, meteorological data in higher spatial and temporal resolution are requested more and more frequently as input for impact assessment models, e.g. in soil erosion modelling or urban drainage planning.

In this context, long-term simulations are performed using COSMO-CLM (COnsortium for Small scale Modelling model—in Climate Limited Area Model, here abbreviated CLM) model. This is a non-hydrostatic local area model, whose dynamic core was originally created by the German weather service (i.e. Deutscher Wetterdienst , DWD) for weather prediction (Steppeler et al. 2003). COSMO-CLM has been developed as an initiative of an international research consortium and is now widely used for climatological studies (e.g. Berg et al. 2012; Feldmann et al. 2012; Meißner et al. 2009; Wagner et al. 2012). Two spatial resolutions simulations are considered in this study: convection-permitting (i.e. 2.8 km resolution) and a coarser scale, namely 7 km. Besides understanding whether higher spatial resolution can lead to some benefits, it is also important to evaluate if these possible added-values compensate for its high computational cost.

In particular, this thesis has the following objectives:

1. Define the optimum model domain and setup to run long-term simulations at convection-permitting scale on the state of Baden-Württemberg in southwest Germany.

The purpose is to verify how sensitive the model results at this resolution are to changes in the simulation domain and in the internal settings. These sensitivity studies are important to estimate the reliability of the results compared to observations. Vidale et al. (2003) underline the risk of compensating model errors related to the parameterisation, which can lead in some

cases to good results for the wrong reason. Meißner et al. (2009) found that leaving out the Alps in simulating Germany at 7 km resolution leads to an unrealistic increase in precipitation. While coarser resolution was widely tested for both size and location of the simulation domain as well as for the optimisation of the internal setup (Berg et al. 2012; Meißner et al. 2009; Meißner 2008), nothing is known for convection-permitting scale modelling in climate mode for this region.

2. Investigate the added value of convection-permitting scale compared to coarser resolution in the representation of precipitation statistics at subdaily timescale and of the atmospheric conditions leading to convection.

For weather prediction, switching off the parameterisation of convection seems to lead to a better representation of the diurnal cycle of precipitation, especially in summer, when convective processes are dominant (Baldauf et al. 2011; Hohenegger et al. 2008; Prein et al, 2013). Nevertheless, it is not clear yet to which extent this improvement is related to the parameterisation or to the increase in spatial resolution. A correct simulation of a diurnal cycle for the right reasons is important because it could allow for a better insight into expected changes in precipitation extremes of short duration (Lenderink and van Meijgaard 2008). Thus, this research investigates the atmospheric conditions leading to convection in order to understand to which extent they are consistent with the occurrence of convective activities. Recent investigations suggest increasing temporal resolution when increasing spatial resolution (Berg et al. 2012; Boberg et al. 2010; Boberg et al. 2009). Haerter et al. (2010) found that the intensity distribution change character at the hourly temporal resolution. Therefore, the analysis considers a higher temporal scale than just daily resolution.

3. Investigate the climate change signal at convection-permitting scale for the near future, i.e. 2021-2050, compared to coarser resolution.

Giorgi et al. (2004) underlined the crucial role that local physics processes and their parameterisation acquire in predicting climate change in summer. Convection-permitting scale could allow reducing the uncertainties related to the convection parameterisation and gaining more information on the precipitation changes and the reasons behind them. On the other hand, the climate change signal could become too noisy increasing the spatial resolution. Thus, the main purpose here is to determine if at convection-permitting scale a climate change signal is detectable and in line with previous findings at coarser scale. Moreover, it is important to understand if this scale can bring some additional information compared to coarser resolution and thus worth its high computational costs.

The investigation focuses on the state of Baden-Württemberg in southwest Germany. In the past, the area was selected by several campaigns studying convection, such as VERTIKATOR in 2002 (e.g. Barthlott et al. 2006) and COPS in 2007 (e.g. Kottmeier et al. 2008; Wulfmeyer at al., 2008). In fact, the characteristic topography of the region with its alternation of hills and flat areas, like the Black forest and the Rhine valley, often generates strong convective events and impacts on the precipitation distribution in the area (Kalthoff et al. 2000; Khodayar et al. 2013; Koßmann and Fiedler 2000; Meißner et al. 2007). Moreover, CLM in NWP mode has difficulties in providing satisfying precipitation forecasts for this region (e.g. Barthlott et al. 2010). Thus, southwest Germany is a challenging region to model, especially when it comes to orographically induced convective precipitation. DWD and LUBW operate a dense network of high temporal resolution rain gauge stations over the state of Baden-Württemberg, which can be used together with the HYRAS dataset (Rauthe et al. 2013) for the validation of the model.

The investigation area throughout most of this thesis is located around the Weiherbach catchment, in the north-western part of Baden-Württemberg

(Figure 1). The KLIWA project, funding this research, selected the Weiherbach catchment as one of the reference areas for soil erosion assessment modelling because of its high erosion risk and the excellent soil data availability thanks to in-depth field campaigns on soil erosion processes in the same area (e.g. Plate and Zehe 2008; Scherer 2008; Zehe et al. 2001). Erosion processes themselves are not considered in this thesis. However, model precipitation data, created within this research, were used as input for two erosion models, namely LISEM (De Roo et al. 1996) and CATFLOW-SED (Scherer 2008; Zehe et al. 2001), respectively within the KLIWA project and a Master thesis research (Antonetti 2013) I co-supervised. Thus, in this research, particular attention is given to precipitation characteristics, which could affect soil erosion (i.e. extreme precipitation and alternation of dry and wet periods). Moreover, the main implications for erosion related to the model performance are reported in the text.

Figure 1: Map of Baden-Württemberg in south-west Germany (left). The black box indicates the Weiherbach catchment that is enlarged on the right.

In the following, CLM model and its characteristics are presented in more detail (Chapter 2). Chapter 3 introduces the observational datasets used for the validation of the model simulations. The optimum simulation area and model configuration for long-term simulations at convection-permitting scale are determined in Chapter 4, while Chapter 5 investigates the added value of convection-permitting scale versus coarser resolution in the representation of the convective precipitation and atmospheric conditions leading to it. Chapter 6 compares higher with coarser resolution in terms of the climate change signal. Finally, the general conclusions and outlook are presented in Chapter 7.

2. Description of COSMO-CLM model

The COSMO model is based on the non-hydrostatic limited-area atmospheric model (formerly known as Lokal Modell, LM) developed and used by DWD since December 1999 for operational NWP. The model was designed to represent both meso-β and meso-γ scales phenomena from fronts and squall lines (i.e. 20-200 km scale) to thunderstorms and convection (i.e. 2-20 km scale). The basic model equations describe a compressible flow in a moist atmosphere in rotated geographical coordinates with a terrain-following height coordinate without any scale approximation.

In 2007, LM model was renamed COSMO to recognize the joint effort of DWD and many weather services and academic institutes in Europe, Switzerland and Russia to systematically develop and improve the model. Actually, two configuration of COSMO are run operationally by DWD: COSMO-EU comprising the whole of Europe with a 7 km spatial resolution and COSMO-DE at 2.8 km resolution covering Germany, Switzerland, Austria and partially the neighbouring countries (Figure 2).

COSMO-CLM or CCLM (COSMO model in CLimate Mode, here abbreviated as CLM) is the climate version of the model, widely employed for climatological study (e.g. Feldmann et al. 2012; Reichler and Kim 2008; Wagner et al. 2012). Note that CLM uses the same dynamics, numerics and parameterisations as COSMO in NWP mode (see following chapters for more details). For this research, CLM version 4.8 is used.

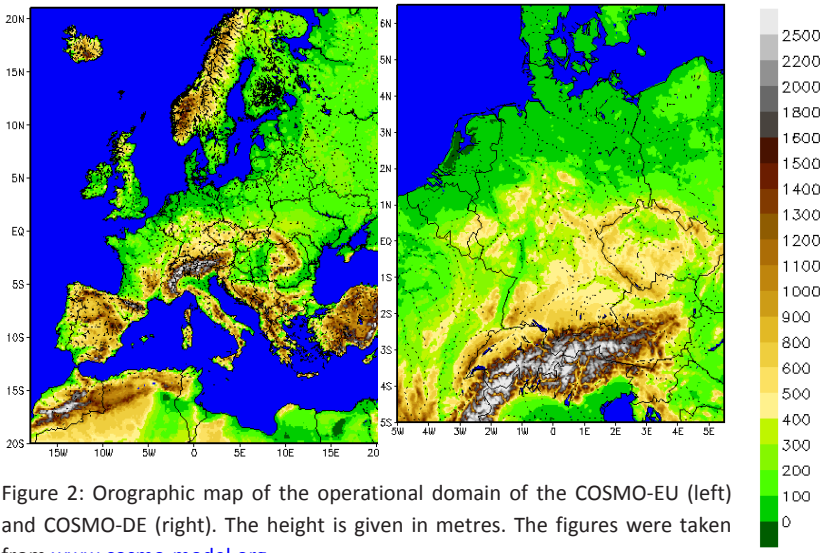

Figure 2: Orographic map of the operational domain of the COSMO-EU (left) and COSMO-DE (right). The height is given in metres. The figures were taken from www.cosmo-model.org

2.1. Model equations

The equations below and the procedure followed to reach the final equations used in the model are taken from the model description by Doms (2011), where more information can be found. The atmosphere is described by CLM as a multicomponent continuum of dry air, water vapour, liquid and solid water in ideal mixture. The basic equations of CLM consider the gravity and Coriolis forces, the conservation of heat, mass and momentum as well as phase changes of water. The budget equations are then:

$$\rho \frac{d\mathbf{v}}{dt} = -\nabla p + \rho \boldsymbol{g} - 2\boldsymbol{\Omega} \times (\rho \mathbf{v}) - \nabla \cdot \underline{\mathbf{t}}$$

$$\frac{d\rho}{dt} = -\rho \nabla \cdot \mathbf{v}$$

$$\rho \frac{dq^x}{dt} = -\nabla \cdot \mathbf{J}^x + I^x$$

$$\rho \frac{de}{dt} = -p\nabla \cdot \mathbf{v} - \nabla \cdot (\mathbf{J}_e + \mathbf{R}) + \varepsilon$$

with:	t, p, T	Time, pressure, temperature
	ρ^x	partial density of mixture constituent x
	$\rho = \sum_x \rho^x$	total density of the air mixture
	$q^x = \rho^x/\rho$	mass fraction (specific content) of constituent x
	$v = \rho^{-1}$	specific volume
	e	specific internal energy
	$h = e + pv$	specific enthalpy
	$\mathbf{v}$	barycentric velocity (relative to the rotating earth)
	I^x	sources/sinks of constituent x
	$\mathbf{J}^x$	diffusion flux of constituent x
	$\mathbf{J}_e$	diffusion flux of internal energy (heat flux)
	$\mathbf{R}$	flux density of solar and thermal radiation
	$\underline{\mathbf{t}}$	stress tensor due to viscosity
	$\varepsilon = -\underline{\mathbf{t}} \cdot\cdot \nabla\mathbf{v}$	kinetic energy dissipation due to viscosity
	$\boldsymbol{\Omega}$	constant angular velocity of earth rotation
	$\mathbf{g}$	apparent acceleration of gravity
	$\frac{d}{dt} = \frac{\partial}{\partial t} + \mathbf{v} \cdot \nabla$	total (Lagrangian) time derivative operator
	$\frac{\partial}{\partial t}$	local (Eulerian) time derivative operator
	∇	gradient (Nabla) operator

The index *x* represents the specific constituent of the mixture, namely *d* for dry air, *v* for water vapour, *l* for liquid water and *f* for ice. Bold symbols indicate vectors and bold underlined symbols dyadic tensors. Scalar and vector products are indicated by · and × respectively.

The above equations need to be modified and simplified to arrive at numerically solvable equations. The procedure is complex and is just quickly summarised in the following. More details can be found in Doms (2011). First the equations are defined in terms of differential operators through the budget operator $\partial(\rho..)/\partial t + \nabla \cdot (\rho \mathbf{v})$, since the total mass is conserved. The thus-obtained equations are averaged over the specific grid box and time step.

The meteorological variables are then divided in a mean value (called grid scale value) and in the deviation from the mean value (called subgrid scale perturbation). The former represents the slow and resolvable part of the flow while the latter needs a parameterisation to be formulated in terms of the grid scale variables and incorporated in the budget equations. Moreover, some approximations of the basic equations are made because of either the considered scale of motion or the small contribution of the water constituents to the total mass of and air volume. According to Doms (2011; page 18-19), the following simplifications are presupposed in the model:

1) all molecular fluxes are neglected except the diffusion fluxes of the liquid and solid water;
2) the specific heat of moist air is replaced by the specific heat of dry air;
3) the impact on pressure due to changes in the concentrations of the water constituents resulting from diffusion fluxes and phase transitions are neglected;
4) the temperature changes due to buoyant heat and moisture fluxes are neglected completely, together with the mean dissipation rate due to viscous stresses.

Up to now, the equations are expressed in spherical coordinates to take into account the curvature of the earth. However, this coordinate system generates numerical problems due to the convergence of the meridians both

when simulating a domain over the geographical pole and, as more often happens, when changing horizontal resolution with latitude away from the equator. To overcome this issue, the model use rotated spherical coordinates. In the new coordinate system, the intersection of the equator and the prime meridian is located in the simulation domain, thus minimising the convergence of the meridians. Figure 3 shows the default rotation applied in the model. COSMO-EU, COSMO-DE as well as all the simulations in this study place the North Pole at 40°S and -170.0°E in the non-rotated system.

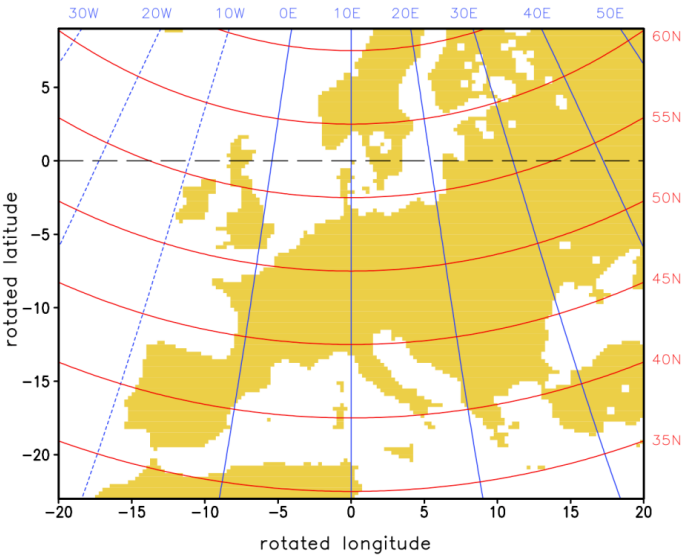

Figure 3: Geographical longitude (blue) and latitude (red) in the non-rotated grid. The dashed line indicates the equator in the rotated grid with the pole coordinates 32.5°S and -170.0°E in the non-rotated system. The rotated 0° meridian corresponds to the 10°E geographical meridian (Doms 2011).

Afterwards, the grid-scale thermodynamic variables are described as a base-state value plus a grid-scale deviation (not to be confused with turbulent fluctuations). The assumption is that the reference state depends only on

the height above the surface and is hydrostatically balanced. This allows neglecting the horizontal base-state pressure gradient terms in the equation of motion, thus enhancing the numerical accuracy of the model in the case of sloping coordinate surfaces. This type of surface is generated when using terrain-following vertical coordinates as in the model.

The terrain-following coordinate system is introduced to simplify the representation of the lower boundary condition and thus the numerical solution of the equations. The vertical coordinate ζ is then a time-independent function of λ , ϕ and z. To guarantee that the numerical solution of the model equations is independent from the selection of ζ, the transformation first uses a user-defined coordinate $\tilde{\zeta}$. Three options for the terrain-following coordinate $\tilde{\zeta}$ are available: (1) a reference-pressure based coordinate, (2) a height-based coordinate, and (3) a height-based SLEVE (Smooth Level Vertical) coordinate. Then, a monotonic function *m* is used to map $\tilde{\zeta}$ to the computational coordinate. The *m* function is selected to map $\tilde{\zeta}$ to the index space used for the vertical discretization with top-down increasing indices and equidistant grid spacing (Figure 4). Thus the irregular curvilinear grid generated with the terrain-following coordinate is mapped onto a regular rectangular grid labelled by integers.

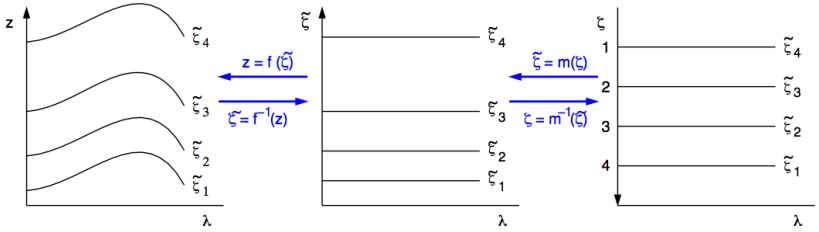

Figure 4: Mapping of an irregular curvilinear grid associated with the terrain following coordinate $\tilde{\zeta}$ onto a rectangular equidistant grid ζ labelled by integers.

After all these transformations, the model equations forming the basis of the model system can finally be written as seven prognostic equations and one diagnostic equation for horizontal wind velocity, vertical wind velocity, perturbation pressure, temperature, water vapour, liquid and solid forms of water, and total density of air:

- Horizontal wind velocities

$$\frac{\partial u}{\partial t} = -\left\{\frac{1}{a\ cos\,\varphi}\frac{\partial E_h}{\partial \lambda} - v\,V_a\right\} - \dot{\zeta}\frac{\partial u}{\partial \zeta} - \frac{1}{\rho a\ cos\,\varphi}\left(\frac{\partial p'}{\partial \lambda} - \frac{1}{\sqrt{\gamma}}\frac{\partial p_0}{\partial \lambda}\frac{\partial p'}{\partial \zeta}\right) + M_u$$

$$\frac{\partial v}{\partial t} = -\left\{\frac{1}{a}\frac{\partial E_h}{\partial \varphi} + u\,V_a\right\} - \dot{\zeta}\frac{\partial v}{\partial \zeta} - \frac{1}{\rho a}\left(\frac{\partial p'}{\partial \varphi} - \frac{1}{\sqrt{\gamma}}\frac{\partial p_0}{\partial \varphi}\frac{\partial p'}{\partial \zeta}\right) + M_v$$

- Vertical wind velocity

$$\frac{\partial w}{\partial t} = -\left\{\frac{1}{a\ cos\,\varphi}\left(u\frac{\partial w}{\partial \lambda} + v\,cos\,\varphi\frac{\partial w}{\partial \varphi}\right)\right\} - \dot{\zeta}\frac{\partial w}{\partial \zeta} + \frac{g}{\sqrt{\gamma}}\frac{\rho_0}{\rho}\frac{\partial p'}{\partial \zeta} + M_w + \\ + g\,\frac{\rho_0}{\rho}\left\{\frac{(T - T_0)}{T} - \frac{T_0 p'}{T p_0} + \left(\frac{R_v}{R_d} - 1\right)q^v - q^l - q^f\right\}$$

- Perturbation pressure

$$\frac{\partial p'}{\partial t} = -\left\{\frac{1}{a\,cos\,\varphi}\left(u\frac{\partial p'}{\partial \lambda} + v\,cos\,\varphi\frac{\partial p'}{\partial \varphi}\right)\right\} - \zeta\frac{\partial p'}{\partial \zeta} + g\rho_0 w - \frac{c_{pd}}{c_{vd}}pD$$

- Temperature

$$\frac{\partial T}{\partial t} = -\left\{\frac{1}{a\ cos\,\varphi}\left(u\frac{\partial T}{\partial \lambda} + v\,cos\,\varphi\frac{\partial T}{\partial \varphi}\right)\right\} - \dot{\zeta}\frac{\partial T}{\partial \zeta} - \frac{1}{\rho c_{vd}}pD + Q_T$$

- Water vapour

$$\frac{\partial q^v}{\partial t} = -\left\{\frac{1}{a\ cos\,\varphi}\left(u\frac{\partial q^v}{\partial \lambda} + v\,cos\,\varphi\frac{\partial q^v}{\partial \varphi}\right)\right\} - \dot{\zeta}\frac{\partial q^v}{\partial \zeta} - \left(S^l + S^f\right) + M_{q^v}$$

- Liquid and solid form of water

$$\frac{\partial q^{l,f}}{\partial t} = \\ = -\left\{\frac{1}{a\ cos\,\varphi}\left(u\frac{\partial q^{l,f}}{\partial \lambda} + v\,cos\,\varphi\frac{\partial q^{l,f}}{\partial \varphi}\right)\right\} - \dot{\zeta}\frac{\partial q^{l,f}}{\partial \zeta} - \frac{g}{\sqrt{\gamma}}\frac{\rho_0}{\rho}\frac{\partial P_{l,f}}{\partial \zeta} + S^{l,f} \\ + M_{a^{l,f}}$$

- Total density of air

$$\rho = p\left\{R_d\left(1 + \left(\frac{R_v}{R_d} - 1\right)q^v - q^l - q^f\right)T\right\}^{-1}$$

with T_0, p_0, ρ_0 base state values of temperature, pressure and density

c_{vd}, c_{pd} specific heat at constant pressure of water vapour, dry air

R_d, R_v gas constant for dry air and water vapour

ρ density

ζ terrain following vertical co-ordinate

$\dot{\zeta}$ contravariant vertical velocity

E_h kinetic energy of horizontal motion

D divergence of the wind field

ϕ, λ rotated latitude, longitude

p' grid scale pressure deviation

$\sqrt{\gamma}$ variation of reference pressure with ζ

V_a absolute vorticity

Q_T diabatic heating

The terms S^l, S^f represent the cloud microphysical sources and sinks due to phase change; Q_r the radiative heating; $P_{l,f}$ the precipitation fluxes and Mψ the source terms due to small scale turbulent mixing and subgrid scale moist convection (see Chapter 2.5), which is the dominating subgrid scale

transport process at meso-β scale. M_ψ also includes for simplicity some terms related with the schemes for numerical smoothing and for relaxation and mixing in the lateral and upper boundary zone. The terms related to subgrid-scale processes are calculated by the corresponding physical parameterisation scheme.

2.2. Grid structure and time integration

To solve the model equations derived in the previous chapter, the computational grid is set by using a constant increment of the independent variables (i.e. λ, φ and ζ). This method allows the (λ, φ, ζ)-space to be represented by a finite number of grid points identified by i, j, and k in the λ, φ and ζ direction respectively. Every grid point (i, j, k) represents the centre of the elementary grid volume ($\Delta\lambda$, $\Delta\varphi$, $\Delta\zeta$).

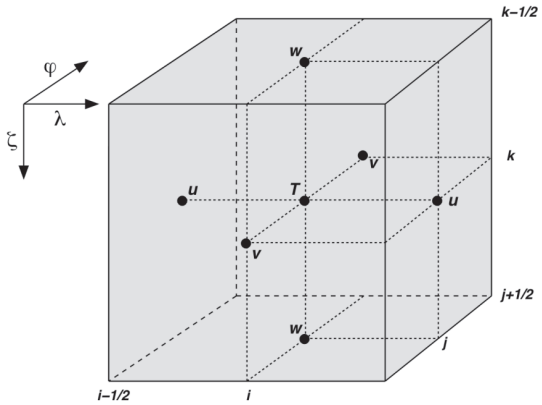

Figure 5: A grid box volume $\Delta V = \Delta x \Delta\lambda \Delta\varphi$ showing the Arakawa-C/Lorenz staggering of the dependent model variables (Doms et al. 2011). T represents all the scale variables.

The faces of the grid-boxes are set halfway between the grid points. The top (lower) boundary of the model domain is defined to be the half level above (below) the uppermost (bottommost) model layer. Note that the lower boundary corresponds to the terrain height. According to the Arakawa-

C/Lorenz grid structure, temperature, pressure and humidity are defined at the grid point (i.e. the centre of the elementary volume), while the wind components at the corresponding box faces. Figure 5 shows the above described Arakawa-C/Lorenz grid structure.

The model needs a time splitting technique to separate the fast processes related to acoustic and gravity wave from the slower motion modes in the prognostic equations. The former are then integrated according to the selected method. All the simulations in this study use a normal 3rd order Runge-Kutta time-stepping scheme (Wicker and Skamarock 2002). The scheme is used operationally for both COSMO-EU and COSMO-DE because of its stability and efficiency.

2.3. Physical parameterisation

Atmospheric processes span a wide range of scales both in terms of time and space, from molecular to planetary scales as well as from seconds to years. On the other hand, RCMs cannot cover either all time or spatial scales of the atmospheric phenomena. Thus, parameterisations of the important physical processes are used to account for all the processes that cannot be explicitly solved because of the limited time or spatial scale of the model. The following presents a brief overview of the most prominent parameterisations used by CLM at both 2.8 km and 7 km resolution (except where differently stated). More details can be found in Doms et al. (2011).

The simulations use a delta-two-stream radiation scheme according to Ritter and Geleyn (1992) with full cloud-radiation feedback. The calculation of grid scale clouds and precipitation follows the Kessler scheme (Kessler 1969), which considers the following hydrometeor species: water vapour, cloud

droplets, rain, snow, cloud ice, and, also graupel[1] for the convection-permitting scale. The various categories interact maintaining the total water mass constant.

Vertical turbulent diffusion uses the prognostic turbulent kinetic energy (TKE) closure at level 2.5 (Raschendorfer 2001). This scheme accounts for the effects of both subgrid-scale condensation and thermal circulations, but it still hypothesizes horizontal homogeneity, i.e. only vertical turbulent fluxes. A new version of the surface transfer scheme was introduced to have a consistent formulation with the TKE scheme for the transport through the surface layer. In this context, the surface layer is divided into a laminar-turbulent sub-layer just above the surface and a constant-flux or Prandtl layer above. This subdivision allows a distinction between the values of the model variables at the ground (predicted by the soil model) and at the lower boundary of the turbulent atmosphere, i.e. at the roughness height z_0 (calculated by the atmospheric model). The heat fluxes are based on drag-law formulations using the temperature and specific humidity at the surface and at the lowest atmospheric level calculated by the soil and the atmospheric model respectively. The new surface scheme generates the stability functions using the dimensionless coefficients of the Mellor-Yamada closure and the interpolation rules, rather than the empirical Monin-Obukhov functions. Both new schemes were extensively tested by DWD and they are now used operationally in both COSMO-EU and COSMO-DE.

The multilayer soil model TERRA_ML (Schrodin and Heise 2001) is implemented in CLM to predict the temperature and specific humidity at the ground. The soil model considers five soil types (plus ice, rock and water) and ten active layers for energy transport up to a depth of 15 m. The surface

1 Graupel defines particles with spherical shape, higher density than snow and fall speeds of about 1 – 3 m/s (Doms et al. 2011).

humidity is calculated from the sum of all surface fluxes of moisture parameterized by the soil model (i.e. evaporation from bare soil, interception and snow reservoirs, transpiration and formation of dew and rime). The surface temperature is a weighted mean between the temperature of the uppermost soil layer and the snow temperature. Bare soil evaporation and plant transpiration are computed following the recommendation of Dickinson (1984), while the calculation of the transport of liquid water uses the prognostic Richards equations (Hillel 1980). The soil temperature T_{so} is predicted with the basic heat equation:

$$\partial \frac{T_{so}}{\partial t} = \frac{1}{\rho c} \frac{\partial}{\partial z} \left(\lambda \frac{\partial T_{so}}{\partial z} \right)$$

with λ, ρc heat conductivity and capacity respectively.

The annual mean temperature is prescribed as a boundary value at the bottom layer, so-called climate layer. Only once, at the beginning of the simulation, is the soil moisture initialised, through the forcing, according to the soil type. Then, it evolves freely without correction throughout the whole simulation. Nevertheless, soil moisture has a long memory and thus it can affect the atmospheric processes at the land surface long after the initialisation (Koster and Suarez 2003; Pan et al. 2001; Seneviratne et al. 2002; Wu and Dickinson 2004). Changes in soil moisture influence directly not only soil temperature and evaporation (Betts et al. 1996), but also the precipitation rate (Eltahir 1998; Schär et al. 1999). To reduce the effects of initialisation, it is common practice within the climate community to remove the first few years of a simulation (considered as spin-up time) for the analysis.

2.4. Atmospheric convection

In meteorology, convection mainly refers to the vertical motion of air parcels in the atmosphere mostly caused by buoyancy force. Convection can take many forms in the atmosphere, being dry or moist, as well as shallow or

deep. This study focuses on moist convection, which, unlike dry convection, implies that there is a conversion of water vapour to liquid water as the parcel is displaced vertically, i.e., the parcel becomes saturated. The main difference between shallow and deep convection lies in the vertical extent of this phenomenon. The former does not usually extend to more than 1 to 2 km in the atmosphere, while the latter can reach up to approximately 10-15 km. Because of its spatial scale shallow convection needs to be parameterised in CLM even at convection-permitting scale and therefore it is not the focus of this analysis. Deep moist convection is the form of convection responsible for various hazardous weather situations due to the release of a large amount of energy by phase changes of water. Since deep moist convection is the only type of convection investigated in this chapter, we will refer to it in the following simply as convection.

Although there is no unique initiating process for convection, two ingredients are most important: atmospheric instability and a triggering mechanism (Emanuel 1994; Houze 1993). The first guarantees the enhancement of the vertical motion of an air parcel; the second is required for the release of the available energy for convection. The parcel method is often used to assess the potential of the atmosphere to convection. The main idea is to evaluate the buoyancy of a parcel that is displaced from its original position through a pseudo-adiabatic process. The lifting of air mass, which causes its cooling and results in its saturation and thus condensation, can have several reasons. Forced convection happens when there is some kind of dynamic mechanism forcing the air upwards. For example, frontal lifting occurs when two air masses differing in temperature and humidity, encounter each other and the warmer and more humid mass is forced upwards because of its smaller density. Orographic lifting is due to the presence of the slopes of a hill or mountain while wind convergence generates upward motion as it lifts surface air higher in the atmosphere. Besides all the lifting mechanisms men-

tioned above, the most common and easily seen form of convection is generated by thermal instability and it is usually referred as free convection, which usually develops in cumulus clouds with a characteristic horizontal length of few kilometres (Emanuel 1994).

The Skew-T plot is a very common technique to visually display the vertical motion and allows for calculation of the significant levels connected with convection. Figure 6 provides an example of this type of thermodynamic diagram. In the background, it shows the isobars horizontally while the isotherms are skewed to the right. According to the simple parcel theory, convection starts at the surface when an air parcel starts rising because of either thermal instability or mechanical forces. Due to the pressure decrease, the lifting causes the expansion of the parcel and thus it is cooling according to the dry adiabatic lapse rate (straight line in Figure 6). If the rising parcel contains moisture, it eventually cools sufficiently to reach saturation and thus water starts condensing and forming clouds. This level is called lifted condensation level, LCL. The change in state causes the release of latent heat of condensation, which fuels the parcel with additional energy. The parcel's temperature will now decrease following the moist adiabatic or pseudoadiabatic lapse rate (dashed curve in Figure 6).

From the LCL, three scenarios are possible. If the rising parcel has a temperature considerably higher than the environment, it becomes buoyant and it can continue ascending further (unstable atmosphere or absolute instability). In the second case, the temperature decreases slowly with height, the parcel's buoyancy is smaller and convection is more unlikely to occur (stable atmosphere). Figure 6 shows the third situation (conditional stability), where the parcel is negatively buoyant for some distance. This means that for small upward displacement, stability is maintained but if the parcel is forced above the level of free convection (LFC), it again becomes positively buoyant and it

can freely continue its ascent until the equilibrium level (EL) is reached, also called limit of convection or level of neutral buoyancy (LNB). When conditional instability occurs, deep cumulus clouds form. Within the LFC and EL the condensate will eventually grow in size until their gravity force becomes larger than the friction forces holding them and they are forced to precipitate. Figure 6 visualizes two important indices for convective processes: the green area represents CAPE (Convective Available Potential Energy; Moncrieff and Miller 1976) and the red part the Convective Inhibition (CIN; Colby 1984). They indicate respectively the atmospheric potential and opposition to the initiation of convective processes.

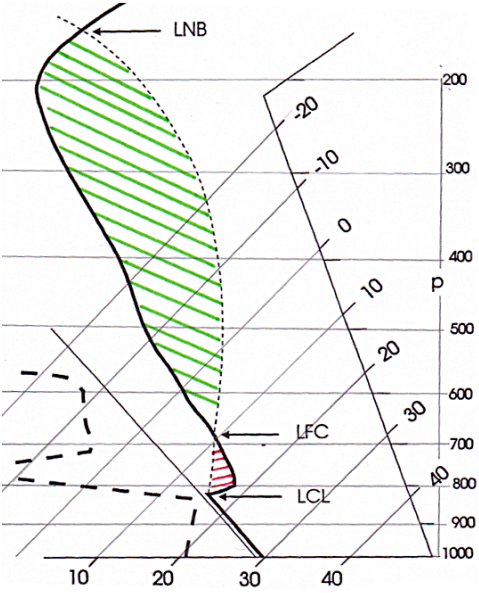

Figure 6: Skew-T plot showing an example if an atmospheric sounding (from Smith 1997). Straight (dashed) lines indicate a dry (pseudo-moist) adiabatic. The thick solid (dahed) line shows the measured (dew point temperature). The area in green (red) represents CAPE (CIN).

2.5. Model parameterisation of moist convection

In general a parameterisation is meant to represent the ensemble effects of subgrid processes on resolved variables, given that it is not possible to resolve them on sub-grid scale (Doms et al. 2011). In this case, a closure condition is necessary to link the parameterization to the explicitly resolved processes. Convective parameterisation is a classic case where it is not possible to calculate the sub-grid vertical velocity and thus the scheme calculates the influence of sub-grid convective tendencies on the model grid space. This chapter provides an overview on the parameterisation of the convection in CLM model. The information is taken from Doms et al. (2011), where more details can be found.

The Tiedtke scheme uses a vertical mass-flux approach to represent moist convection (Tiedtke 1989). In particular, it uses the grid-scale variables to calculate the vertical mass flux at the convective cloud base. A one-dimensional cloud model is applied to calculate the feedback of subgrid-scale vertical fluxes of mass, heat, moisture and momentum in up- and downdrafts. This bulk model approximates the net effects of an ensemble of clouds as a single representative cloud (Yanai et al. 1973). Although the parameterisation neglects the impact of convective mesoscale circulations on large-scale heat and moisture budgets, it includes the basic effects of moist convection, namely:

- diabatic heating due to the release of latent heat caused by both cloud condensation and formation/evaporation of precipitation,
- vertical transports of heat, moisture and momentum in cumulus updrafts and downdrafts,
- entrainment and detrainment processes by lateral exchange within cumulus clouds.

The scheme distinguishes between three types of moist convection: shallow convection, deep convection and midlevel convection, but only one type of convection can occur at a specific grid point at a certain time. This means that the scheme is not able to describe layered convection, i.e. midlevel convection above a layer of shallow convection. Both shallow and deep convection originate in the atmospheric boundary layer, but they differ in their vertical extent (see Chapter 2.4 for details). By contrast, midlevel convection has its roots at much higher level, within the free atmosphere. A dynamical lifting of air mass to the LFC is usually responsible for this type of convective cells.

The scheme proceeds according to the following steps:

(1) determine if convection occurs and define the type (trigger function).

The scheme first verifies whether free convection (shallow or penetrative) can occur at each grid point. Therefore, an air parcel is defined with the temperature (plus 0.5 K), the specific humidity and the horizontal momentum registered at the first model level above the surface. Then the parcel is lifted adiabatically and the model computes its LCL. If the parcel is found buoyant with respect to the environment, then LCL corresponds to the LFC and the updated variables representing the air parcel in the new level can be used as boundary conditions for the updraft equations. Alternatively, if the lifted parcel is non-buoyant at the LCL, the grid point is checked for the occurrence of mid-level convection. Starting from the surface the air parcel with environmental properties is lifted adiabatically by one model layer. If it becomes buoyant in the new layer, this is the LCL for mid-level convection and the model follows the same procedure as before. Otherwise, the next model layer is checked for convection and so on. In order to occur, mid-level convection at LCL needs to have a positive vertical velocity and a relative humidity larger than 90%.

(2) calculate the cloud base mass flux (closure assumption) using the grid-scale variables determined in step (1)

Depending on the specific type of convection, the scheme applies different closure hypotheses. For shallow and penetrative convection, the mass flux is set proportional to the vertically integrated moisture convergence between the surface and the cloud base (Kuo-type closure). Therefore, convection occurs only if moisture convergence increases the subcloud moisture content:

$$\{M_u(q_u^v - q^v) + M_d(q_d^v - q^v)\}_{z_b} = -\int_{z_s}^{z_b} \left(\rho \boldsymbol{v} \cdot \nabla q^v + \frac{\partial F^{q^v}}{\partial z}\right) dz$$

with z_b terrain height, z_b height of the cloud base, F^{q^v} vertical turbolent flux of specific humifity.

In case of midlevel convection, the updraft mass flux at cloud base is simply proportional to the grid-scale vertical velocity *w*, i.e. the moisture vertically advected through the cloud base is fully available for convective activities.

$$(M_u)_{z_b} = (\rho w)_{z_b}$$

(3) apply the bulk cloud model to vertically distribute heat, moisture, momentum and formation of precipitation and compute the convective tendencies M_ψ^{MC}, i.e. the feedback of subgrid vertical circulation into the resolved flow. Neglecting non-hydrostatic effects on the mesoscale and changes in the mean vertical velocity, these tendencies can be written:

$$c_{pd} M_T^{MC} = \left(\frac{\partial s}{\partial t}\right)_{MC} =$$

$$= -\frac{1}{\rho}\frac{\partial}{\partial z}\{M_u(s_u - s) + M_d(s_d - s)\} + L\left(c_u - e_d - e_l - e_p\right)$$

$$M_{q^v}^{MC} = \left(\frac{\partial q^v}{\partial t}\right)_{MC} = \\ = -\frac{1}{\rho}\frac{\partial}{\partial z}\{M_u(q_u - q) + M_d(q_d - q)\} - \left(c_u - e_d - e_l - e_p\right)$$

$$M_{\alpha}^{MC} = \left(\frac{\partial \alpha}{\partial t}\right)_{MC} = -\frac{1}{\rho}\frac{\partial}{\partial z}\{M_u(\alpha_u - \alpha) + M_d(\alpha_d - s)\}$$

with:

$s = c_{pd}T + gz$ dry static energy

$M_u = \rho\alpha_u(w_u - w)$ updraft mass flux and $M_d = \rho\alpha_d(w_d - w)$ downdraft mass flux

a_u, a_d area fraction of the updraft and downdraft, resp.

w_u, w_d vertical velocity of the updraft and downdraft, resp.

s_u, s_d dry static energy within the up- and downdraft, resp.

q_u, q_d specific humidity within the up- and downdraft, resp.

α_u, α_d horizontal wind components in the up- and downdraft, resp.

c_u condensation in the updraft (area mean)

e_d evaporation of precipitation in the downdraft (area mean)

e_l evaporation of cloud water in the environment (area mean)

e_p evaporation of precipitation below cloud base (area mean)

L latent heat with $L = L_V$ (heat of evaporation) for $T \geq 0\ ^{\circ}C$ otherwise $L = L_S$ (heat of sublimation)

The convection parameterisation affects several other fields besides precipitation. Particularly interesting for this study is cloud cover. For the parameterisation scheme for grid-scale clouds and precipitation, each grid cell can either be fully filled with clouds or cloud free. However, for the calculation of e.g. radiative transfer, the model defines a fractional cloud cover σ_c for all grid boxes. The calculation of σ_c in each model layer is based on an empirical

function depending on the relative humidity, the height of the model layer and the convective activity, and in particular the vertical extent of the convection cell.

The Tiedtke scheme does not use CAPE as closure assumption. CAPE, as well as CIN, is calculated at each grid point independently according to the parcel theory. A well-mixed near surface layer is assumed with a depth of 50 hPa. The parcel starts from a level approximately in the middle of this layer, with the average specific humidity and potential temperature as start values. The method follows the recommendations of Doswell and Rasmussen (1994).

2.6. Initial and boundary conditions

To start a simulation, RCMs need information on the initial state of the atmosphere and soil moisture and soil temperature profiles. In addition, data about the lower boundary of the domain like orography and vegetation cover (the so-called “external” data) are required (Table 1).

Using standard datasets from various sources (e.g., orography from the Global Land One-km Base Elevation (GLOBE), harmonized world soil database from the Food and Agriculture Organization of the United Nations (FAO)), the CLM Community provides the external data for the required horizontal resolution and region. After the initialization, the lateral boundary conditions are updated regularly every six hours in our simulations. The initial and boundary conditions can be interpolated from either GCMs or a coarser nest of RCMs through the so-called nesting procedure. This research applies the one-way nesting strategy, i.e. RCMs use GCMs (or coarser RCMs resolution) information as driving data at its lateral boundaries, but the results thus obtained are not fed back into the GCMs simulations.

Table 1: Summary of the initial and external data required by the model (Schättler et al. 2013). The * symbol indicates the variables are required also as boundary data in climate mode.

External data	Initial data
Height of surface topography	Zonal and meridional wind speed *
(alternatively) geopotential of the earth's surface	Vertical wind speed
Fraction of land in the grid cell	Pressure deviation from reference pressure *
Soil type	Temperature *
Roughness length	Specific water vapour and cloud water content *
Plant cover *	Specific cloud ice, rain and snow content *
Leave area index and root depth *	Specific water vapour content at the surface *
Vertical integrated ozone content and ozone maximum*	Temperature of snow surface *
	Water content of snow *
	Water content of interception
	water Temperature at surface*
	Temperature and moisture on the different soil layers
	Density of snow and snow 'freshness'

The model needs a buffer zone to generate reliable RCM results from the GCM data received at the boundary. In this sponge area the GCM information has an exponentially decreasing weight on the RCM internal solution. According to Doms (2011), the depth of this relaxation zone is at least eight grid boxes at each lateral boundary. Moreover, the simulation domains should be sufficiently large to allow the model to become uncoupled from the forcing (McGregor 1997) and thus develop its own climate. Meantime, finer and coarser nest should not differ too strongly in terms of synoptic circulation (Jones et al. 1995). Sensitivity studies are necessary to determine the optimum size and location of the simulation domain depending on the region and the atmospheric variables under investigation.

As forcing data, different datasets can be used depending on the scope of the investigation. Table 2 summarises the forcings used in this research and their main characteristics.

Table 2: Used driving dataset and their characteristics.

Name	Spatial resolution	Covered period	Type
ERA40	~125 km	1957-2002	Reanalysis data
ECHAM5	~150 km	1860-2100	Climate runs

ERA40 reanalysis data (Uppala et al. 2005) are often used as driving data when the purpose is to determine the biases of the RCM itself (i.e. to validate the model). In fact, reanalysis datasets provide a spatially coherent record of the historical atmospheric fields since they are created assimilating observations while running GCMs for past decades. Other GCMs are used to investigate the climate change signal. The GCM ECHAM was developed at the Max Planck Institute for Meteorology and it is one of the contributing models for AR5. Its fifth version ECHAM5 (Roeckner et al. 2003) is widely used for climate studies (e.g. Feldmann et al. 2012; Reichler and Kim 2008; Wagner et al. 2012). This type of model gives the possibility to investigate both past and future periods since it covers the period 1860-2100. On the other hand, ECHAM5 is designed to describe correctly the statistics of the climate variables but a time correspondence between GCM driven simulations and observed events cannot be expected because they have complete freedom to develop their own climate (Feldmann et al. 2008). Moreover, changing the forcing (e.g. ECHAM5 versus ERA40) affects the model performance and can add an additional bias (Berg et al. 2012).

2.7. Nesting strategy

Dynamical downscaling is used to downscale GCM information to regional scales. Results from the coarser nests (either GCMs or previous RCM runs) are used to drive the higher resolution simulation (i.e. the finer nest). Denis et al. (2003) suggested that the jump in horizontal resolution between two nests should be limited to a ratio of 12 to yield realistic results.

IMK-TRO established its own nesting strategy which provides satisfying results at 7 km resolution (Berg et al. 2012; Feldmann et al. 2008; Meißner 2008). From GCM, the coarsest RCM nest is at about 50 km resolution and embraces the whole of Europe with 118 × 112 grid points. The next finer nest at 0.0625° (circa 7 km) comprises all of Germany and the near surroundings with 165 × 200 grid points (Figure 7). The finest nest at 0.025° (circa 2.8 km) centres on the state of Baden-Württemberg in southwestern Germany.

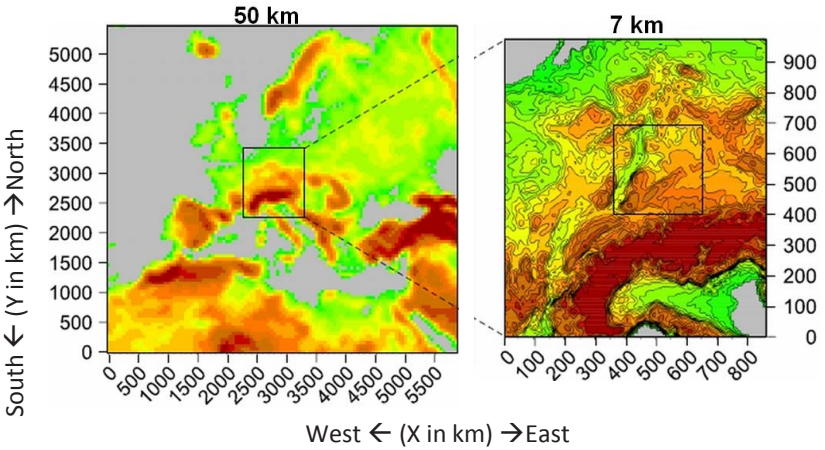

Figure 7: Simulation domain for each step of the nesting strategy, namely 50 km (left), 7 km (right) and 2.8 km domain (inner black frame) in southwestern Germany. Orographic heights are indicated in colour.

3. Observational datasets

In this study, two different observational datasets are used for the validation of the model performance. The next chapters first present the HYRAS gridded daily dataset and then the measurement stations maintained by DWD and their characteristics.

3.1. HYRAS dataset

HYRAS dataset is a gridded 1 x 1 km precipitation and temperature dataset covering the whole of Germany and some river catchments in neighbouring countries, recently created by DWD (Rauthe et al. 2013). HYRAS is the updated version of the REGNIE dataset often used by the hydrological and meteorological communities (Berg et al. 2012; Photiadou et al. 2011; Schwitalla et al. 2008). The dataset has a daily temporal resolution and covers the period 1951 to 2006. The gridded precipitation field is calculated from 6200 precipitation stations using REGNIE (REGionalisierung der NIEderschlagshöhen, regionalised precipitation amount) method. The gridding strategy is based on a combination of multiple linear regression, accounting for orography, and inverse distance weighting (Perry and Hollis 2005; Widmann and Bretherton 2000). In particular, the method first calculates a background climatological field including corrections for the elevation of the stations and the orientation of the terrain in terms of wind exposure. Then, anomalies are calculated assigning to each grid point a station value and dividing it by the background data. The anomalies are interpolated using inverse distance weighted interpolations, and finally, the results are multiplied by the background field (Bartels et al. 2005; Berg et al. 2012; Dietzer 2003).

The REGNIE method guarantees that observed extreme precipitation as well as non-precipitation events are maintained unchanged in the gridded field

(Rauthe et al. 2013). This is a crucial aspect for this research that gives a special attention to the characteristics of the precipitation pattern impacting the most on erosion, namely strong precipitation intensities and the alternation of dry and wet period. Rauthe et al. (2013) found that the HYRAS dataset compares well with other existing datasets especially in flat areas. The mean absolute error is less than 2 mm/day, but varies spatially and temporally.

3.2. Measurement stations

Figure 8 shows the DWD stations available in the state of Baden Württemberg, in southwestern Germany.

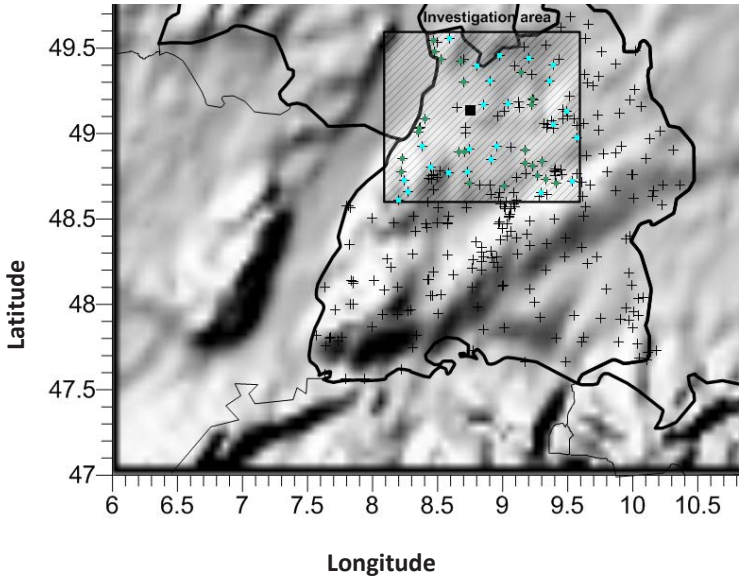

Figure 8: Map of Baden Württemberg in southwestern Germany showing the investigation domain (black frame) around Weiherbach catchment (black square) and all available DWD measurement stations between 1950 and 2004 (cross points). The blue (green) dots represent the gauges with 5-minute (30-minute) temporal resolution within the investigation area between 1997 and 2004 used for the analysis.

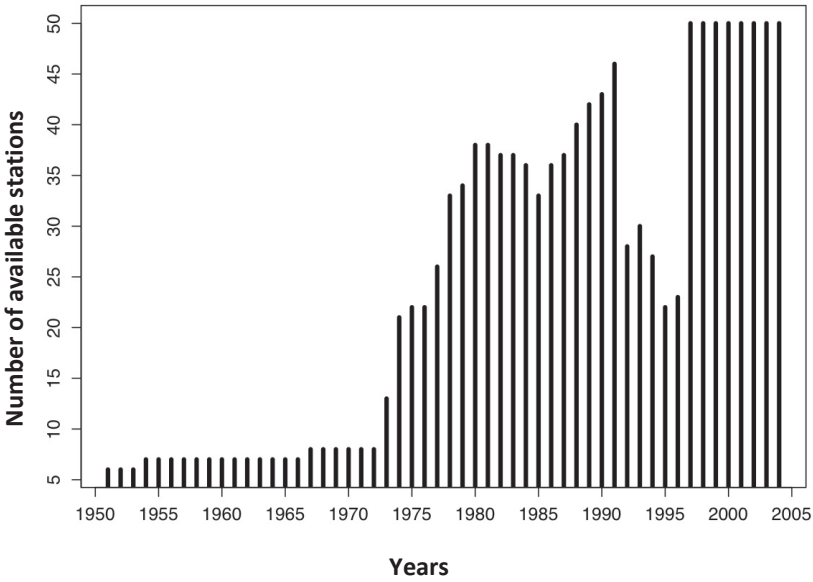

Figure 9: Number of available station within the investigation domain between 1950 and 2004. The stations have different temporal resolutions, namely 5 or 30 minutes.

All the rain gauges use the weighting principle and have a lower measurement limit of 0.01 mm (Brommundt and Bárdossy 2007). From 1950 to 2004, the number of stations varies considerably and only few of them are active for long periods. Figure 9 shows the total number of stations available for each year within the investigation area (black frame in Figure 8), but it does not clarify if it is the same station that is active. Often, especially in the seventies and eighties of the last century, the rain gauges were active for a few years only before being replaced by new stations at other locations. For the model validation the observations dataset should be as long as possible and consistent in time and space. The period 1997-2004 presents the highest number of active stations with a stable density, namely 48. Half of them have a 5-minute temporal resolution, while the rest has 30 minutes (Figure 8 in blue and green respectively). Since these stations were recently activated

and automated, they should provide more reliable measurements in comparison with stations operating previously (Rauthe et al. 2013).

The quality of the signal both in summer and winter is shortly to be investigated considering the:

- average number of missing values per station per year (Table 3);
- influence that the height of the stations and their temporal resolution have on the diurnal cycle of precipitation (Figure 10 and Figure 11).

On average, the stations with 5-minute resolution are more reliable in comparison with those at coarser temporal resolution. This is especially true in summer, when the number of missing value in their time series is negligible (Table 3).

Figure 10 shows the diurnal cycle of precipitation for each station, displayed in different colours depending on the height range. The amount of mean precipitation increases with the elevation of the station, in agreement with literature (Khodayar et al. 2010). For both winter (DJF) and summer (JJA), it is evident that two stations are completely out of the range. According to DWD specifications, they are located at 750 m and 110 m. In reality, the latter, Hornisgrinde station, is at 1164 m, which explains the mismatch. To guarantee a homogenous dataset, only the 45 stations below 700 m active between 1997 and 2004 are selected for the following investigation. Of those, 21 have 5-minute resolution, while the rest have a coarser temporal scale (i.e. 30 min).

Table 3: Average number of missing values per station per year depending on the season and the temporal resolution of the station.

Average number of missing value per station per year	5 minutes	30 minutes
JJA	12	296
DJF	189	275

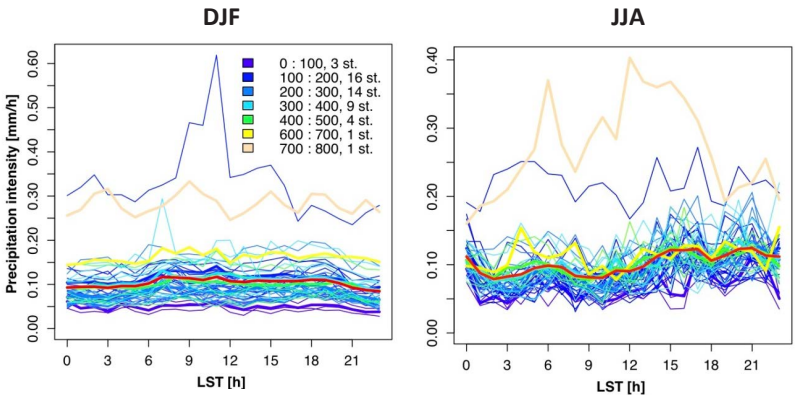

Figure 10: Diurnal cycles of precipitation, in DJF (left) and JJA (right), for each station within the investigation area in the period 1997-2004. The different colours represent the height of the stations, according to the legend. The thick lines represent the mean of a specific range with the same colour, while the red thick line the average over all stations. Note the different scale for winter and summer.

Figure 11 shows the diurnal cycles of precipitation for the selected 5 and 30-minute stations, respectively in black and yellow colour. In both seasons, the pattern is similar between resolutions, although the measurement stations at coarser temporal resolution have lower mean value. This could be linked to their average height, which is lower in comparison with stations with 5-minute resolution. Although the spread among stations is quite broad (grey and yellow shaded areas), the observational diurnal cycles have a distinct character in both seasons. In winter (left panel), the diurnal cycle presents

higher intensities during daytime and a peak around 8:00. In summer (right panel), the two main maxima are at 15:00 and 20:00.

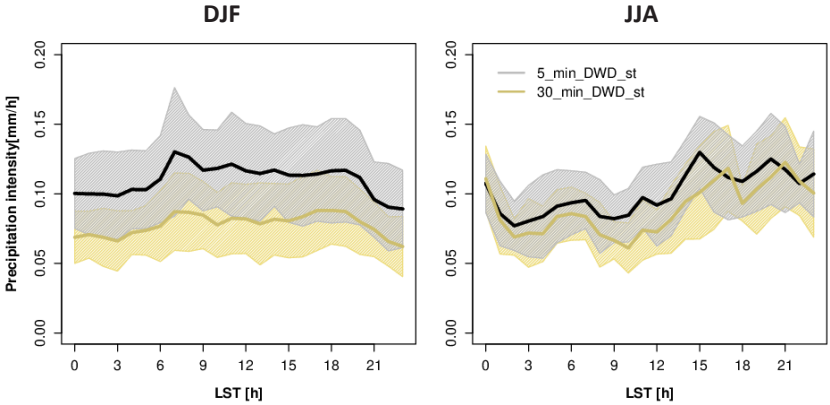

Figure 11: Diurnal cycles of precipitation, in DJF (left) and JJA (right), calculated considering only the stations with a temporal resolution of 5 (black/grey) and 30 (yellow) minutes. The shaded areas indicate the spread of the signal calculated as the mean ± the standard deviation for the stations.

There are statistical relationships among stations. To illustrate this, the precipitation time series of two measurement stations, namely Eppingen and Kraichtal, are selected. They are the closest available rain gauges to Weiherbach, which is one of the erosion-prone catchments selected by the KLIWA project. They are both active between 1986 and 1992 and are about 10 km apart. Table 4 shows the temporal correlation between the two time series both in JJA and DJF calculated on hourly and daily bases. The correlation coefficients are calculated using different methods. Pearson's r test gives a measure of the linear dependence between two variables (Pearson 1920). Although Pearson's r test is frequently and widely used, nonparametric methods are more suitable when dealing with non-normal distributed data (Kendall 1962; Sommer and Sommer 2002). Moreover, replacing the observations with their ranks, such as in the case of Spearman's rank and Kendall's

tau correlation, allows reducing the impact that outliers have on the final score (Abdullah 1990).

Table 4 shows a higher temporal correlation in winter than in summer at both temporal resolutions. This depends on the characteristic of the precipitation pattern in the different seasons. Large-scale weather patterns, like frontal passages, play the strongest role in the precipitation occurrence during winter, while in summer precipitation is mainly due to convection. The latter phenomenon acts on a scale of few kilometres and is strongly related to orography and local conditions. Thus, the chances that both stations are hit by the same precipitation event are higher in winter than in summer (Table 4). Moreover, Table 4 underlines the strong differences arising from the different temporal scale used for the analysis (i.e. hourly versus daily scale). In fact, the correlation coefficients have much lower values on an hourly than on a daily basis, for all methods and especially in summer. Thus, when comparing model simulations with observations and especially on hourly basis, it might be important to select the nearest model grid points to the stations in order to avoid sampling bias. This is particularly important in areas with different landscapes and steep orography (Moberg and Jones 2004).

Table 4: Temporal correlation between Eppingen and Kraichtal measurement stations on hourly and daily bases both in JJA and DJF, according to several methods. The period considered is 1986-1992.

Correlation	JJA		DJF	
	Hourly	Daily	Hourly	Daily
Pearson	0.413	0.76	0.624	0.887
Spearman	0.543	0.819	0.625	0.899
Kendall	0.51	0.719	0.58	0.799

3.3. Comparison HYRAS versus DWD stations

Generally, the HYRAS dataset compares well with DWD stations within the investigation domain. This is not surprising since most of the measurement stations are likely to be part of the HYRAS dataset. Nevertheless, some differences are obvious. Compared to observations, the HYRAS dataset underestimates the percentage of dry days (i.e. days with precipitation below 1 mm) by 3% in summer, while in winter it underestimates the precipitation intensities above 15 mm/day. On the other hand, the gridded dataset tends to present more extreme precipitation in both seasons than the measurement stations. More details and graphs on the comparison between HYRAS and observations can be found in Chapter 5.4.1, especially Figure 30 and Table 8.

4. Sensitivity studies of the model at higher spatial resolution

4.1. Introduction

Within the KLIWA project, long-term simulations need to be provided for selected areas, Weiherbach and Mertesdorf among them. Before performing long-term simulations, it is necessary to make sure that the model gives physically sound results in the area under investigation (Meißner 2008). The performance of the same model can vary substantially depending on several parameters, as for example simulation domain, internal settings, boundary data, and soil initialisation. Moreover, the quality of the simulation can be judged differently depending on the variables under investigation (Bachner et al. 2008; Suklitsch et al. 2008), i.e. the model can represent one variable well while strongly overestimating/underestimating another one.

According to McGregor (1997), the simulation area should be large enough to allow the model to develop independently from the boundary conditions. On the other hand, it should be small enough to guarantee that finer and coarser nests do not differ too strongly in terms of synoptic circulation (Jones et al. 1995). Unfortunately, there is no a clear definition of "enough", which depends also on the area location and characteristics (Seth and Giorgi 1998). Dickinson et al. (1988) suggested avoiding placing the lateral boundary in regions with strong orography. Meißner et al. (2009) found that leaving out the Alps in simulating Germany at 7 km resolution leads to an unrealistic increase in precipitation. In addition to all the above-mentioned suggestions, modellers always strive to keep the simulation domain small in order to save computing time while maintaining satisfying and stable results.

Model parameterisation can also strongly affect the results both in summer and winter (e.g. Giorgi and Mearns 1999; Bachner et al. 2008; Gebhardt et al. 2011; Giorgi et al. 1993; Seneviratne et al. 2002; Vidale et al. 2003). For example, Bachner et al. (2008) found that the uncertainties in the intensity distribution of daily precipitation span from 20 to 50 % depending on the parameterisation. As noted for the simulation domain, it is not possible to define an overall best configuration for the model and the "best setting" always depends on the application. For example, CAPE-based closure in the convection parameterization can be suitable when considering regional averages, but fails in representing the spatial precipitation distribution (Bachner et al. 2008). Meantime, Suklitsch et al. (2008) found that in the Alpine region, the modifications of the domain size and vertical resolution show stronger impacts on both precipitation and temperature than the alteration of the model configuration.

Vidale et al. (2003) underlined the risk of compensating model errors related to the parameterisation, which can lead in some cases to good results for the wrong reason. In this context, different methods are required to detect physical inconsistencies, which might not appear from a superficial analysis. Year, seasons, months or days are the standard temporal scales for the analysis of the model results. Those scales imply a temporal average of the model outputs, which usually have an hourly frequency (usually between one and six hours). In averaging, a compensation of maximum and minimum values can occur, thus hiding important information and possibly leading to false conclusions.

The purpose of the chapter is to define the optimum model condition at 2.8 km resolution to perform long-term simulations in the area around Weiherbach and Mertesdorf. In this context, sensitivity studies on both size and location of the model domain as well as internal model settings are consid-

ered. The focus is on the representation of intense precipitation events as well as the alternation between dry and wet periods, which are the conditions affecting soil erosion the most. Different temporal scales for the analysis of the simulated precipitation are considered to guarantee that the conclusions are not affected by the averaging process and/or from the selected temporal scale.

Section 4.2 contains the description of the methodology used. Chapter 4.3 focuses on the sensitivity study on the location and size of the simulation domain while Chapter 4.4 analyses the effect of different model configurations and several modification of those. The diurnal cycle of precipitation and the problem related to its model representation are presented in Chapter 4.5. The model performances in areas other than Weiherbach are considered in Chapter 4.6. Conclusions are drawn in Chapter 4.7.

4.2. Methodology

Despite various research work on these topics, there is no unique way to set the simulation domain and the model configuration because these parameters strongly depend on the characteristics of investigation area and on the research focus (Bachner et al. 2008; Seth and Giorgi 1998; Suklitsch et al. 2008). Therefore, sensitivity studies are required to test the responsiveness of the model to these parameters.

The sensitivity analysis of this chapter concerns only the simulation at 2.8 km resolution, since previous nests were widely tested for both size and location as well as for the optimisation of the internal model settings (Berg et al. 2012; Meißner et al. 2009; Meißner 2008). More information of the nesting strategy is provided in Chapter 2.7. Figure 8 and Figure 13 show the investigation area (black frame), where the analysis is performed, except where dif-

ferently stated (Chapter 4.6). All the simulations are driven with ERA40 reanalysis data to be close to reality (see Chapter 2.6 for further details). The model outputs are validated mainly against the HYRAS observational dataset (more information in Chapter 3.1).

The sensitivity study follows two steps, each of them focusing on one specific aspect of the model sensitivity. First, a one-year simulation is performed for several domains with different dimensions in order to select the optimum domain size and location (Chapter 4.3). Short simulation periods are often used to evaluate the error characteristics of RCMs (Alexandru et al. 2007; Caya and Biner 2004; Giorgi et al. 2004; Jacob and Podzun 1997; Meiβner et al. 2009; Suklitsch et al. 2008). Then, the domain selected from the first step of the analysis is used to test the model sensitivity to the internal settings (Chapter 4.4). Note that, since all the simulations in this chapter are at 2.8 km resolution, the parameterisation of deep convection is always switched off. The simulations in the second part of the sensitivity study cover a different and longer period, namely five years, to make sure that the results of the first step are not influenced by the specific one-year selected.

The analysis focuses on the precipitation statistics since rainfall is the variable affecting soil erosion the most. Besides precipitation, this phenomenon is strongly affected by the soil characteristics, the land use and the vegetation coverage. Under the same precipitation event, a bare soil usually generates higher erosion than a covered one. A full analysis of the erosion within the Weiherbach catchment is outside the purpose of this chapter and this thesis in general. However, it is important to make sure that the model is able to simulate seasons with different soil situations.

Figure 12 compares hydrological summer (i.e. from May to October included) and winter (i.e. from November to April included) in terms of occurrence

of precipitation events with different hourly thresholds (namely above 5, 10, 15 mm/hour). The data refer to Kraichtal gauge station but similar results are also found for Eppingen (not shown). These two stations are the closest to Weiherbach and are both active between 1986 and 1992. From the figure, it is clear that the precipitation tends to be more intense and recurring in hydrological summer compared with the rest of the year. Thus, this chapter in contrast to the rest of the thesis, that analyses only JJA and DJF, focuses on the hydrological summer.

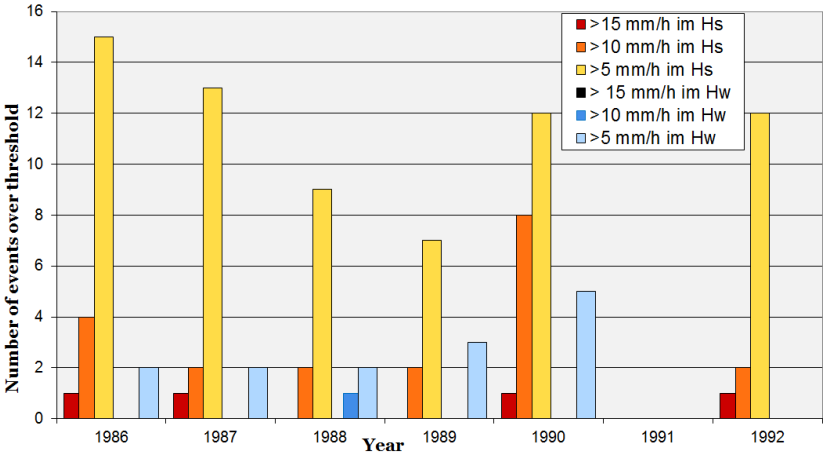

Figure 12: Number of precipitation events for different hourly thresholds (namely above 5, 10, 15 mm/hour) registered in Kraichtal measurement station between 1986 and 1992. Blue (orange) colours represent the hydrological summer, Hs (hydrological winter, Hw).

4.3. Sensitivity studies on the location and size of the simulation domain

To test the sensitivity of the model to the size and location of the simulation area, three domains are selected (Figure 13).

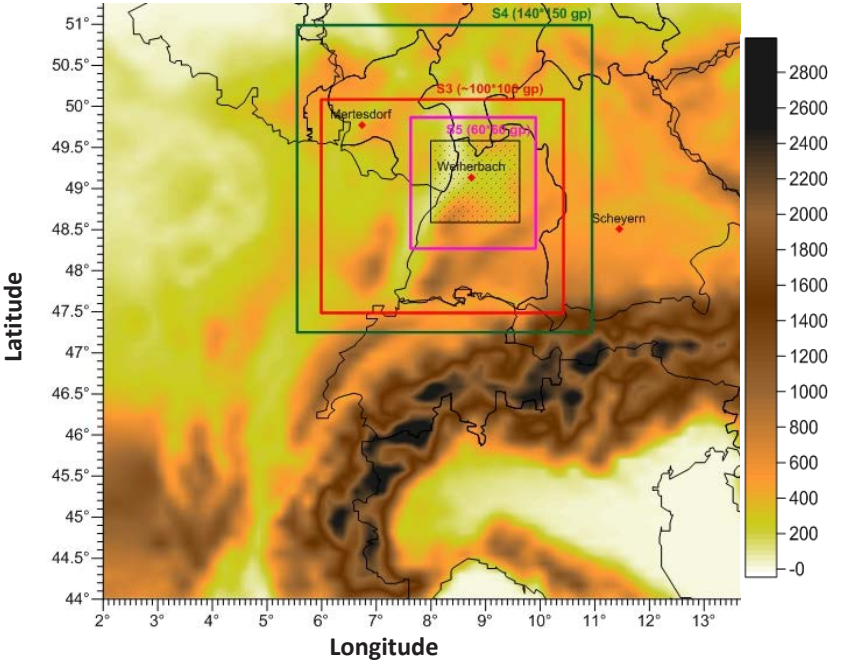

Figure 13: Map of Central Europe showing the three simulation domains (S5, pink; S3, red; S4, green) used in the sensitivity study and the investigation area (black frame). The red points indicate the erosion prone areas selected within the KLIWA project, i.e.Mertesdorf, Weiherbach, and Scheyern.

The S5 domain represents the 'minimum' simulation area since it is ten grid points in each direction larger than the investigation area, i.e. almost the minimum relaxation zone recommended by Doms (2011). The S3 domain exceeds S5 in order to include the entire Rhine valley (westward), the Black Forest and the Swabian Jura (southeastward) and Eifel and Hunsrück (north-

eastward). This selection includes the area from where dominant winds come and thus regional-scale effects should be more accurately represented. The largest domain, S4, covers the southwestern part of Germany, Luxemburg and part of France. Moreover, it embraces also the Mertesdorf area with more than ten grid points westward and northward so that no additional simulation is required for this location.

The selection of the simulation year is based on Kraichtal and Eppingen data since these measurement stations are the closest to Weiherbach and thus reflect best the situation of the catchment. The modelled year needs to fulfil several conditions:

- Presence of intense events, which are main drivers for erosion
- High variability between dry and wet periods; the model can have some difficulties in simulating quick alternations of these states
- Wet February-March period to best initialize the model in terms of soil memory

The year 1986 satisfies the above-specified perquisites and presents the highest number of events above 30 mm/day, namely four, which is the threshold established within KLIWA project as hazardous for erosion. Therefore, the domains S3, S4 and S5 are simulated for this year to decide the optimum location and size of the simulation domain.

Figure 14 shows the daily mean precipitation bias between the different simulation domains (S5 domain, top; S3, middle; S4, bottom) and HYRAS dataset for the hydrological summer 1986. All the simulation domains present the same pattern, with drier conditions in the south (between 34% for S4 and 42% for S5) and a wetter area in the northwest side of the investigation area (between 81% for S4 and 50% for S5). S5 domain performs the worst among the others with a large region of underestimation. When only wet days (i.e. day with precipitation above 1 mm/day) are considered, the model accentuates the wet bias while reducing the dry region.

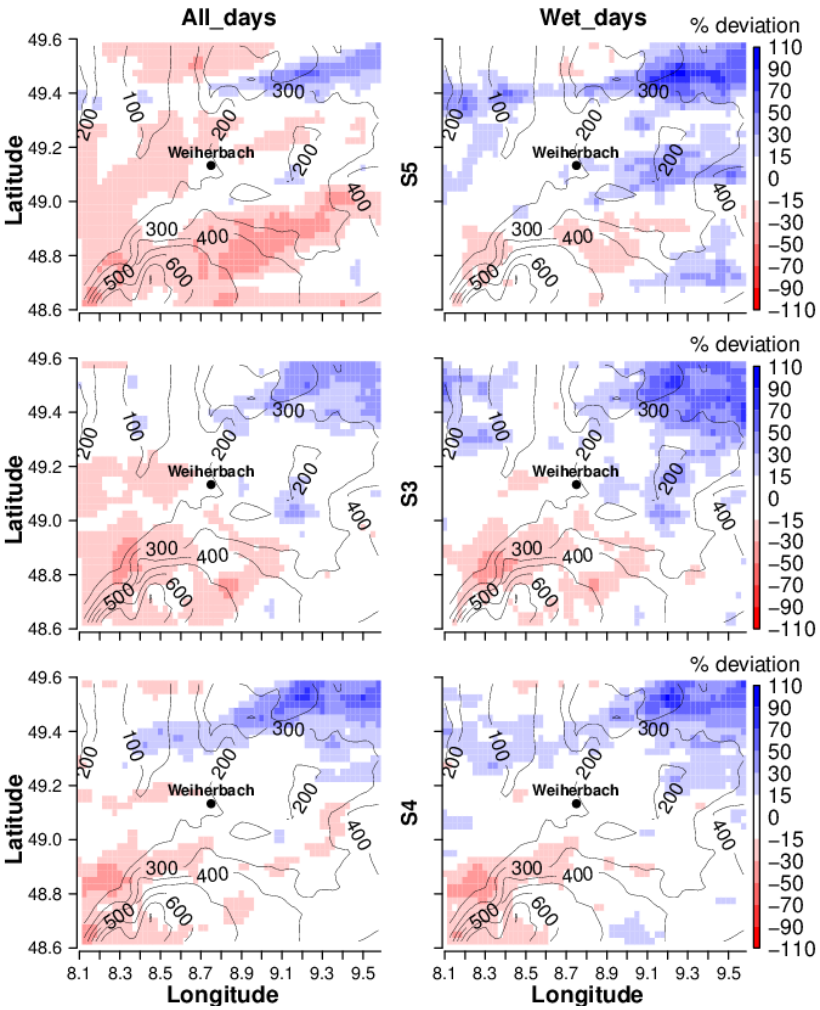

Figure 14: Spatial distribution of the differences in daily mean precipitation between model simulations (domain S5, top; S3, middle; S4, bottom) and HYRAS dataset for hydrological summer 1986, considering all days (left), and only wet days (right). Blue (red) grids show the model overestimation (underestimation). The contour lines represent the orography of the area.

Although from Figure 14 one would conclude that S4 performs best, the Taylor diagram in Figure 15 provides a different conclusion from the results. The Taylor diagram shows the relative skill, with which the model simulates the spatial distribution of daily mean precipitation calculated for the hydrological summer of 1986 compared to observations. The spatial correlation, readable on the arc, quantifies the similarity between the different simulation patterns and HYRAS data. The standard deviation, on the axes, represents the amplitude of the variations of the real data normalized with the observed standard deviation. In this case, S5 domain has a higher spatial correlation compared to S4 (0.7 versus 0.6), while the standard deviation is similar for both of them. Thus, one would conclude that S5 best represents the HYRAS dataset in terms of precipitation spatial pattern.

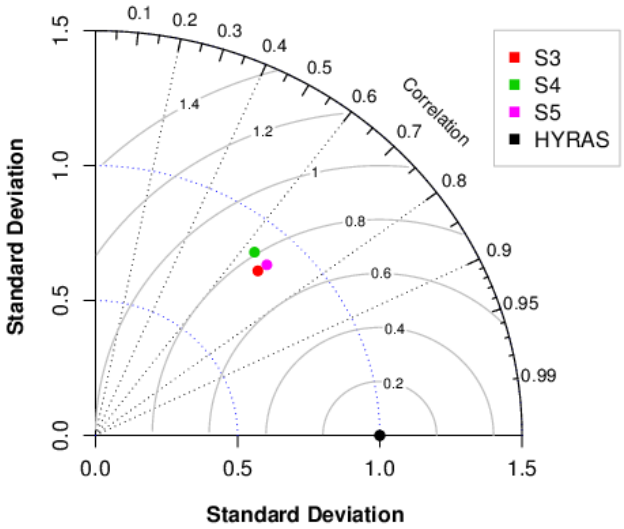

Figure 15: Taylor diagram for S5 (pink), S3 (red) and S4 (green) domain versus HYRAS data in hydrological summer 1986.

Up to now the analysis considered only mean values of precipitation while erosion is mainly sensitive to intense precipitation events as well as the al-

ternation between dry and wet periods. Moreover, the averaging process smoothes extremes and can lead to a wrong interpretation of the results.

The World Meteorological Organization (WMO) suggested the use of indices to easily evaluate extremes (Klein Tank et al. 2009; Zhang et al. 2011). Following WMO recommendation, Figure 16 shows how the different simulation domains perform in representing the number of events above 1, 10, 20 mm/day in comparison with HYRAS dataset. Note that this figure gives no indication as to the location of these types of precipitation. S5 domain highly underestimates the number of wet days and this is probably the reason for the dry bias observed in Figure 14 (top left). On the other hand, it shows a good agreement with HYRAS for precipitation above 20 mm/day. S3 and especially S4 well represent the observational dataset for the full range of selected thresholds.

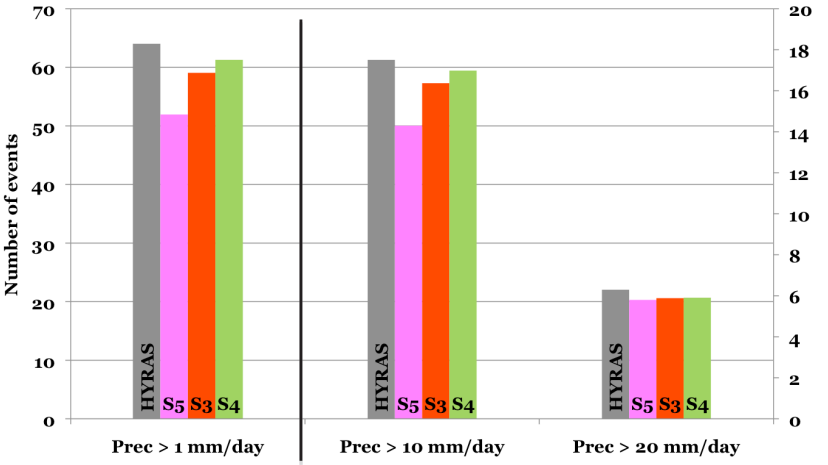

Figure 16: Number of events above 1, 10, 20 mm/day, averaged over the investigation domain, of the different simulation domains (S5, S3, S4) and HYRAS dataset in hydrological summer 1986. The first set of bars on the left refers to the vertical axis on the left; the second and third set to the vertical axis on the right.

Table 5: Time needed to simulate different domains depending on the spatial resolution.

Domain	Spatial resolution [km]	Grid points	Simulation area [km]	Time needed to simulate one year [hour]
Whole Germany	7	165 * 200	1155 * 1400	18
S5	2.8	60 * 60	168 * 168	14
S3	2.8	100 * 100	280 * 280	25
S4	2.8	140 *140	392 * 392	33

In choosing the simulation domain, the computational time and the storage capacity need to be taken into account because of the constraints they can generate. The last column of Table 5 shows the time needed to simulate one year for the domains S5, S3 and S4 in comparison with a coarser resolution (i.e. 7 km). Increasing spatial resolution augments substantially the computational requirement both in terms of time and memory space.

In conclusion, none of the domains outperforms the others. S4 better represents the number of dry days and more intense events, but it shows a lower spatial correlation and it requires high computational costs. Since these are crucial when performing a large number of sensitivity tests, as done in the following, the S5 domain is selected for further investigation on model settings. Nevertheless, its spatially large dry bias needs to be taken into account in analysing the following results. An additional simulation of the large domain S4 with the selected model configuration will be necessary to understand how the results transfer to a bigger area.

4.4. Sensitivity studies on the model internal settings

The sensitivity studies on the model internal settings use only the S5 domain, which was selected in the previous chapter among the simulation areas. The model runs for a different and longer period, namely 1980-1984, to make sure that the previous findings, for the selection of the simulation domain (Chapter 4.3), were not influenced by the choice of the specific year (i.e. 1986). Note that for all the simulations the parameterisation of deep convection is switched off, since all of them are at 2.8 km resolution.

Two reference configurations are considered (Table 6 in yellow):

- IMK_TRO, consistent with the run at the coarser resolution, i.e. 7 km, in which the 2.8 km run is nested
- COSMO_DE, elaborated according to the advice on high-resolution simulations from DWD and Climate Limited-area Modelling, CLM, Community.

Table 6: Overview of the sensitivity studies on model internal settings. The reference configurations are marked in yellow.

Simulation name	Setup	External dataset	Boundary update
IMK_TRO	consistent with coarser resolution	CLM	6 h
IMK_Tur_len	IMK_TRO + + reduced asymptotic turbulence length scale		
IMK_HINC_3h	IMK_TRO + + more frequent update of the boundary conditions		
COSMO_DE	consistent with COSMO_DE	CLM	6 h
DE_HZG	COSMO_DE + external dataset from HZG		
DE_HINC_1h	COSMO_DE + + more frequent update of the boundary conditions		

The following changes to the reference configurations are also considered:

- More frequent update of the boundary conditions both for IMK_TRO and COSMO_DE (see also Chapter 2.6). This leads to a stronger connection between the coarser and the finer resolution. In other words, this means that the merits and the blemishes of the 7 km are likely to become more evident in the 2.8 km outputs. The runs are called respectively IMK_HINC_3h and DE_HINC_1h and the boundaries conditions are updated respectively every three and one hour versus the six hours of the reference configurations.
- Use of a different the external dataset, namely HZG_PEP, for COSMO_DE configuration. The external dataset, i.e. PEP, contains information like land use, soil type, topography, etc. IMK_TRO uses the PEP provided by the CLM Community; the Helmholtz Zentrum Geesthacht, HZG, created its own dataset for external parameters. The two PEPs are based on different maps; in particular, for the calculation of Leaf Area Index and Vegetation Area Fraction, CLM Community and HZG use GLC2000 and ECOCLIMAP maps, respectively. The latter is more accurate since both vegetation parameters change throughout the whole year, and not only between April and October, as in the case of CLM dataset (Figure 17).

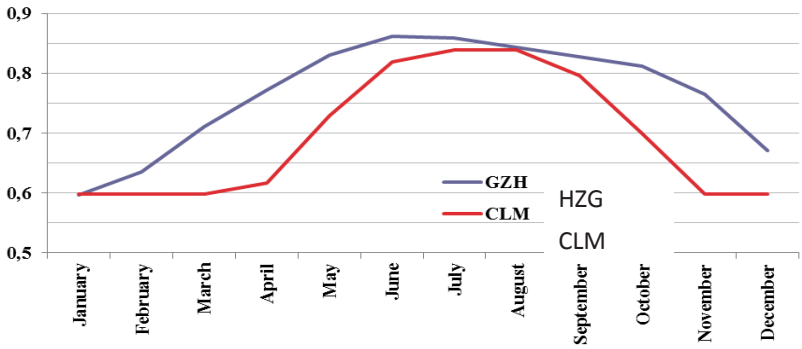

Figure 17: Vegetation Area Fraction index along the year for the GZH (blue) and CLM Community (red) dataset.

- Reduced asymptotic turbulence length scale l∞ (Blackadar 1962) of the turbulent mixing length l for IMK_TRO configuration. According to Baldauf et al. (2011), a reduced asymptotic turbulence length fosters the initialization of convection and can therefore lead to an improvement in the representation of convective precipitation. Note that the COSMO_DE configuration already includes this recommendation.

In Figure 18 the different model configurations are compared with HYRAS data in terms of number of wet days (P>1 mm per day), of heavy precipitation days (P>10 mm per day) and of very heavy precipitation days (P>20 mm per day), according to WMO suggestions (Klein Tank et al. 2009; Zhang et al. 2011).

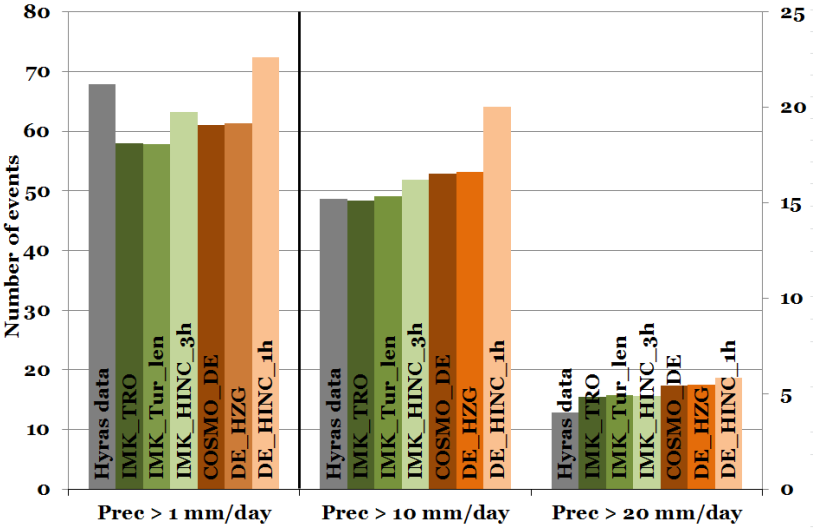

Figure 18: Number of events above 1, 10, 20 mm/day, averaged over the investigation domain, of simulations with different configurations and HYRAS dataset.The values are yearly means calculated for the hydrological summers between 1980 and 1984. The first set of bars on the left refers to the vertical axis on the left; the second and third set to the vertical axis on the right.

As already seen in Chapter 4.3, all the runs performed on the small S5 domain systematically underestimate the number of wet days. The only exceptions to this behaviour are found for the simulations with a more frequent update of the boundary conditions, namely DE_HINC_1h and, to less extent, IMK_HINC_3h. According to Berg et al. (2012), a wet bias affects the results at 7 km, in which 2.8 km is nested. Through a more frequent update of boundary conditions, the characteristics of the coarser resolution get a stronger impact on the nested simulation; this causes a substantial decrease of the dry days. Moreover, it leads to a clear overestimation of the number of heavy and very heavy rainfall for DE_HINC_1h, which is thus not suitable to represent Weiherbach catchment. Besides the latter configuration (i.e. DE_HINC_1h), the model captures well the frequency of high and very high precipitation days (P>10 mm and >20 mm/day), especially for the IMK configurations (Figure 18). Although the number of these events never exceeds observations by more than 1-2 events per year, there is an overestimation of the number of five-days periods with a total precipitation above 50 mm, which is for all simulations almost double that which is registered (not shown).

Figure 19 shows the highest one-day precipitation amount simulated by the model, with different configurations, during the hydrological summers between 1980 and 1984. Somewhere within the investigation domain, the model clearly overestimates this quantity up to double its real value for the COSMO_DE configuration. Although the graph strongly depends on the period selected and no overall conclusions can be drawn from it, it shows that results can differ strongly depending on the area of the investigation domain on which the focus is. Therefore an analysis of the spatial distribution of the extreme precipitation is crucial to determine the preferable model configuration.

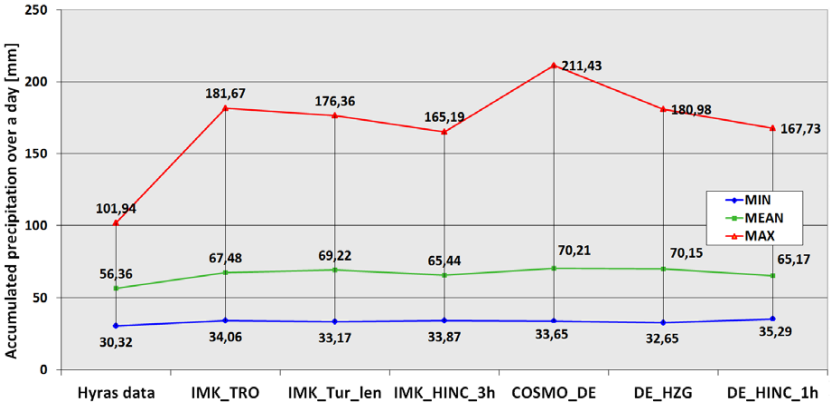

Figure 19: Highest one-day precipitation amount over the whole investigation area, between 1980 and 1984, for different model configurations and HYRAS dataset. The blue, green and red lines represent respectively the minimum, mean and maximum one-day precipitation over the domain.

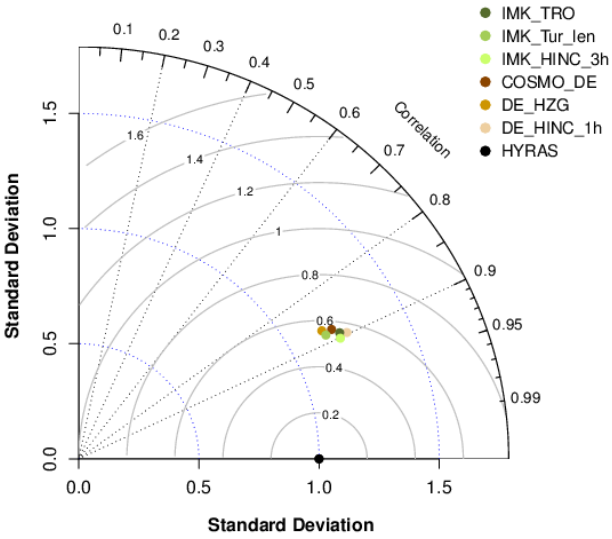

Figure 20: Taylor diagram for the different model configurations and HYRAS data for the hydrological summers between 1980 and 1984.

In the following, only the bias maps of IMK_TRO and IMK_HINC_3h configurations are presented (Figure 21). In fact, the reduction in the asymptotic turbulence length scale (IMK_Tur_len configuration) does not seem to have a remarkable effect in comparison with the reference IMK_TRO run, as well as the different external dataset from HZG (DE_HZG configuration) with respect to the reference COSMO_DE simulation. DE_HINC_1h configuration had already been excluded because of its wetness (Figure 18). Between the reference configurations COSMO_DE and IMK_TRO, the latter best represents extremes while the number of wet days is comparable with the former (Figure 18). Moreover, the Taylor diagram shows that IMK_TRO and IMK_HINC_3h have slightly better spatial correlation with the HYRAS dataset compared to the other configurations (Figure 20).

At the top, Figure 21 shows the spatial difference in daily mean precipitation between model simulations (IMK_HINC_3h configuration, on the left; IMK_TRO, on the right) and HYRAS data considering all days. Probably linked to its higher number of dry days (Figure 18), the IMK_TRO reference configuration presents a more extensive area of underestimation of the mean precipitation compared to the IMK_HINC_3h configuration. In addition, this dry region is pretty close to the boundaries of the Weiherbach catchment. On the other hand, the overestimation is limited in both cases (IMK_TRO and IMK_HINC_3h) to the hilly area, with an altitude above 500 m, in the southern part of the investigation domain. When all days are considered in the calculation of daily mean precipitation, very wet and dry periods tend on average to compensate each other. This can lead to a wrong interpretation of the results due to the artificial good agreement with observations in terms of daily mean. Thus, in Figure 21, middle row, the spatial bias is calculated only for wet days (P>1 mm). Compared to HINC_TRO_1h, IMK_TRO presents a higher and spatially amplified overestimation of precipitation, although this configuration underestimated the number of wet days more than

IMK_HINC_3h (Figure 18). This means that the reference IMK configuration has too many dry periods and, when it rains, it rains systematically slightly more than in the observational dataset; therefore, the number of wet days as well as the number of events above 10 and 20 mm is in line with HYRAS data but the mean precipitation for wet days is too high.

In presenting Figure 19, it was noticed that the model was overestimating the highest one-day precipitation amount as well as the number of five-day periods with a total precipitation above 50 mm in some areas of the investigation domain. Figure 21 bottom shows where this problem occurs. The figure displays the spatial difference in the number of very heavy precipitation (P>20 mm/day) between the model (IMK_HINC_3h, left; IMK_TRO, right) and HYRAS. The major bias is localized on the hilly area above 500 m at the beginning of the Black Forest and thus it does not affect the Weiherbach catchment; the same can be stated referring to the number of very severe precipitation periods (not shown).

The precipitation characteristics important for erosion are frequency and intensity of extreme events as well as the alternation of dry and wet periods. The configuration that, among the others, best captured the above-mentioned precipitation characteristics is IMK_HINC_3h. Since this configuration is consistent with the coarser resolution, it will also be possible to compare the two different resolutions. Therefore, IMK_HINC_3h settings are used to simulate also the large domain S4 (see Figure 13) to verify if a bigger domain can also solve the problem of underestimation of wet days shown in Figure 18.

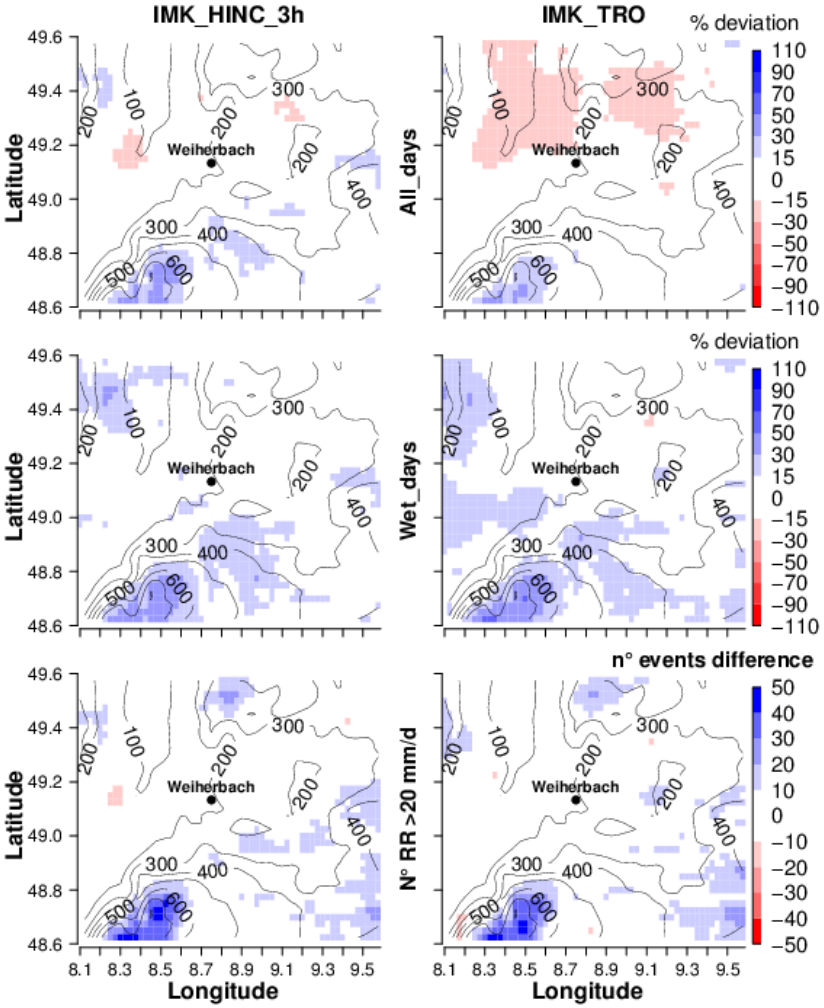

Figure 21: Spatial distribution of the differences for the hydrological summers 1980-1984 between the model simulations (IMK_HINC_3h, left; IMK_TRO, right) and HYRAS data in: top (middle) pannel daily mean precipitation considering all days (only wet days), bottom panel, the number of very heavy precipitation (P>20 mm/day). Blue (red) grids show the model overestimation (underestimation). The contour lines represent the orography of the area.

4.5. Diurnal cycle

Before concluding the sensitivity study, the diurnal cycle of precipitation is investigated for summer. According to the analysis performed on the measurement stations (Chapter 3.2), the diurnal cycle in JJA has a very characteristic pattern with a maximum precipitation in the afternoon between 15:00 and 17:00 (Figure 11 right in Chapter 3.2). This peak is mainly due to convective processes (more details on convection in Chapter 2.4).

Most of the RCMs have problems in representing convective precipitation, which usually occurs too early in the day and with overestimated amplitude of its diurnal cycle (Brockhaus et al. 2008; Dai 2006; Dai and Trenberth 2004; Yang and Slingo 2001). Previous studies recognized in the convective parameterizations a major source of uncertainties and errors causing, among others, a misrepresentation of the diurnal cycle of precipitation (Bechtold et al. 2004; Brockhaus et al. 2008; Hohenegger et al. 2008). Increasing spatial resolution to 2.8 km allows switching off the parameterisation and this should lead to a more consistent representation of the atmospheric fields related to convection (Baldauf et al. 2011; Fosser et al. 2014). The next chapter investigates in detail the added value of higher versus coarser resolution using long term-simulations. Here the goal is to make sure that the selected model settings and the domain selected for the simulations at 2.8 km resolution offer a good representation of the diurnal cycle of precipitation.

The observational diurnal cycle is derived from 48 measurement stations active in the investigation area between 1997 and 2004, a period with the highest number of available stations with a stable density (see Chapter 3.2). For this reason, this period is selected, although it does not overlap with the simulated one (1980-1984). The shape of the precipitation diurnal cycle is not expected to change over time if there is not a strong climate change

signal. In Figure 22 the observations show a maximum precipitation in the afternoon between 15:00 and 17:00 followed by a secondary peak in the evening around 21:00.

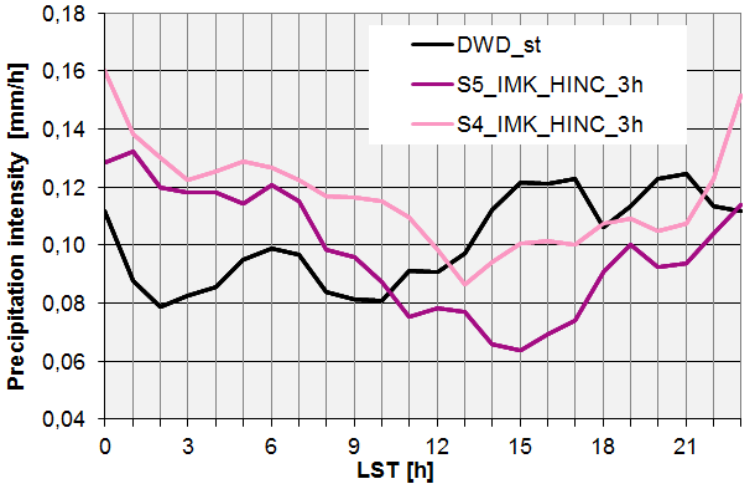

Figure 22: Diurnal cycles of precipitation for observations (black line) in JJA 1997-2004 and model simulations for JJA 1980-1984. The model simulations are performed over different domains (S5, purple and S4, pink; see Figure 13) but have the same settings, namely IMK_HINC_3h (see Table 6).

The figure displays also the diurnal cycle of S5 and S4 domains simulated using the selected configuration, the same for both simulations (consistent with the coarser resolution and update of boundary conditions every three hours, namely S5_IMK_HINC_3h and S4_ IMK_HINC_3h). Both domains have a similar pattern and both misrepresent the diurnal cycle completely, showing too much precipitation in the morning and no peak in the afternoon. Note that this overestimation and underestimation of hourly mean precipitation compensated each other in the calculation of the daily mean precipitation, leading to a limited bias on a daily basis compared with the observational dataset (see 21). Thus, to assess the quality of the simulation results

at convection-permitting scale, a sub-daily temporal scale should always be used for the analysis because coarser temporal resolution can lead to a misinterpretation of the results. Figure 22 also shows the impact of the domain size on the hourly mean precipitation that increases for larger domains (as S4 compared to S5).

In order to understand what generates the error in the diurnal cycle, a new simulation, called S4_new, is performed on the S4 domain (Figure 23 in green). The precipitation diurnal cycle with this new configuration shows a peak between 15:00 and 17:00 and a smaller one at 21:00 in good agreement with observations, despite a third peak too early in the morning. Although the absolute values are still overestimated, the shape is very similar between S4_new and stations data, while it is completely different from S4_IMK_HINC_3h (Figure 22 and Figure 23 in pink).

The two model simulations (S4_new and S4_IMK_HINC_3h) differ in the frequency of the update of the boundary conditions (6 hours in S4_new) and some model settings, namely tuning parameters and the frequency in the call of the radiation scheme. Each of the latter parameters was investigated through a one-year simulation to detect the possible responsible for such a strong change in the diurnal cycle of precipitation as seen in Figure 22. None of the parameters generate the error, which thus probably derives from a combination of them.

Figure 23 shows an additional run, called S4_new_HINC_3h in blue. The latter has the same settings as S4_new but a more frequent update of the boundary conditions (namely 3 hours versus the previously used 6 hours). Figure 18 showed that a more frequent update of the boundary conditions leads to an increase in the number of wet days, which compensated the underestimation of wet days in the S5 domain. Now Figure 23 shows that this

option generates an excess of precipitation, especially in the early morning, and thus it is not a viable configuration.

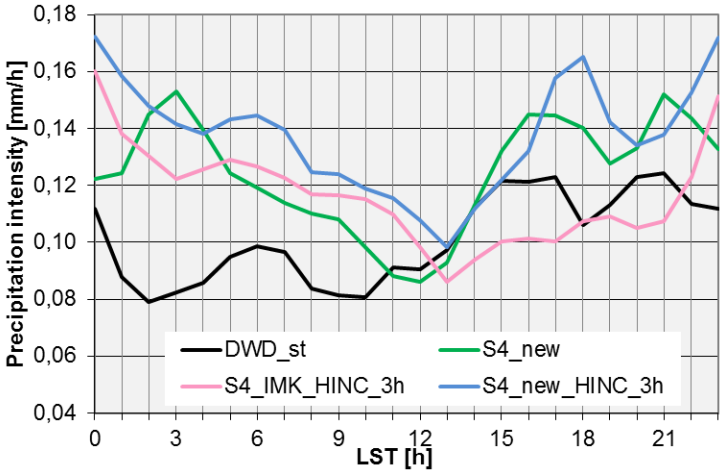

Figure 23: Diurnal cycles of precipitation for observations (black line) in JJA 1997-2004 and model simulations for JJA 1980-1984. The model simulations are performed over the same domain (S4; see Figure 13) but have different model configurations. In particular, the diurnal cycle for S4_IMK_HINC_3h (pink) is the same than in the above panel (i.e. configuration IMK_HINC_3h); S4_new (green) has the new settings in green; and S4_new_HINC_3h (blue) has the new settings (as S4_new) and the update of boundary condition every 3 hours instead of 6 hours as for S4_new.

S4_new has a more extended wet bias compared with the previously selected configuration (S5 domain with IMK_HINC_3h configuration), both considering all days and only wet days (Figure 24). On the other hand, S4_new simulates the shape of the diurnal cycle of precipitation well, especially the convective peak in the afternoon. This is of crucial importance because it presumes a correct simulation of the physical process leading to it. Thus, this simulation domain and configuration are selected for the long-term simulations used in the following chapters.

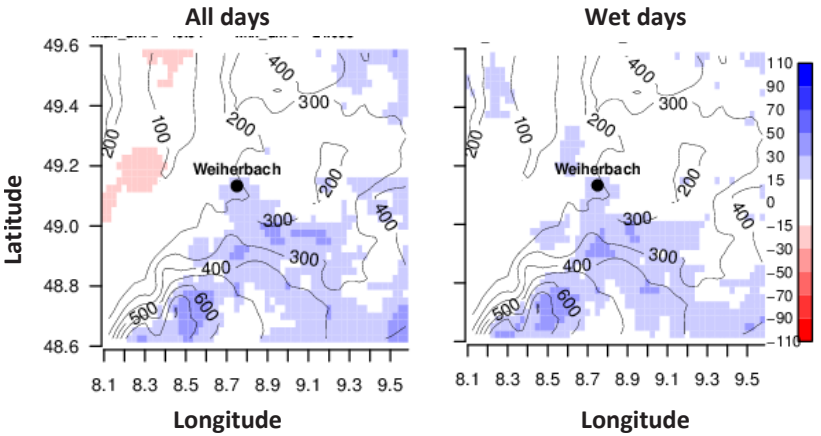

Figure 24: Spatial distribution of the differences (in percent) in daily mean precipitation between model simulation (S4_new) and HYRAS dataset for hydrological summers 1980-1984, when considering all days (left panel) and only wet days (right panel). Blue (red) grids show the model overestimation (underestimation). The contour lines represent the orography of the area.

4.6. Performance in different locations

Model simulation can give good results in certain regions but fail in others. This is particularly true in an area with strong orographic characteristics or weather patterns (Barthlott et al. 2010). The model can be configured to deal with the specific issues of a selected location but then do not provide the same performance as in other regions Seth and Giorgi 1998).

Within the KLIWA project, the long-term simulations will also be used for different locations besides Weiherbach. It is thus important to check how the model performs in other regions. For this purpose, two additional areas are selected from the simulation S4_new (Figure 25). The first covers Mertesdorf and the erosion-prone areas located in the eastern part of the state of Rheinland-Pfalz (personal communication with Dr. Billen from BodenGut).

The second is located in the middle of the Black Forest, orographically completely different from those previously considered.

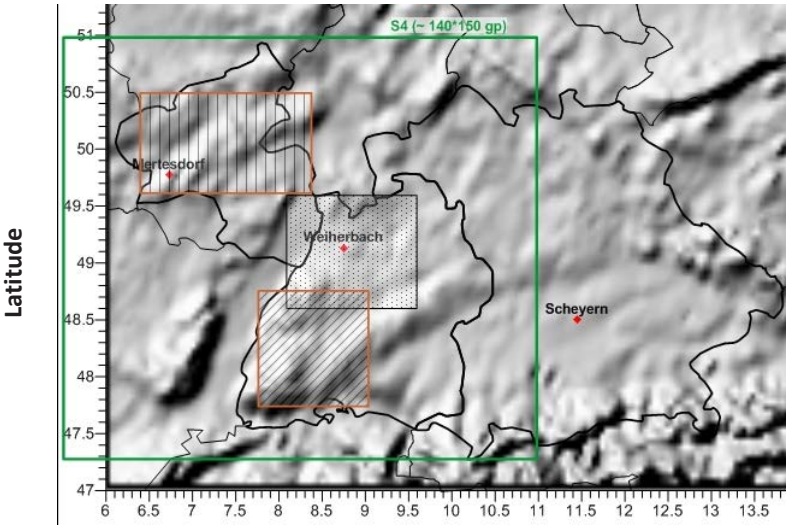

Figure 25: Map of southern part of Germany showing the simulation domain S4 (green box), the standard investigation area (black frame) and two additional areas respectively covering Mertesdorf and the Black Forest. The red points indicate the erosion prone areas selected within the KLIWA project, namely Mertesdorf, Weiherbach, and Scheyern.

Figure 26 shows the differences in daily mean precipitation between the model simulation and the HYRAS data considering all days (left) and wet days only (right) for the Mertesdorf (top) and Black Forest area (bottom). The former is well simulated especially when considering only wet days (top panel left). In this case, the bias limited to ±15% outperforms the results obtained for the Weiherbach investigation area in Figure 24. By contrast, the Black Forest shows an extended overestimation of mean precipitation, both with and without consideration of the dry days. This is probably linked to a steeper orography that can act as trigger for precipitation.

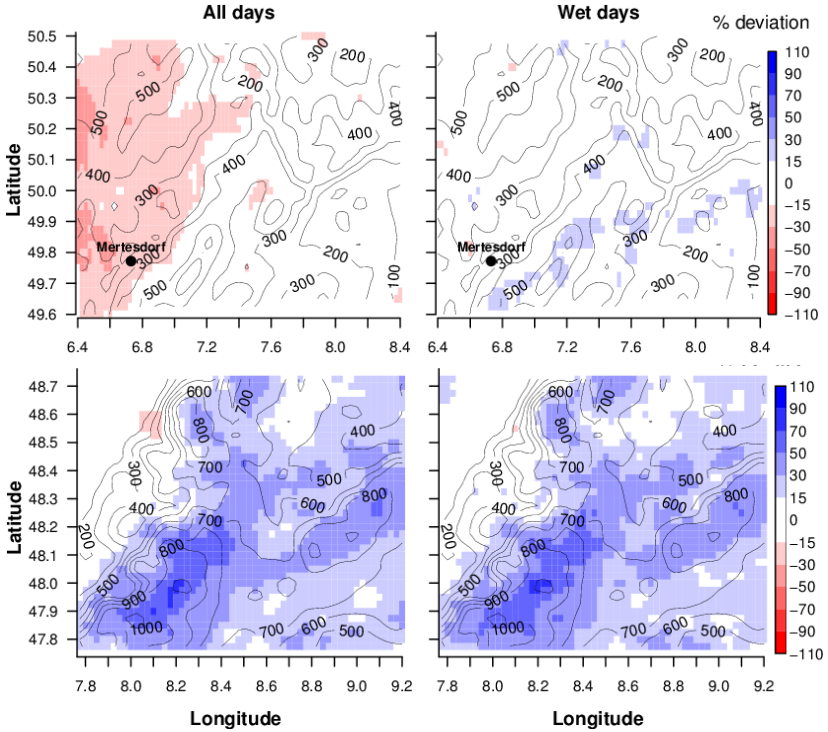

Figure 26: Spatial distribution of the differences (in percent) in daily mean precipitation between model simulation (S4_new) and HYRAS dataset for hydrological summers 1980-1984, when considering all days (left panel) and only wet days (right panel). The top row shows an area around Mertesdorf, while the bottom row an area in the south of the Black Forest. Blure (red) grids show the model overestimation (underestimation) of daily mean precipitation. The contour lines represent the orography of the area.

The probability distribution in Figure 27 confirms the findings above. For the Mertesdorf area, all the modelled precipitation intensities up to 40 mm/day are very close to the HYRAS dataset, while the percentage of dry days is overestimated by 4%. This explains both the small bias when only wet days are considered (Figure 26 top right) and the dryness, when including also dry days (Figure 26 top left). The latter are better simulated for the standard in-

vestigation area, namely Weiherbach, but the model overestimates precipitations above 20 mm/day, which might explain the bias in Figure 24. In the Black Forest region, the model performs well in terms of dry days probability, but it highly overestimates precipitation intensities above 10 mm/day.

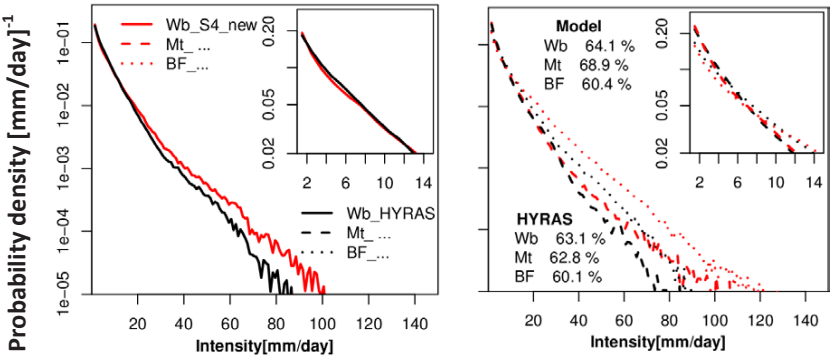

Figure 27: Probability distributions of precipitation intensities comparing between HYRAS data (black) and model simulation (red) for the hydrological summers in 1980-1984. The investigation areas considered are Weiherbach (Wb, solid lines), Mertesdorf (Mt, dashed lines) and Black Forest domain (BF, dotted lines). The percentages in the graphs represent the percentage of dry days for the specific dataset.

4.7. Summary and conclusion

Within the KLIWA project, long-term simulations at convection-permitting scale are required as input for the erosion modelling. In this context, it is important that the model is able to simulate the alternation between dry and wet periods and especially the intense precipitation events. Since the latter occur mainly during the hydrological summer, this is selected as investigation period throughout the whole of Chapter 4. The model is sensitive to the domain size and location as well as to the internal settings. Thus, a set of sensitivity studies is performed to find the optimum configuration of the model at 2.8 km resolution before starting long-term simulations. The simulations in this chapter uses ERA40_reanalysis as driving data and the simu-

lated precipitation is compared mainly with the observational HYRAS dataset remapped on 2.8 km grid.

In order to investigate the influence of the domain size and location, three domains are selected and simulated with the same internal settings for one year. Their size varies from 60*60 grid points to more than double. The analysis shows that a too small domain leads to an underestimation of the number of wet days and of heavy precipitation, i.e. precipitation above 10 mm/day. Despite this limitation, the second round of sensitivity tests is performed on the small domain in order to save computational time. To test the sensitivity of the model to the internal setup, two reference configurations are considered and simulated for a five-year period. The first, called IMK_TRO, is consistent with the coarser resolution, in which 2.8 km is nested; the second, called COSMO_DE, follows the recommendations of DWD and CLM community on high resolution modelling. Moreover, a more frequent update of the boundaries conditions is considered for both the reference configurations. In addition, two more simulations are analysed. One, based on COSMO_DE configuration, uses a more detailed external dataset; the other one, based on IMK_TRO configuration, considers a reduced asymptotic turbulence length scale. The latter two options do not show any strong difference in comparison with their reference configurations. On the other hand, a more frequent update of the boundary conditions leads to a strong increase in the number of both wet days and of the heavy precipitation. The configuration called IMK_HINC_3h, consistent with the coarser nest and with an update of the boundary conditions every three hours (instead of six), is the one that best simulates both the frequency and the intensity of extreme precipitation events as well as the alternation of dry and wet periods. Moreover, the bias in daily mean precipitation is limited to ±15%.

Stepping from daily scale to hourly scale reveals completely different results. The analysis focuses on the summer diurnal cycle of precipitation, which should be well represented by RCMs at convection-permitting scale since the parameterisation of deep convection is switched off at this spatial scale (Bechtold et al. 2004; Brockhaus et al. 2008; Hohenegger et al. 2008). Contrary to our expectations, the selected IMK_HINC_3h configuration fails to reproduce the observational diurnal cycle, generating a remarkable excess of precipitation in the early morning and entirely missing the convective peak in the afternoon. The first problem is linked to a more frequent update of the boundary conditions, and the second to the specific internal settings used. The largest simulation domain produces higher mean hourly precipitation, but presents the same deficiencies as the smallest domain. The higher temporal scale used for this analysis reveals physical inconsistencies generated by the changes in the model settings, which were not visible on a daily scale. In fact, the precipitation overestimation in the morning and underestimation in the afternoon compensate each other leading to a misleading small bias in daily mean precipitation. Thus, coarser temporal scale for the analysis of the simulated precipitation can hide important information and lead to false conclusions, as hypothesized at the beginning of the chapter. Instead, an hourly temporal scale better guarantees that the results are good for the right reason.

The modification of some parameters of the model settings and an update of the boundary conditions of six hours allow reproduction of the shape of the observational diurnal cycle of precipitation. With this new model configuration, the largest domain is selected to perform the long-term simulations since it represents the number of wet days and of heavy precipitation better than the smallest domain. The bias in daily mean precipitation of this new simulation is around 30% compared to the HYRAS observational dataset.

5. Investigation of the added value of higher versus coarser spatial resolution

5.1. Introduction

In the context of adaptation strategies, there is an increased interest in high resolution climate model simulation (Christensen et al. 2007). Hydrological river catchment and erosion models generally need meteorological forcing data with at least hourly resolution and a spatial resolution of few kilometres (Berg et al. 2012; Michael et al. 2005). Increasing spatial resolution from 50 to 25 or 7 km resolution (Boberg et al. 2010; Berg et al 2013 respectively) leads to an improvement of precipitation daily statistics at least in terms of probability density functions. However, at these resolutions models struggle to correctly represent convective precipitation (Bechtold et al. 2004; Brockhaus et al. 2008; Dai and Trenberth 2004; Yang and Slingo 2001).

A realistic representation of moist convection is a very difficult task for RCMs since it involves complex interactions between the surface, the boundary layer, and the free troposphere, such as surface fluxes, turbulence, condensation processes and cloud–radiation relations. For instance, an overestimation of cloud cover could reduce the heating derived by solar heating and cause an underestimation of surface temperature, which in turn would be responsible for a suppression or delay of convection initiation (Baldauf et al. 2011; Brockhaus et al. 2008). Convection acts on a scale of few kilometres, while the typical grid resolution for RCMs simulations ranges between 5 and 50 km. Thus, RCMs at these spatial resolutions need a parameterization to represent this phenomenon. Previous studies recognized in the convective parameterizations a major source of uncertainties and errors causing, among others, a misrepresentation of the diurnal cycle of precipitation (Bechtold et al. 2004; Brockhaus et al. 2008; Hohenegger et al. 2008).

Convection-permitting scale (i.e. a spatial resolution below 3 km) gives the possibility to resolve explicitly deep convection. Moreover, higher spatial resolution leads to a more detailed representation of orography and surface fluxes, crucial for the initiation of convection (Hohenegger et al. 2008). Several studies show the benefits of convection-permitting scale in the representation of the precipitation field, mainly when moist convection and/or regions with steep orography are involved (Baldauf et al. 2011; Grell et al. 2000; Hohenegger et al. 2008; Mass et al. 2002; Miura et al. 2007; Richard et al. 2007; Roberts and Lean 2008; Schwartz et al. 2009; Weusthoff et al. 2010). Lately, Prein et al. (2013) found that the improved representation of the diurnal cycle of summer precipitation and of the extreme precipitation events is directly due to the possibility of switching off deep convection parameterization rather than to higher resolved orography.

Because of the very high computational cost of high-resolution simulations, all the above-mentioned literature concerns NWP simulations or is limited to a season. The results of these types of studies strongly depend on the specific planetary boundary condition of the selected month (Hohenegger et al. 2009) and do not account for the possible improvements due to a better resolved soil-atmosphere interaction processes (Prein et al. 2013). In this context, long-term simulations are necessary to reach a sound conclusion on the possible benefits of convection-permitting scale in comparison with coarser resolution independently from the specific chosen period.

This chapter tries to overcome the limitation of NWP knowledge on convection-permitting scale using two climatological model simulations of 30 years each, performed with CLM. The first one has a spatial resolution of 7 km and utilises the complete parameterisation of convection according to (Tiedtke 1989); in the second, at 2.8 km resolution, most moist convective parameterisations are turned off. Initially the analysis explores the differences in the

representation of precipitation statistics between the two simulations in comparison with observations. The study uses bias maps, probability distribution and single events based analyses.

Besides a more accurate representation of the orography, the main difference between the two resolutions lies in the model settings, namely the convection scheme. Therefore, the investigation focuses on the representation of the conditions leading to convection at the different resolutions. The instability of the atmosphere, vertical profiles of temperature and humidity as well as cloud cover, radiation budget and triggering mechanisms leading to convection are investigated.

Note that I performed a similar investigation for a larger area covering most of the state of Baden-Württemberg (Fosser et al. 2014).

In the following, Chapter 5.2 describes the simulations used in this study. The methodology applied in each step of the analysis is explained in Chapter 5.3. Chapter 5.4 presents the results for the investigation area, while the conclusions follow in Chapter 5.5.

5.2. Model simulations

In this chapter, two climatological model simulations of 30 years each are compared, CLM7 and CLM2.8 respectively, at 7 km and 2.8 km horizontal resolution. Both simulations use ERA40 reanalysis data as driving data and cover the period 1968-2000, where the first three years are considered as spin-up time and are therefore not included in the analysis. For the 2.8 km simulations, a nesting strategy is applied as explained in Chapter 2.7. The coarser nest at 7 km comprises all of Germany and the near surroundings (165 × 200 grid points) and the finer nest at 2.8 km concentrates on the state

of Baden-Württemberg (140 × 116 grid points) in south-western Germany (Figure 28). The common investigation area is the black frame in Figure 28.

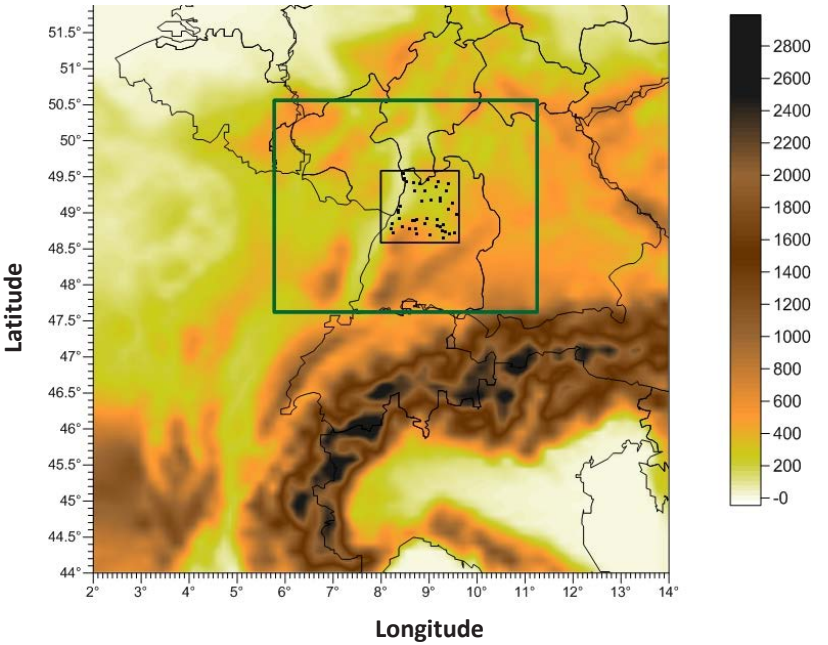

Figure 28: Topographical map of the CLM7 and CLM2.8 simulation domains covering Germany and surrounding areas. The green box represents the simulation domain of CLM2.8 at 2.8 km resolution on the state of Baden-Württemberg in southwestern Germany. The inner black frame indicates the investigation area common to all simulations. The black dots indicate the locations of the precipitation gauges.

The main difference between the two simulations in terms of model settings lies in the convection scheme. CLM7 uses the complete parameterisation of convection according to (Tiedtke 1989), whereas in CLM2.8 the parameterisation of deep convection is turned off. More details on model parameterisation of convection can be found in Chapter 2.5. The 7 km resolution is in a spatial range where one could wonder if and to which extent convective processes can be resolved. Larger convective processes, such as mesoscale con-

vective system, could be resolved partially by the model at 7 km resolution. This would possibly lead to a double counting of precipitation due to an overlap between resolved and parameterised convection. In this context, an additional run, CLM7_conv, was performed to help understanding the effect of the parameterisation on the representation of the atmospheric processes leading to convective precipitation. CLM7_conv is a short simulation (1991-1999 including one year spin-up time) with the same spatial resolution and simulation area as CLM7 (namely 7 km horizontal resolution, Germany simulation area), but with the same convection parameterisation as CLM2.8.

Table 7 provides a summary of the simulations used in this chapter and the main differences among them in terms of model configuration. More information on the general settings of the model can be found in Chapter 2.3.

Table 7: Simulations used in this chapter and their main characteristics.

	CLM7	**CLM7_conv**	**CLM2.8**
Resolution	7 km	7 km	2.8 km
Simulation period	1968-2000	1991-1999	1968-2000
Simulation area	Germany		Baden-Württemberg
Driving data	ER40_reanalysis data		
Convection scheme (Tiedtke 1989)	full parameterisation	only shallow convection parameterisation	
Radiation scheme (Ritter & Geleyn 1992)	1h	1h	15 min
Hydrometeor species (Kessler 1969)	water vapour, cloud droplets, rain, snow, cloud ice		…. and graupel

5.3. Methodology

To determine the potential added value of convective resolving scale versus coarser resolution, two complementary aspects are considered: first, the representation of the precipitation statistics between resolutions, and second, the atmospheric conditions relevant for convection.

Most of the investigation focuses on a sub-daily temporal scale, since convective processes usually occur on a timescale of a few hours. Moreover, coarser temporal scale (e.g. day versus hour) can hide important information, as seen in Chapter 4.5. Any form of averaging (e.g. daily mean precipitation) will be handled with care since this procedure tends to smooth extremes especially when dealing with highly heterogeneous, both in time and space, variables as precipitation. In this context, Prein et al (2013) found that the improvements of higher spatial scale become undetectable when considering monthly or spatial average.

In the first step of the analysis, bias maps and probability distribution plots as well as diurnal cycles are used to assess the differences in the precipitation statistics between CLM7, CLM2.8, the HYRAS dataset and precipitation gauges. More details on the observational dataset are found in Chapter 3 and Figure 28. Berg et al. (2012) found that, in comparison with observations, CLM7 underestimates the probability of dry days due to the presence of too much drizzle and overestimates of low intensities precipitation. Therefore, the study considers also the percentage of dry periods, only wet periods and the duration of the events.

Model outputs and HYRAS have different spatial resolutions. According to Jones (1999), a conservative remapping was performed to bring them on the same scale. This technique minimizes the smoothing effects of remapping

and allows maintaining energy and water budgets. The chosen grid spacing for this study is 2.8 km; however a conservative remapping on 7 km grid would not alter the results significantly (Fosser et al. 2014). For the comparison between model data and observational data, the nearest grid point is selected. This method reduces the sampling bias especially in regions with different landscapes (Moberg and Jones 2004). Fosser et al. (2014) considered the effects of considering an average of five grid points instead of only one. They found that the shape of the probability distribution and diurnal cycle was retained although the mean intensities showed a reduction (as is to be expected when averaging). In the present study, a similar analysis was performed confirming that the results do not change significantly when considering all grid points or only the nearest one (not shown). This is probably due to the flatness of the investigation area at 2.8 km resolution, which guarantees similar precipitation characteristics on climate scale (i.e. 30 years).

In the investigation area, precipitation has different characteristics depending on the seasons. In winter large-scale process are dominant whereas in summer “boundary-layer forced” convection is the main driver for extreme precipitation events (Kottmeier et al. 2008). These meteorological aspects should be reflected in the precipitation characteristics. Thus, the study begins by considering both seasons (DJF and JJA) for the precipitation statistics, and then focuses on summer period only in its second part, which investigates how CLM2.8 and CLM7 represent the atmospheric conditions leading to convective precipitation. In this context, the CLM7_conv simulation becomes important to understand the influence of the parameterisation of convection on the representation of the atmospheric fields related to it.

As seen in Chapter 2.4, an unstable atmosphere enhances of the vertical motion of an air parcel and is thus an important condition to initiate convection. Several indices are used in case studies and NWP to provide an indication of

the atmospheric convective potential. In this context, none of them outperforms the others, and the performances are highly dependent on both the area under investigation and the type of event (Doswell 1987). In climate research as well as in NWP, CAPE and CIN are widely employed as indicators of the state of atmosphere in term of potential for convective processes (Bachner et al. 2008; Brockhaus et al. 2008; Dai and Trenberth 2004; Hohenegger et al. 2009; Langhans et al. 2013; Khodayar et al. 2013; Khodayar et al. 2010). One would expect to have prevailingly a high CAPE and low CIN ahead of the maximum precipitation in the diurnal cycle (Brockhaus et al. 2008). CAPE is highly sensitive to small changes in the temperature and moisture in the boundary layer (Emanuel 1994; Smith 1997). Therefore, these variables are analysed in more detail through both vertical profiles and diurnal cycles. Skew-T plots are also employed to visualise the LCL and the LFC calculated following the parcel theory. The LCL provides an insight into the effects of the different boundary layer conditions between simulations on the level of base cloud formation. LFC allows an estimation of the required strength of the triggering mechanisms for the release of CAPE.

Variables such as temperature and humidity as well as precipitation are highly dependent upon radiation fluxes and cloud cover. Therefore, these variables are also considered. In particular, the analysis considers the fractional cloud cover at both low and middle level (respectively in the range 0-2 km and 2-7 km). The model division of clouds in low, medium and high clouds gives the possibility to evaluate the vertical extent of the clouds, which is an important factor for convection. The depth of cumulus is highly related with the strength of the convection. Moreover, the fractional cloud cover affects the radiative transfer and consequentially other variable such as temperature and humidity. Besides atmospheric instability, a triggering mechanism is favourable for the initialisation of convection. Horizontal wind convergence can lead to a lifting of air mass and thus be a possible cause of forced con-

vection. The higher spatial resolution of CLM2.8 allows a better representation of orography, which should also lead to a better representation of vertical velocity. Spatial distribution and diurnal cycle of this field are also considered in the analysis.

5.4. Results

5.4.1 Precipitation statistics

Figure 29 shows the daily mean precipitation bias between model simulations and the HYRAS dataset for both summer and winter during the period 1971-2000. Generally, CLM2.8 shows a reduced deviation from the gridded observational dataset in comparison with CLM7.

The main improvement is visible in summer when CLM2.8 presents an overestimation within 0 - 30% in most of the investigation domain, while in CLM7 the bias is more spread and reaches up to +70%. In winter, there is a larger wet bias for both simulations up to 110% and 130% for CLM2.8 and CLM7 respectively. The wet bias of CLM7 is a well-known problem of this spatial resolution linked to the overestimation of drizzle, i.e. precipitation below 1 mm/day (Berg et al. 2012).

To interpret correctly the bias maps, it is important to investigate the influence of drizzle not only at 7 km but also at 2.8 km resolution. Therefore, the following analysis considers the percentage of dry days, the probability distribution of precipitation intensities above 1 mm/day and finally the bias maps of the daily mean precipitation calculated considering only wet days (i.e. precipitation above 1 mm/day). Note that for Figure 30, Figure 32 and Table 8 only the closest grid points to the DWD stations were selected for both model simulations and the HYRAS dataset (see Methods).

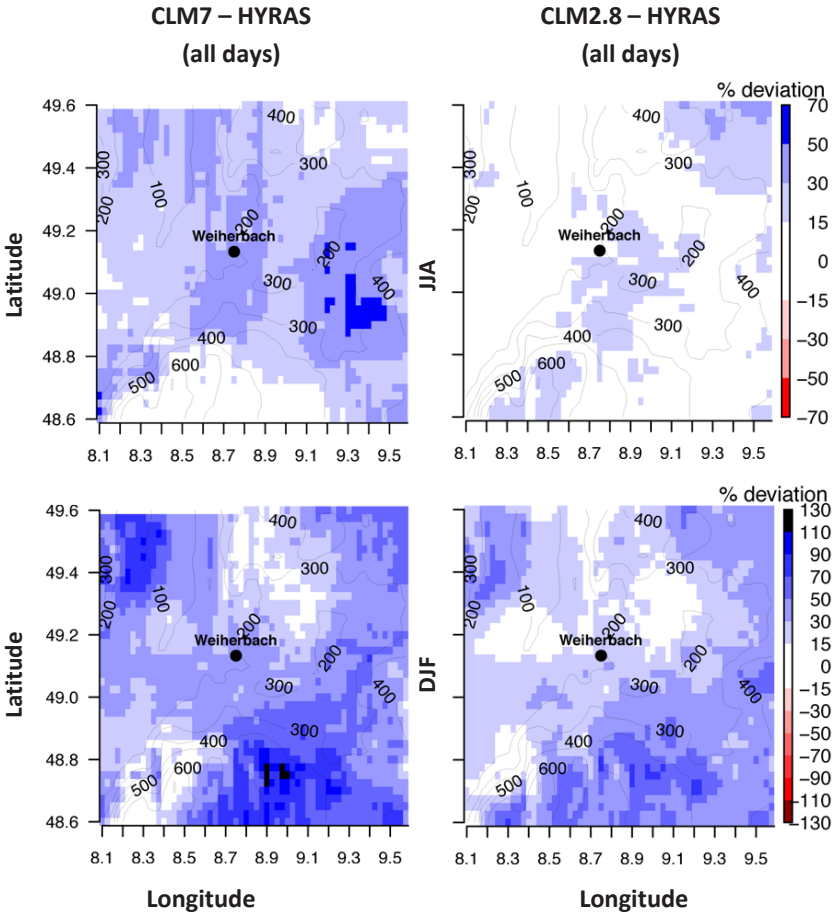

Figure 29: Spatial distribution of the differences (in percent) in daily mean precipitation between model simulations (CLM7 left; CLM2.8, right) and HYRAS dataset in the period 1971-2000, if all days are included. Blue (red) grids show the model overestimation (underestimation). Summer is displayed in the top row, winter at the bottom. The contour lines represent the orography of the area.

Table 8 presents the percentage of dry days for observational datasets and model simulations. The HYRAS dataset is in good agreement with DWD stations in winter but it underestimates the number of dry days in summer by 3%. In comparison with HYRAS data, CLM7 underestimates the number of dry days by 9% and 15% in summer and winter respectively. CLM2.8 reduces the differences with the observations in both seasons and in summer even outperforms the HYRAS dataset.

Table 8: Percentage of dry days (P<1 mm/day) for the DWD stations (DWD_st), HYRAS and model simulations (CLM7 and CLM2.8) in summer (top row) and in winter (bottom row).

Percentage of dry days	DWD_st	HYRAS	CLM7	CLM2.8
JJA	67	64	55	69
DJF	64	64	50	57

The distributions of daily precipitation intensities above 1 mm/day are shown in Figure 30. Generally, the observational datasets agree well with each other, but in winter HYRAS tends to underestimate precipitation above 15 mm/day. In summer, CLM7 performs well for all range of intensities, but it presents more fluctuations in winter. First, it underestimates slightly precipitation below 3 mm/day, and then it overestimates intensities between 3 and 15 mm/day and underestimates precipitation above 15 mm/day. CLM2.8 is very close to observations in winter, except for an underestimation of intensities below 3 mm/day, while in summer it underestimates intensities between 4 and 15 mm/day and highly overestimates precipitation above 15 mm/day.

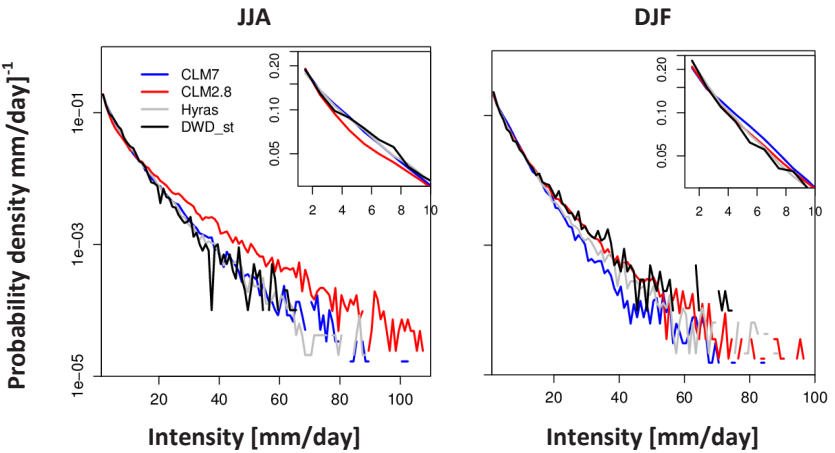

Figure 30: Probability density distribution of daily precipitation for JJA (left) and DJF (right) for only wet days. Note the logarithmic vertical axis.

Since the probability distribution of CLM2.8 (CLM7) in winter (summer) is pretty close to the HYRAS dataset, one would expect also that the daily mean precipitation for CLM2.8 (CLM7) and HYRAS dataset are similar in winter (summer). In this case, the bias in daily mean should be limited; however Figure 29 show that CLM2.8 (CLM7) overestimates the daily mean precipitation of 15 - 90% (up to 70%) compared to HYRAS in winter (summer). Similarly, one would expect that the underestimation of medium intensities (i.e. 4-15 mm/day) of CLM2.8 in summer does not completely compensate the strong overestimation of higher intensities when calculating the daily mean precipitation (i.e. in the bias map of (Figure 29). These mismatches between probability distributions and bias maps depend on the different percentage of dry days between model and HYRAS. In fact, an overestimation (underestimation) of dry days reduces (increases) the daily mean precipitation since more (less) days with a precipitation below 1 mm/day are included in the average.

Bias maps calculated using only wet days allows the daily mean precipitation to not be affected by the bias in dry days and thus better represent the expectation of the probability distribution. For example, in summer CLM2.8 compared to HYRAS highly shows an overestimation of the number of dry days, which compensates the overestimation of the higher precipitation intensities when calculating the daily mean precipitation. This is reflected in a limited bias (i.e. below 30%) in Figure 29 calculated for all days.

When considering only wet days, the overestimation in the probability distribution of CLM2.8 becomes visible with a deviation in daily mean between 30 and 50% (Figure 31), while CLM7 performs very well when drizzle is removed. In winter, when both resolutions highly underestimate the number of dry days (Table 8), considering only wet days reduces the bias in daily mean by 60-100% (comparison Figure 29 and Figure 31). The underestimation of CLM7 of intensities above 15 mm/day is compensated by the higher underestimation of dry days in comparison with CLM2.8.

Up to here, the analysis has considered daily resolution, but increasing spatial resolution should go along with increasing temporal resolution. The comparison between the bias maps of daily mean precipitation calculated first including and then excluding dry days showed how averaging causes a loss of information. Moreover, Haerter et al. (2010) found that the intensity distribution changes character if using an hourly to a daily temporal resolution for the analysis. Thus, the analysis continues using an hourly scale. In this case, the HYRAS dataset cannot be used since it has a daily resolution.

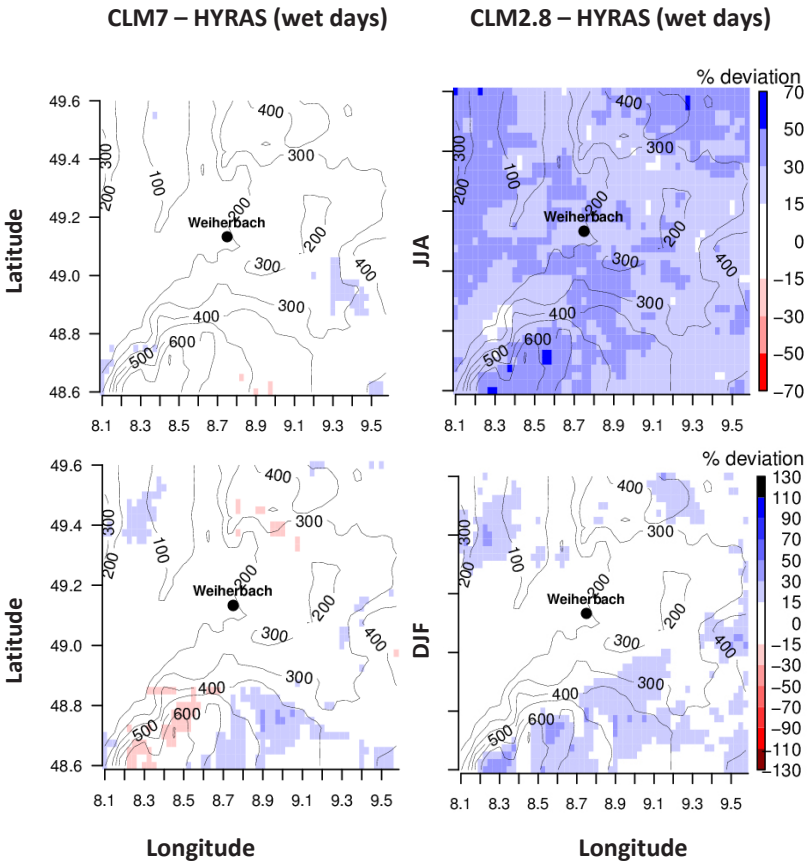

Figure 31: Spatial distribution of the differences (in percent) in daily mean precipitation between model simulations (CLM7 left; CLM2.8, right) and HYRAS dataset in the period 1971-2000, when only wet days (P>1 mm/day) are included. Blue (red) grid points show the model overestimation (underestimation). Top panel represents the summer period (JJA), the bottom DJF. The contour lines represent the orography of the area.

Figure 32 shows the probability distribution of hourly precipitation. In winter, both CLM7 and CLM2.8 are underestimating (overestimating) intensities above (below) 1 mm/h, but CLM2.8 is closer to observations in terms of ex-

treme precipitation events. In summer, CLM2.8 outperforms CLM7, with probabilities close to those observed. In Table 9 the percentage of dry hours (i.e. hours with precipitation below 0.1 mm/hour) shows the same as on a daily basis (Table 8). CLM7 underestimates the dry hours in both seasons (-7% in JJA, -10% in DJF), while CLM2.8 reduces this error.

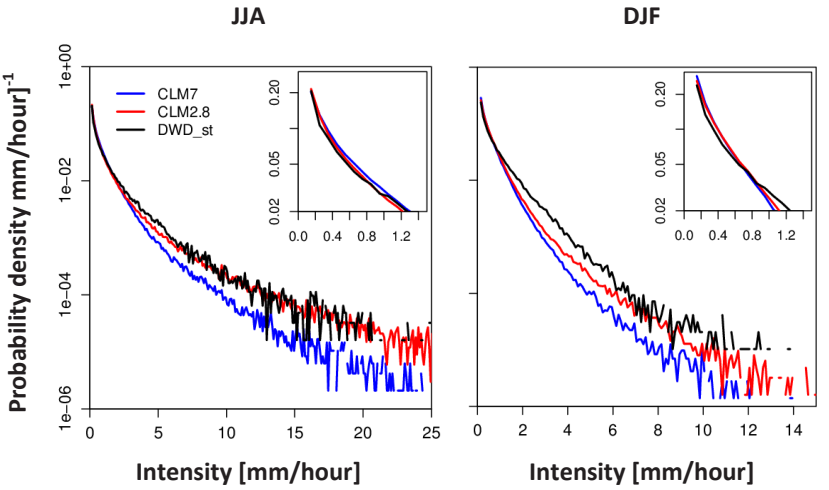

Figure 32: Probability density distribution for hourly temporal resolution for JJA (top) and DJF (bottom). Note the logarithmic vertical axis.

Table 9: Percentage of dry hours (P < 0.1 mm/hour) for the DWD stations (DWD_st) and model simulations (CLM7, and CLM2.8) in summer (top row) and in winter (bottom row).

Percentage of dry hours	DWD_st	CLM7	CLM2.8
JJA	92	85	90
DJF	87	77	80

Comparing the probability distributions from the different temporal resolutions (Figure 30 and Figure 32), it is surprising that, especially in summer, CLM2.8 performs well on the hourly timescale, but poorly on the daily time scale. At the same time, the dry days and dry hour probabilities are very

close to what was obtained for the DWD stations. Meantime, CLM7 presents a good agreement with observations on the daily basis, but is inadequate on the hourly time scale. This mismatch from a statistical point of view can be explained by a simple example as follow. Figure 33 shows two hypothetical days and their hourly distribution of precipitation. The two graphs, top and bottom, have the same sample of hourly data but distributed in a different way over the two days. In the first case, there are five events, in the second, only two events, one of which is quite long. Since the two graphs (top and bottom) have an identical sample of hourly data, they will have identical probability distributions on an hourly base as well as an identical percentage of dry hours. On the daily basis, the probability distribution will be completely different because they have different daily precipitation amounts.

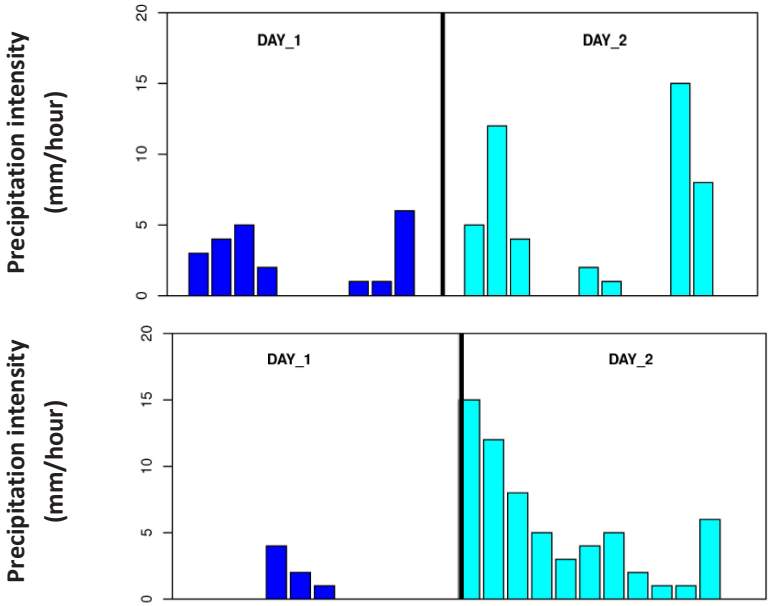

Figure 33: The figure displays two hypothetical days and their precipitation distribution on hourly base. Both graphs have the same sample of hourly data but they are distributed in a different way within the two days.

The hypothesis explaining the mismatch between the probability distribution on different temporal scales is that there is a problem in the temporal structure of wet hours in the model. In reality, usually, there is an “extreme” event and then the precipitation stops. In the model, there is an “extreme” event and then it keeps raining. Thus, in the model the hours are wrongly clustered together on the daily basis.

To prove this, the duration and the amount of the events are calculated for both model simulations and observations in the summer months and displayed in Figure 34. An event starts when the precipitation is above 0.1 mm/hour and it stops when it drops below this threshold. Note that the model time series covers 30 years while the observations only 8 years. To overcome this problem the number of events is normalized by the total number of considered years. This is why the number of events is less than one in some cases for model simulations.

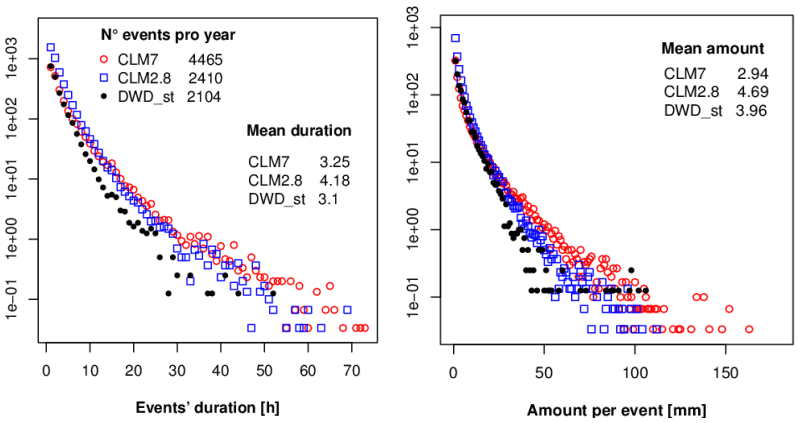

Figure 34: Distribution of the number of events per year in relation to their duration (left) and their amount (right). Note the logarithmic y-axis for all the graphs. The comparison is between CLM7 (blue), CLM2.8 (red) and the observations (black) in JJA based on hourly data. The numbers in the legend indicate the total number of events for each dataset as well as the mean duration and amount for model simulations and observational dataset.

The number of precipitation events per year (Figure 34 left, in the legend) is overestimated by the model especially for CLM7, which presents almost double the observational number of events. This excess of events in CLM7 is likely linked to the drizzle problem (i.e. there are too many wet hours). In fact, CLM7 overestimates the number of events with low duration and low intensities compared with observations (Figure 34). Although the percentage of dry hours is well simulated at 2.8 km resolution, CLM2.8 overestimates the duration of the events longer than 10 hours and on average presents events one hour longer than observations. Thus, the longer events duration is caused by a wrong clustering of the wet hours into the events and thus into days. Longer durations go along with higher amounts, especially for CLM2.8 which reaches a maximum amount of 160 mm/event versus a maximum of 100 mm/event in the observations.

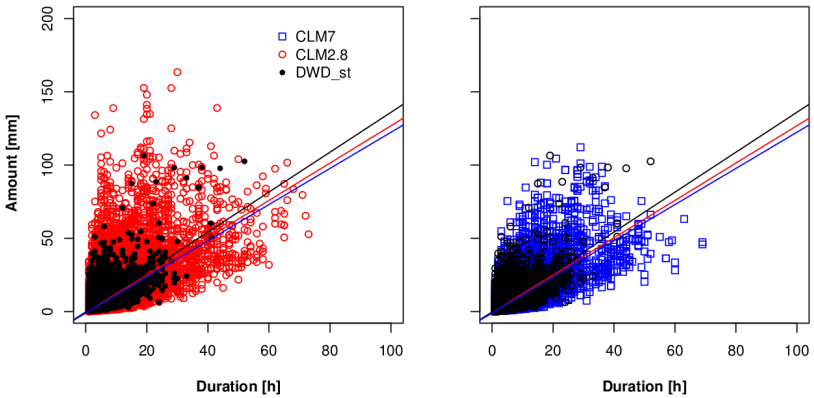

Figure 35: The two panels show the scatter plots of duration versus amount: CLM2.8 and DWD stations on the left; CLM7 and DWD stations on the right. The straight lines represent linear fits to the data, according to the colour. Lines are the same in both graphs.

Figure 35 shows the scatter plots of the precipitation amount for each event as a function of its duration. The straight lines in the plots represent the line-

ar fits to the data, i.e. the amount increases with the events' duration. The observations have a steeper gradient in comparison with model simulations, which means events with the same duration are more intense in reality with respect to what the model forecasts. Reformulating, the model needs longer (i.e. longer event duration) to generate the same amount of precipitation as observed. As a consequence, the events tend to be less intense than observations.

A possible explanation for this behaviour is connected with too much low intensity precipitation in the model. Model simulated events are surrounded by low intensity precipitation above 0.1 mm/h as seen in the example in Figure 33. This will lead to an increase in duration and amount of the event and decrease the mean intensity of the event. On a daily basis, this will lead to an increase in the daily amount (and thus its intensity) because there are less dry hours within the day. This can explain the overestimation on daily temporal resolution of intense events for CLM2.8 in JJA (Figure 30).

5.4.2 Diurnal cycle and atmospheric conditions leading to convection

In this section, we investigate the added value of convection-permitting scale in the representation of convective precipitation and the atmospheric conditions leading to it. Figure 36 shows the precipitation diurnal cycles of station data and model simulation, CLM7 and CLM2.8. In winter (left panel), the observations show higher intensities during daytime with a small peak around 8:00. Both models, and especially CLM2.8, fail in capturing this structure.

In summer, the precipitation diurnal cycle shows clearly the consequence of the parameterisation of convection. In the literature, it is often remarked

how models at coarser resolution have difficulties to correctly represent the summer diurnal pattern of the precipitation cycle (Brockhaus et al. 2008; Dai 2006; Dai and Trenberth 2004; Yang and Slingo 2001). In this season, the observational diurnal cycle presents the same peculiar features (Figure 36, right panel). Particularly important is the maximum between 15:00 and 17:00, which is mainly related to convective activities. The secondary peaks take place around 20:00 and 6:00. CLM7 produces a completely different image of the diurnal cycle with only one large maximum, peaking around 12:00. Because of the parameterisation, it is possible to distinguish the contribution of the grid resolved and the parameterised precipitation (respectively dotted and dot-line in Figure 36). The former agrees well with the morning peak of the observations while the parameterised component is alone responsible for the midday peak.

At 7 km spatial resolution, it is not clear how resolved and parameterised precipitation co-exist and/or influence each other. Thus, a short simulation (i.e. 8 years), called CLM7_conv, was performed with the same spatial resolution as CLM7, but with the same settings of CLM2.8, namely turned-off Tiedtke scheme except for shallow convection (see Chapter 5.2 for details). In CLM7_conv, the precipitation reaches the maximum intensity too late in the evening around 19:00, then maintains quite high values for the whole early morning/night and decreases in intensities after 6:00 (green line in Figure 36). It is therefore clear that CLM7 needs a parameterisation to correctly represent convective processes. On the other hand, the current Tiedtke parameterisation fails in its objective since the convection scheme is triggered too early, inhibiting the grid resolved convection.

The diurnal cycle of CLM2.8 produces a main peak between 15:00 and 17:00 and a smaller one at 19:00. CLM2.8 shows a very good agreement with observations apart from a third peak too early in the morning. Although the ab-

solute values are still overestimated, the shape is more similar between CLM2.8 and station data than for CLM7. The improvements of the convection-permitting scale are particularly relevant in the afternoon, when CLM2.8 correctly simulates the time of maximum convection, which is the main failure of CLM7.

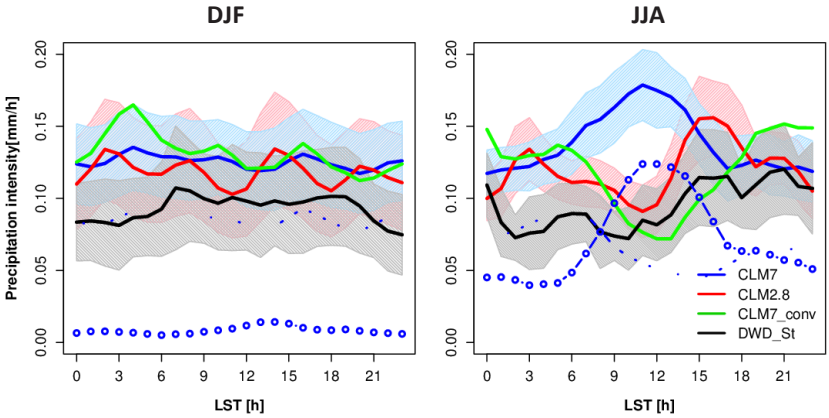

Figure 36: Diurnal cycle of precipitation for CLM2.8 (red), CLM7 (blue), CLM7_conv (green) and observations (black). Results for DJF (left) and JJA (right) are shown. The resolved and parameterised components for the CLM7 simulation are shown as dotted and dashed blue curves respectively. Shaded areas represent the confidence interval calculated as mean precipitation ± standard deviation.

The main interest is now to try to understand the reasons behind this improvement through a deeper analysis of the modelled atmospheric conditions leading to convective precipitation. Therefore, the investigation continues for JJA with the discussion of the instability of the atmosphere, the vertical profiles of temperature and humidity, cloud cover, radiation between different resolutions and finishes with triggering mechanism of convection. In this context, the use of CLM7_conv can help understand the effect of the parameterisation on the results.

In the following, CAPE and CIN are used to assess when the atmosphere is more prone to initiate convection. High values of CAPE indicate a highly unstable atmosphere, a situation that could lead to the development of deep convection and subsequent heavy precipitation. On average, one would expect to have a high CAPE, and low CIN (i.e. low atmospheric opposition to convective processes), before the precipitation maximum in the diurnal cycle (Brockhaus et al. 2008). It has to be noted that the frequency of the model outputs is different for CAPE and precipitation, being every three hours and one hour respectively. The analysis of these two well-known convective indices in connection with precipitation is often applied in climatological studies (e.g. Brockhaus et al. 2008). CAPE is calculated as a mean over 30 years including all weather conditions (i.e. also when convection does not occur). Thus, CAPE values are lower than those usually found in case studies on convection (e.g. Barthlott et al. 2006).

Figure 37 (left) shows that CAPE and CIN evolve similarly for all model simulations throughout the day. From 6:00 CAPE gradually grows until it reaches a maximum between 15:00 and 18:00, depending on the simulation, and decreases afterwards. Similar CAPE evolution and values were also found from Brockhaus et al. (2008), who showed that they compare well with the station of Payerne in Switzerland. CIN shows opposite behaviour in absolute value compared to CAPE. It is high during night, decreases quickly in the early morning, close to zero from 9:00 to 15:00, when it increases again to absolute values up to 300 J/kg.

The comparison between Figure 36 and Figure 37 leads to the conclusion that CLM2.8 well captures the relation between CAPE and precipitation discussed above. In fact, the daily maximum is found between 15:00 and 18:00 for CAPE and around the same time, 15:00-17:00 for the convective precipitation. CLM7 instead simulates the maximum precipitation around 11:00,

but it exhibits the maximum atmospheric instability around 18:00, seven hours too late. Thus, the occurrence of convective precipitation for CLM7 is detached from the atmospheric conditions leading to it, in accordance with previous findings (Baldauf et al. 2011). Conversely, CLM7_conv reaches the maximum instability at 18:00, which is followed by the peak in precipitation around the same time. In this case, the relation between atmospheric instability and occurrence of convective precipitation is maintained. This confirms that it is mainly the parameterisation that is responsible for the too weak connection between atmospheric status and precipitation. On the other hand, CLM7_conv strongly misrepresents the precipitation diurnal cycle in comparison with observations, showing that 7 km spatial resolution needs a parameterisation to correctly represent convective processes acting at smaller scales. Nevertheless, the current version of the Tiedtke scheme needs to be improved in order to be competitive with convection-permitting scale.

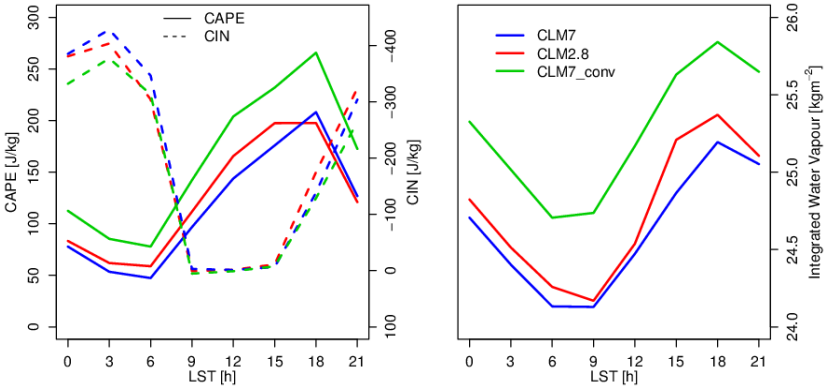

Figure 37: For CLM2.8 (red), CLM7 (blue) and CLM7_conv (green) in JJA the panels show the diurnal cycle of CAPE (solid line) and CIN (dashed line) on the left, and integrated water vapour on the right.

The model calculates CAPE and CIN following the classic parcel theory as seen in Chapter 2.4. Therefore, temperature and moisture of the ascending parcel are crucial elements for the estimation of these indices. The diurnal cycle of these variables and their distribution within the boundary layer can help in understanding the evolution of CAPE and CIN (Brooks et al. 1993; Crook 1996; Khodayar et al. 2010) and thus these variables are investigated in detail. Figure 38 shows the diurnal cycle of specific humidity and temperature at different model levels. Those follow the terrain and, in our case, they represent the pressure levels of ~950 hPa and ~850 hPa. All simulations show similar daily evolution for both variables. Temperature shows the same pattern at both levels, uniformly increasing from sunrise (i.e. 6:00) until 18:00 and decreasing afterwards. By contrast, specific humidity alters its behaviour at different heights in the boundary layer. For both levels, moisture slowly accumulates from 6:00 to 12:00, then it stays constant until 18:00 in the lower boundary layer while it keeps increasing at higher level (~850 hPa).

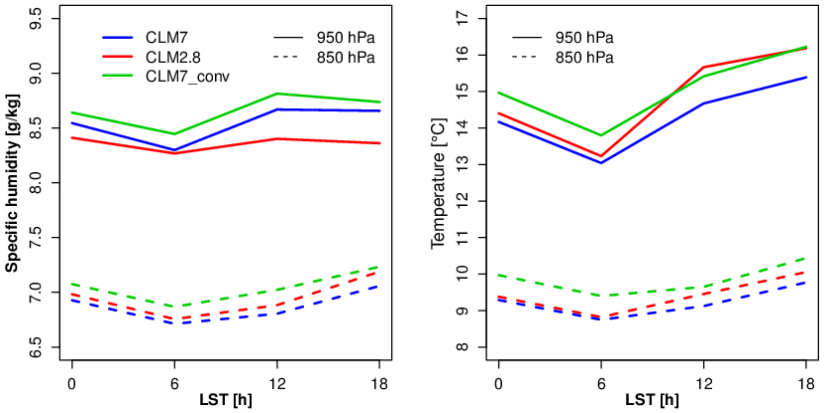

Figure 38: Diurnal cycle of specific humidity (left) and temperature (right) at both ~950 hPa (solid line) and ~850 hPa (dashed line) for CLM2.8 (red), CLM7 (blue) and CLM7_conv (green) in JJA. Note that temperature and specific humidity are output every six hours in all model simulations.

CLM7 and CLM7_conv have similar patterns for both these variables, showing that the parameterisation does not affect their temporal evolution. However, CLM7_conv is systematically wetter and warmer than CLM7 (and CLM2.8) resulting in higher integrated water vapour and CAPE in comparison with the other simulations (Figure 37). The convection-permitting scale (i.e. CLM2.8) shows some differences compared with coarser resolution between 6:00 and 18:00. In particular, at ~950 hPa the temperature increase between 6:00 and 12:00 is substantially steeper than for coarser resolution; this could be related to the reduced cloud cover, as will be explained later in the text and Figure 40a. At ~950 hPa, the maximum differences between the two resolutions in temperature and specific humidity are respectively in the order of 1 °C and approximately 0.3 g/kg, CLM2.8 being drier and warmer. Although this difference in moisture could seem to be negligible, it is of crucial importance for the evolution of the atmospheric conditions. In fact, the atmosphere needs all the layers to compensate this small difference in the lower boundary level since the integrated water vapour shows a CLM2.8 wetter than CLM7 (Figure 37 right).

It is interesting that CAPE has the same diurnal cycle shape as temperature and specific humidity at ~850 hPa. At this level, CLM2.8 is systematically warmer and wetter than CLM7, which results in a higher CAPE. Nevertheless, vertical profiles of temperature and specific humidity can give a better insight on the atmospheric state and explain the temporal evolution of CAPE.
Figure 39 shows the vertical profiles of humidity and temperature both in the midday (12:00, top) and evening (18:00, bottom) periods. The figure confirms what is found in Figure 38, namely a drier and warmer CLM2.8 in comparison with CLM7 in the lower boundary layer, up to 900 hPa. Moreover, the skew-T plots allow the calculation of the level of base cloud formation, LCL; the LFC from where the atmospheric parcels freely rise; and the EL, i.e. the limit of convection (Figure 39 left).

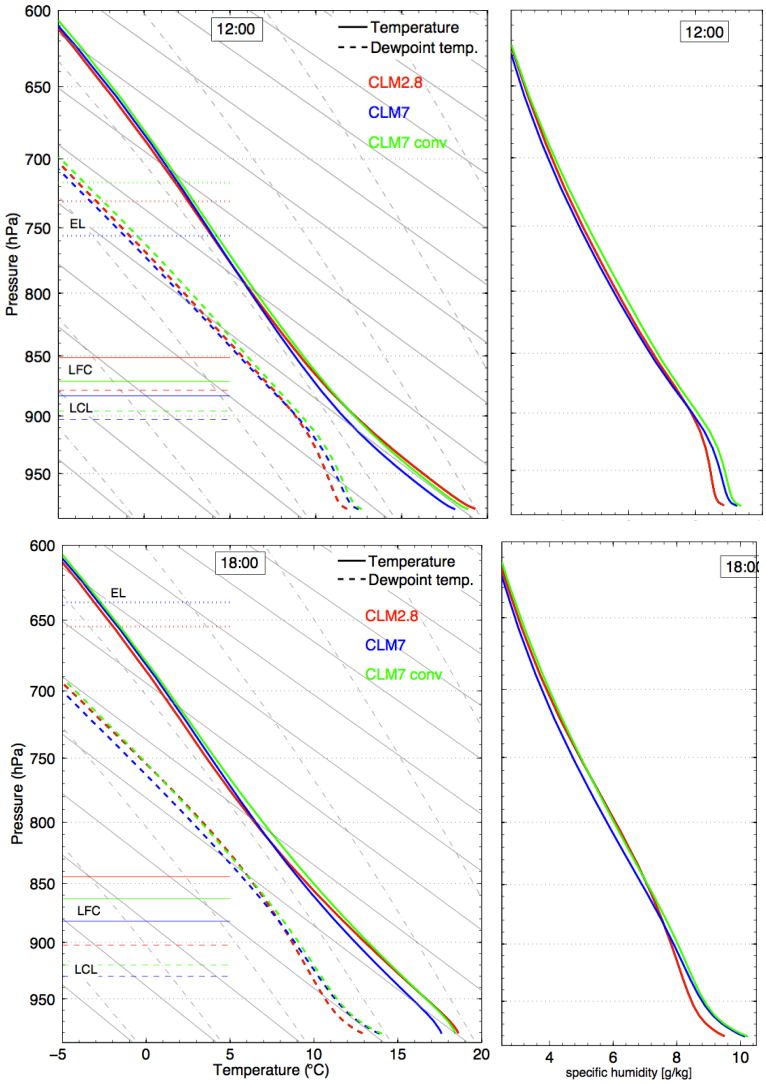

Figure 39: Skew-T plots (left) and vertical profiles of specific humidity (right) respectively at 12:00 (top) and 18:00 (bottom) for CLM2.8 (red), CLM7 (blue) and CLM7_conv (green) in JJA.

In the lower boundary layer, at both 12:00 and 18:00 CLM7 is wetter and cooler in comparison with CLM2.8 leading to lower LCL and LFC. This means that clouds can form more easily and frequently, impeding the increase in temperature and the accumulation of water vapour necessary for the initiation of deep convection. This situation is likely to result in low intensity precipitation instead of heavy thunderstorms as in the case of convection. This scenario would explain the drizzle problem affecting CLM7. Meanwhile, a much less wet environment in CLM2.8 could explain why its specific humidity does not vary remarkably during the day in the lower boundary layer (Figure 38).

Higher LCL and LFC in CLM2.8, in comparison with coarser resolutions, imply that the triggering mechanism will need to be stronger to lift the atmospheric parcels to the LFC and thus initiate convective processes. For all simulations, the temporal variation of the LFC and EL (higher EL at 18:00 than 12:00), agree with the diurnal cycle of CAPE in Figure 37.

The differences found in the analysis of the skew-T plot are reflected in the extent of cloud cover in the atmosphere. CLM classifies clouds depending on their height. Low clouds are from the surface to 800 hPa, medium clouds from 800 to 400 hPa and high clouds from 400 hPa to the free atmosphere. Figure 39 showed that CLM2.8 has systematically higher LCL and LFC with respect to coarser resolution. This causes the reduction in low cloud cover with a maximum difference of circa 10 % at 12:00 (Figure 40a) and consequently the peak in temperature at the same time in the lower boundary layer (Figure 38).

Focusing on medium level clouds (dashed lines in Figure 40a), one immediately notices the peak of CLM2.8 at 15:00. This probably indicates the presence of deeper convective clouds around the same time as the CAPE and

precipitation maxima. Baldauf et al. (2011) found that nocturnal drizzle is due to an excess of boundary layer clouds at night and can generate an overestimation of precipitation. In this context, the decrease in low cloud coverage at night in CLM2.8, in comparison with CLM7, could be one of the reasons behind the attenuation of the drizzle problem at this resolution.

Cloud coverage is often investigated in climate studies given its influence on several atmospheric fields as well as on precipitation. For instance, an overestimation of cloud cover could reduce the heating derived from solar radiation and cause an underestimation of surface temperature, which in turn can result in changes in the atmospheric status and determine the suppression or delay of convective processes (Baldauf et al. 2011; Hohenegger et al. 2008).

A well-known problem of CLM is the underestimation (overestimation) of shortwave (longwave) net radiation, which is due to an overestimation of cloud cover (Jaeger et al. 2008). Note that the longwave radiation has a negative sign and thus to improve its representation, its value should become more negative. Due to improvement in the cloud representation, at convection-permitting scale (CLM2.8) the representation of both radiation net components also improves (Figure 40b). In particular, CLM2.8 shows an increase of shortwave net radiation in comparison to CLM7 as well as a decrease of longwave net radiation. Figure 40c looks in more detail at the short wave radiation, plotting both its components, diffuse and direct. Both of them show an increase, justifying the rise in short wave radiation. Higher direct radiation is probably linked to the diminished cloudiness at 12:00 in CLM2.8 versus CLM7.

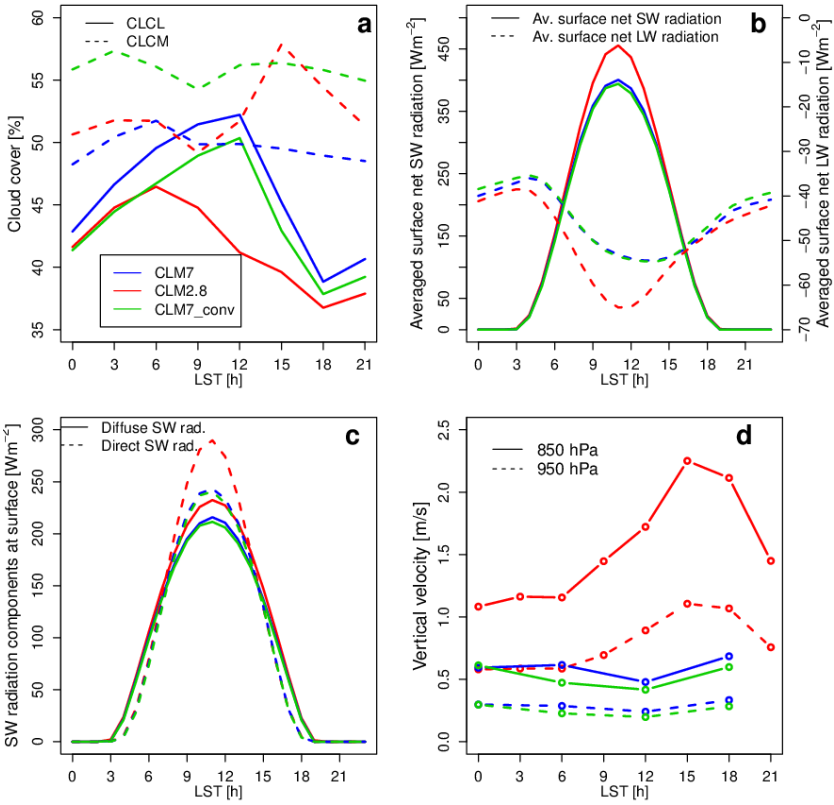

Figure 40: All the panels show the diurnal cycles for CLM2.8 (red), CLM7 (blue) and CLM7_conv (green) in JJA. The variables shown are respectively: panel a, cloud cover at low (solid line) and medium level (dashed line); panel b, averaged surface net shortwave and longwave radiation (solid and dashed line respectively). Note that radiation is positive when directed downward. Panel c represents the surface shortwave radiation components for both diffuse (solid line) and direct (dashed line), while panel d the instantaneous vertical wind maxima at ~850 hPa (solid line) and ~950 hPa (dashed line).

Besides an unstable atmosphere, a triggering mechanism favours the initiation of convection to allow the release of convective potential energy. Analysing the LCL and LFC, it was underlined that CLM2.8 would have needed a stronger triggering mechanism to initiate convection in comparison with

coarser resolution. Figure 40d shows the diurnal cycle of the instantaneous maximum vertical velocity *w*. CLM2.8 exhibits more intense updrafts in comparison with both simulations at coarser resolution, proving that the enhancement of *w* is due to a better representation of the orographic features. Vertical velocity simulated at convection-permitting scale can reach even higher values, up to 14 m/s, in areas with steeper orography, like the Black Forest (Fosser et al 2014). The vertical velocity at CLM2.8 peaks at 15:00, especially at ~850 hPa, consistent with the higher cloud coverage at middle level (Figure 40a) and the maximum in convective precipitation between 15:00 and 17:00 (Figure 36 right).

In addition, the spatial distribution of *w* is considered for different atmospheric levels, namely ~950 hPa, ~850 hPa and ~500 hPa (Figure 41), where CLM7 is displayed on the left and CLM2.8 on the right. The values are much lower than those presented in Figure 40d because of the averaging over 30 years. Nevertheless, substantial differences can be seen, especially at lower levels, ~950 hPa and ~850 hPa (bottom and middle panel). CLM2.8 shows a remarkably larger spatial variability at all levels in comparison with coarser resolution, due to the higher-resolution representation of orography at convection-permitting scale. The representation of convergence and divergence areas, more consistent with the orographic features of the area, is of great importance for the initiation of convection (Kalthoff et al. 2009).

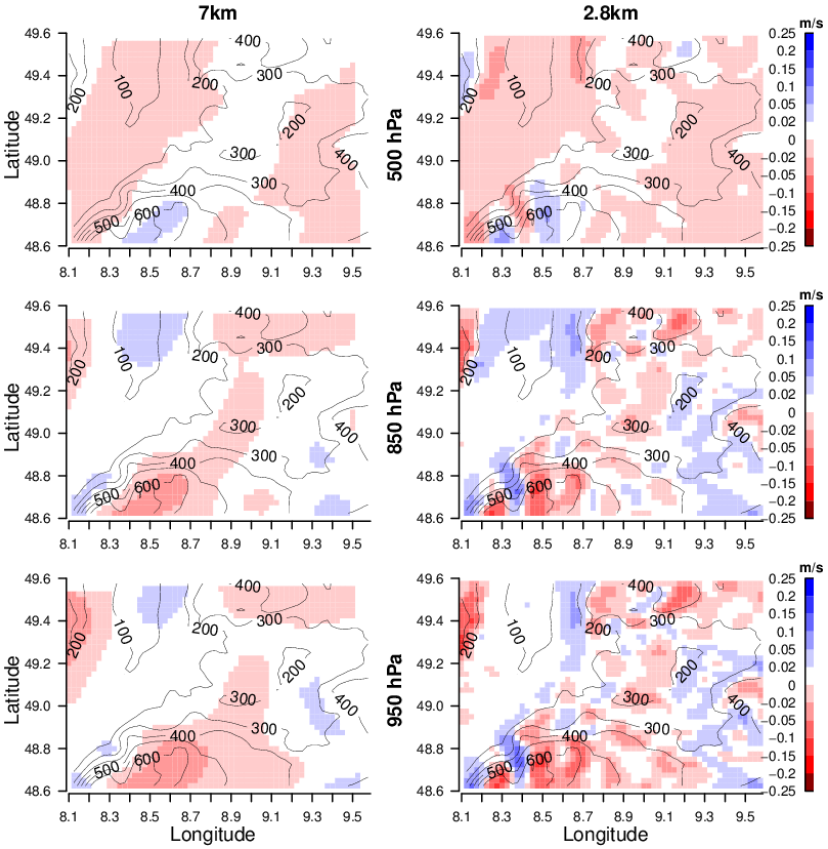

Figure 41: Spatial distribution of vertical wind as a mean over the JJA period 1971-2000 for CLM7 (left) and CLM2.8 (right) at ~500hPa (top), ~850hPa (middle) and ~950hPa (bottom). The contour lines represent the orography of the area.

5.5. Summary and conclusion

This chapter investigated the benefit of convection-permitting scale compared to the coarser resolution in the representation of the precipitation field. In particular, the focus is on the convective precipitation and the atmospheric conditions leading to it. The main difference between the two resolutions considered, besides an improved representation of orography, lies in the possibility to switch off the parameterisation of convection, which is known to be a major source of error and uncertainties (e.g. Brockhaus et al. 2008). Several studies showed the added value of convection-permitting scales in NWP mode or for seasonal simulations (e.g. Hohenegger et al. 2008; Prein et al. 2013), but none was performed on a climate scale. In this context, CLM was used to simulate 30 years at both a 7 km (CLM7) and a 2.8 km (CLM2.8) resolution over the state of Baden-Württemberg in southwestern Germany. The HYRAS dataset as well as 45 measurement stations, operated by DWD, are used to validate the precipitation field versus observations.

CLM2.8 produces a number of dry days close to observations especially in summer and thus reduces the drizzle problem affecting coarser spatial resolution (i.e. CLM7; Berg et al. 2012). In winter, the dominance of large-scale circulation could explain the strong overestimation of wet days that leads to a strong bias in daily mean precipitation at both resolutions. The relatively small size of the simulation domain at 2.8 km could impede the autonomous evolution of CLM2.8 especially in this season. The analysis showed that averaging procedures, as for the bias maps, have to be handled with care, especially in the case of strong overestimation/underestimation of dry days, to avoid arriving at wrong conclusions.

The probability distribution of daily precipitation is well represented by CLM7 for all ranges of intensities especially in summer. By contrast, CLM2.8 highly overestimates precipitation above 15 mm/day in summer, while it is very close to observations in winter. Increasing the temporal scale used for the analysis leads to opposite conclusions. On an hourly basis CLM2.8 performs very well in terms of probability distribution, while CLM7 highly underestimates it in both seasons. This mismatch between different temporal resolutions is due to a wrong clustering of wet hours on the daily basis. The events in CLM2.8 are longer, produce higher amounts of precipitation and have lower intensities than observations. Probably, when the model simulates an event, it surrounds the event with low intensity precipitation above 0.1 mm/h, thus leading to an overestimation of higher intensities on the daily basis. Most probably situation occurs also at CLM7, which underestimates hourly statistics but performs well on a daily basis. Further analysis would be necessary to understand the reasons behind this model behaviour.

In accordance with the literature, CLM7 fails in representing the summer diurnal cycle of precipitation presenting a strong maximum around midday. By contrast, CLM2.8 simulates well the shape of the diurnal cycle in summer although it overestimates the amount and presents a peak in the morning that does not exist in the observations. The improvement at convection-permitting scale seems to be linked to the explicit resolution of deep convection. Temperature and specific humidity have similar diurnal evolution among simulations, with CLM2.8 being wetter. The higher humidity, especially in the afternoon, could be responsible for the more unstable atmosphere in CLM2.8. According to Baldauf et al. (2011), the parameterisation decouples the initiation of convection from the boundary layer conditions leading to it. The analysis of the diurnal cycle of CAPE shows that the atmosphere reaches the maximum instability just before the afternoon peak of precipitation only when the parameterisation of convection is switched off.

However, CLM7_conv misrepresents the precipitation diurnal cycle showing a maximum precipitation too late in the afternoon. Thus, a parameterisation is still necessary at 7 km resolution, but the Tiedtke scheme needs to be improved in order to be competitive with convection-permitting scale.

The analysis of the vertical profiles of temperature and specific humidity show that CLM2.8 tends to be systematically warmer than CLM7, with maximum difference at 12:00 of 1 °C. Moreover, CLM2.8 is slightly drier than CLM7 in the lower boundary layer but it gets wetter at higher levels in the atmosphere. Wetter and cooler CLM7 lead to a steadily lower LCL and LFC compared to CLM2.8. This could foster the formation of clouds at low level and be a cause of drizzle. By contrast, the boundary layer conditions of CLM2.8 allow the accumulation of moisture, which is a driving element for deep convection and eventually heavy precipitation. The temperature peak at 12:00 in CLM2.8 is probably due to a strong reduction at the same time in low cloud compared to CLM7. The latter condition results also in an increase (decrease) in surface net shortwave (longwave) radiation correcting thus its underestimation (overestimation) detected by Jaeger et al. (2008). This improvement depends on the increase of diffuse but mainly direct shortwave radiation. Due to a better representation of orography, vertical velocities show a more consistent alternation of convergence and divergence areas and much higher values in the diurnal cycle for CLM2.8 compared to CLM7. Moreover, wind convergence, which can trigger the initiation of convection, presents its daily maximum at 15:00, in good agreement with convective precipitation, CAPE and mid-level cloud cover.

Concluding, CLM2.8 provides a representation of the diurnal cycle of summer precipitation in good agreement with observations, thus overcoming the well-known limitations of coarser resolution. Moreover, CLM2.8 shows a more consistent representation of the atmospheric conditions leading to

deep convection compared to CLM7. The ability of convection-permitting scale of correctly simulating precipitation on an hourly basis is of crucial importance for erosion models, which are more sensitive to heavy precipitation than to long durations (Antonetti 2013). The 7 km resolution presents insufficiently strong events to generate erosion, while 2.8 km allows reaching a better agreement with observational data from field campaigns, at least for the Weiherbach area (personal communication with Mrs Kempf from GEOMER GmbH). Moreover, the possibility to have a correct simulation of the diurnal cycle for the right reasons allows for a more sound analysis of the changes in precipitation extremes in the near future.

6. Analysis of climate change signal in higher versus coarser spatial resolution

6.1. Introduction

In its Fifth Assessment Report (AR5), the Intergovernmental Panel on Climate Change forecast for the 21st century a global warming of about 0.2 K per decade, with even larger increases for sub-regions, such as Europe (IPCC 2013). The trends for precipitation show a high seasonality and the signal is stronger in winter and summer compared to intermediate seasons (Feldmann et al. 2012; Giorgi et al. 2004; Wagner et al. 2012). The AR5 GCMs ensemble predicts a precipitation increase in winter in Northern Europe and a decrease in Southern Europe for summer. However, large uncertainties on the future climate remain for Central Europe where the models disagree on both distribution and magnitude of the climate change signals (IPCC 2013).

Knowledge of the regional trends of the precipitation and temperature patterns under climate change is crucial to develop effective adaptation measures not only to deal with soil erosion, but also in others fields such as hydrology, agriculture, and urban drainage network planning. RCMs help in bridging the gap between GCMs and regional planning requirements and they can give a better insight in the future climate in Europe. Moreover, increasing horizontal resolution enables a more detailed representation of topographical features and may lead to better results in simulating extreme precipitation events (Giorgi 2006), spatial patterns and intensity distributions of precipitation (Boberg et al. 2010). Several projects pursued the goal of investigating the climate change signal in Europe using RCMs through steadily increasing the spatial resolution, as, for example, PRUDENCE (Christensen and Christensen 2007) and ENSEMBLES (Hewitt 2005) with a resolutions of 50 km and 25 km respectively. An even higher resolution, namely 7 km, was

reached by Feldmann et al. (2012) and Wagner et al. (2012) using the CLM and WRF models over southwestern Germany. Besides the different spatial resolutions, a clearer climate change signal was found, especially for temperature, that shows a wide-spread increase over the whole of Europe for all seasons but with the largest warming in summer in the Mediterranean region (Christensen and Christensen 2007). Wagner et al. (2012) found that annual temperature in Germany will rise on average by 1.1 K. While the future temperature change seems to depend mainly on the GCM and its realization, RCMs play a significant role in the projected precipitation especially in summer (Déqué et al. 2007; Wagner et al. 2012).

For this season, Giorgi et al. (2004) found that the future Atlantic storms track tends to be deflected northward causing a precipitation decrease over most of Europe. Over southwestern Germany, Feldmann et al. (2012) forecast no significant changes in mean precipitation apart from a slight decrease on the lower mountain ranges. However, looking at the probability distribution of precipitation, simulations agree on a future increase in the more intense events and a decrease in light and moderate precipitation (Boberg et al. 2010; Boberg et al. 2009; Feldmann et al. 2012; Wagner et al. 2012). Feldmann et al. (2012) hypothesized that the changes in extreme precipitation are connected to changes in the soil moisture, surface energy balance and atmospheric stability. In this context, Giorgi et al. (2004) found a uniform reduction in cloudiness, snow cover and soil water content over Europe but an increase of 10 - 20% in atmospheric moisture. Moreover, in the near future the number of dry days and dry periods of more than five consecutive days are projected to rise by + 20% on the annual scale in southwestern Germany (Wagner et al. 2012) in line with the European trend (Giorgi et al. 2004). In winter, mean precipitation shows widespread increase of 5–10% over southwestern Germany, in line with the European trend (van der Linden and Mitchell 2009). This rise seems to be due to an increase in the number

of events or their duration more than to their intensity. According to Giorgi et al. (2004), this change depends on the increase in cyclonic activity and higher atmospheric water vapour content in a warmer climate (Trenberth et al. 2003).

Giorgi et al. (2004) underlined the importance of the model selection in predicting climate changes in summer when the parameterisation of local processes, like convection, can impact strongly on the results. Climate convection-permitting simulations improve the probability density distribution of hourly precipitation and the representation of more extreme precipitation events (Fosser et al. 2014; Prein et al. 2013). The shape of the precipitation diurnal cycle in summer is closer to the observations thanks to a more consistent representation of the atmospheric fields related to convection (Fosser et al. 2014). However, not much is known about the added value of this spatial resolution in the context of the climate change because of the high computational costs of this type of simulation.

The purpose of this chapter is to determine if at convection-permitting scale a climate change signal is detectable and in line with previous findings at coarser scale. Moreover, it is important to understand if it is worthwhile investing in higher spatial resolution. This spatial scale could allow us to gain more information on the precipitation changes and the reasons behind them, especially in summer, when the uncertainties related with the parameterisation of convection are higher. For this reasons, ECHAM5 is used to force two climatological model simulations of 30 years in the recent past (1971-2000) and the near future (2012-2050), at 7 km and 2.8 km resolution. The comparison between the two resolutions focuses on winter and summer when the climate change signal is stronger (Feldmann et al. 2012; Giorgi et al. 2004; Wagner et al. 2012) and the added value of convection-permitting scale becomes evident (Fosser et al. 2014).

Chapter 6.2 describes the methodology used in the following. The results on the climate change signal are presented in Chapter 6.4 after the validation of the ECHAM5 driven simulations in the recent past against those forced with ERA40 reanalysis data (Chapter 6.3). Conclusions and implications for erosion can be found in Chapter 6.5.

6.2. Methodology

For the studies described in previous chapters, ERA40 reanalysis data were used as driving data. The choice was justified by the necessity to have model data as close as possible to observations in order to determine the optimum simulation area and model configuration (Chapter 4) and the added value of convection-permitting scale versus coarser resolution (Chapter 5).

To investigate the climate change signal, GCMs output can be used as forcing. More details on the different forcing characteristics are given in Chapter 2.6. The GCM ECHAM was developed by the Max Planck Institute for Meteorology and it is one of the contributing models for AR4. Its fifth version, ECHAM5 (Roeckner et al. 2003), is widely used for studies on the climate change signal (e.g. Feldmann et al. 2012; Reichler and Kim 2008; Wagner et al. 2012). This type of model gives the possibility to investigate both past and future periods. It has to be noted that one cannot expect a time correspondence between ECHAM5 and observed events since GCMs can only be expected to describe the statistics of the climate variables (Feldmann et al. 2008). Moreover, changing the forcing (ECHAM5 versus ERA40) affects the model performances and can add an additional bias (Berg et al. 2012). Thus, modellers usually investigate the error introduced by different forcings and then analyse the climate change signal (e.g. Berg et al. 2012; Wagner et al. 2012).

This chapter follows the same strategy as summarised in Table 10. First, in Chapter 6.3, the model driven with ECHAM5 is compared with ERA40 driven simulations. The latter are used as reference and thus the graphs in the following do not use observational data. The main differences between ERA40 driven simulations and observational dataset (i.e. HYRAS dataset and DWD station) were already discussed in Chapter 5 and in the following they are underlined only when necessary. The nearest grid points to the DWD stations are selected to be consistent with the previous chapter. For this first step of the analysis, the simulations cover the period 1968-2000, where the first three years are considered as spin-up time and therefore not included in the analysis. The variables considered for the model validation are precipitation and temperature, the same used for the validation of 7 km resolution versus the previous nest at 50 km by Berg et al. (2012). Note that EC7_past and EC2.8_past (see Table 10) are abbreviated to EC7 and EC2.8 in the validation chapter for simplicity.

Table 10: Summary of the simulations used in the Chapter 6.3 and 0.

	Simulation	Resolution	Driving data	Analysed simulation period	
Validation (Chapter 6.3)	ER7	7 km	ERA40 re-analysis data	1971-2000	
	ER2.8	2.8 km			
	EC7_past	7 km	ECHAM5	1971-2000	
	EC2.8_past	2.8 km			
	EC7_fut	7 km	ECHAM5	2021-2050	Climate change signal (Chapter 6.4)
	EC2.8_fut	2.8 km			

The second step, in Chapter 6.4, investigates the climate change signal comparing ECHAM5 driven simulations in the past, when only twentieth century anthropogenic forcing is considered (Roeckner et al. 2006), with the future, which uses the IPCC SRES A1B forcing scenario (Nakicenovic et al. 2000). The recent past covers the same period as for validation. Only limited differences in the order of ± 10–20 % were found among ECHAM5 realisations of the past in reference to the spatial distribution of annual precipitation (Berg et al. 2012). In terms of probability distribution Berg et al. (2012) did not find any relevant difference among realisations apart from slightly higher probabilities for the most extreme precipitation events in R1 realisation. Since this study focuses on the extremes, R1 realisation is selected for further downscaling to 2.8 km resolution.

The simulations for the near future extend from 2018 to 2050 with a spin-up time of three years. To investigate future changes in soil erosion, the KLIWA group chose this time period because of its compatibility with their planning horizons. The projected climate change signal is smaller for the selected period than for 2070-2100 (Wagner et al. 2012), which is commonly used to investigate changes in future climate (Boberg et al. 2009; Christensen et al. 2007; Christensen and Christensen 2007; Déqué et al. 2007; Déqué et al. 2005; Giorgi et al. 2004). In this part of the analysis, the comparison between past and future ECHAM5 simulations is not limited to temperature and precipitation as for the model validation. Several other atmospheric variables, such as humidity, CAPE, cloud cover and radiation, are considered in order to understand the possible reasons behind changes in the precipitation pattern. All grid points within the investigation area are used in the analysis since there is no comparison with observations.

There is abundant literature discussing the climate change signal at coarser resolution, while little is known on the effects of higher spatial resolution in

this context. Thus, more space will be given to convection-permitting scale to determine if it can provide more detailed or different information about future changes in the precipitation pattern with respect to coarser resolution. Information on the nesting strategy applied to reach convection-permitting scale can be found in Chapter 2.7. The investigation area is the same for both resolutions and throughout the chapter (black frame in Figure 28 in Chapter 5). The model internal settings are kept unchanged for both validation and investigation of the climate change signal (summarised in Table 7 in Chapter 5).

The whole study focuses on winter and summer since the climate change signal in these seasons is more pronounced than in spring and autumn (Giorgi et al. 2004). Previous chapters underlined the crucial role of using a sub-daily as well as an event-temporal scale in the evaluation of convection-permitting scale. Thus, the same strategy is employed also in this chapter. Bias maps and probability distribution plots as well as diurnal cycles are used to assess the error introduced by the change in the forcing as well as the differences between past and future in the precipitation pattern and related fields.

Note that in the study of the climate change signal, it is assumed that the model maintains the same error in the past and future. This assumption is likely to be acceptable for the very near future (2021-2050) when the climate change signal is weaker. Under this hypothesis, the model bias due to the change in the forcing does not affect the findings regarding the climate change signal, i.e. the relative change in the precipitation pattern between past and future would be correct even if the absolute values are overestimated or underestimated in comparison with observational datasets. Thus, the absolute values provided in Chapter 6.4 should always be seen in the context of a comparison between past and future.

6.3. Validation: ERA40 versus ECHAM5

The validation compares ECHAM5 with ERA40 driven simulations to evaluate the error introduced by a different forcing. Most of the graphs do not show observational data, which were already presented in Chapter 5. Note that an "underestimation/overestimation" compared to ERA40driven simulations does not necessarily imply an underestimation/overestimation versus observations.

Figure 42 compares the probability distribution of ECHAM5 and ERA40 driven simulation at both spatial resolutions on daily basis. In summer (left panel), EC2.8 compared to ER2.8 underestimates intensities below 4 mm/day, overestimates them between 4 and 20 mm/day and underestimates them again for intensities above 50 mm/day. Remembering Figure 30 in Chapter 5, one can conclude that EC2.8, compared to observations, presents a strong underestimation of low intensities (below 4 mm/day) and an improvement in higher intensities above 50 mm/day. Meanwhile, EC2.8 keeps overestimating intermediate intensities between 15 and 50 mm/day like ER2.8. By contrast, the 7 km resolution simulations seem to be much less sensitive to the change of the forcing being EC7 and ER7 close to each other. The same situation occurs in winter for both resolutions, meaning that different driving data do not change substantially the shape of the curves and thus EC2.8 is similar to observations, while EC7 underestimates intensities above 15 mm/day (Figure 30 in Chapter 5).

For both resolutions, the ECHAM5 driven simulations lead to a decrease in the percentage of dry days especially in winter (-11% compared to ERA40 driven simulations), consistent with previous findings by Berg et al. (2012) and Feldmann et al. (2008). In comparison with observations, this means in summer for EC7 an increase in the bias (-14% compared to HYRAS) and for

EC2.8 change in the sign of the bias (before +5% versus HYRAS), which leads to an underestimation of dry days equal to -3% (Table 11 and Table 8 in Chapter 5). In winter, EC7 and EC2.8 underestimate dry days by respectively -25% and -18% compared to HYRAS. These overestimations of wet days appear clearly when considering the spatial distribution of daily mean precipitation (Figure 43 and Figure 44).

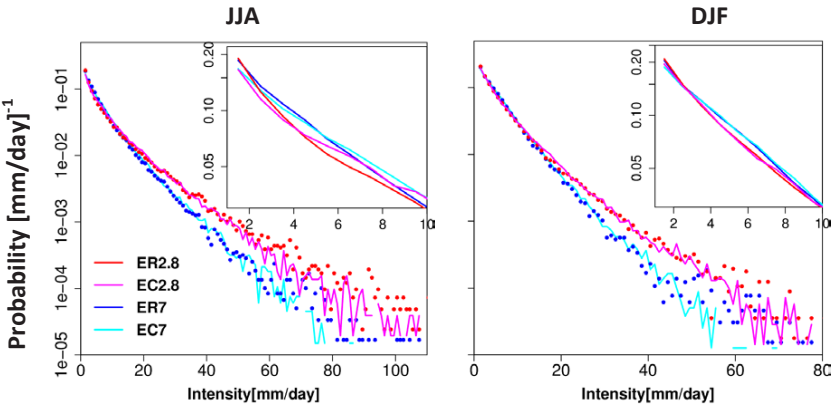

Figure 42: Probability density distribution of daily data for the simulations ER2.8 (red dots), EC2.8 (pink line), ER7 (blue dots) and EC7 (light blue line). Panel on the left refers to JJA and on the right to DJF for the validation period 1971-2000. Note the logarithmic vertical axis.

Table 11: Percentage of dry days (P < 1 mm/day) for ER2.8, EC2.8, ER7 and EC7 in summer (top row) and in winter (bottom row).

Percentage of dry days	ER2.8	EC2.8	ER7	EC7
JJA	69	61	55	50
DJF	57	46	50	39

When considering all days (Figure 43), ECHAM5 driven simulations in both seasons and resolutions show a large bias compared to ERA40 driven simulations, which in turn presented a strong overestimation compared to HYRAS except for ER2.8 in JJA (Figure 30 in Chapter 5).

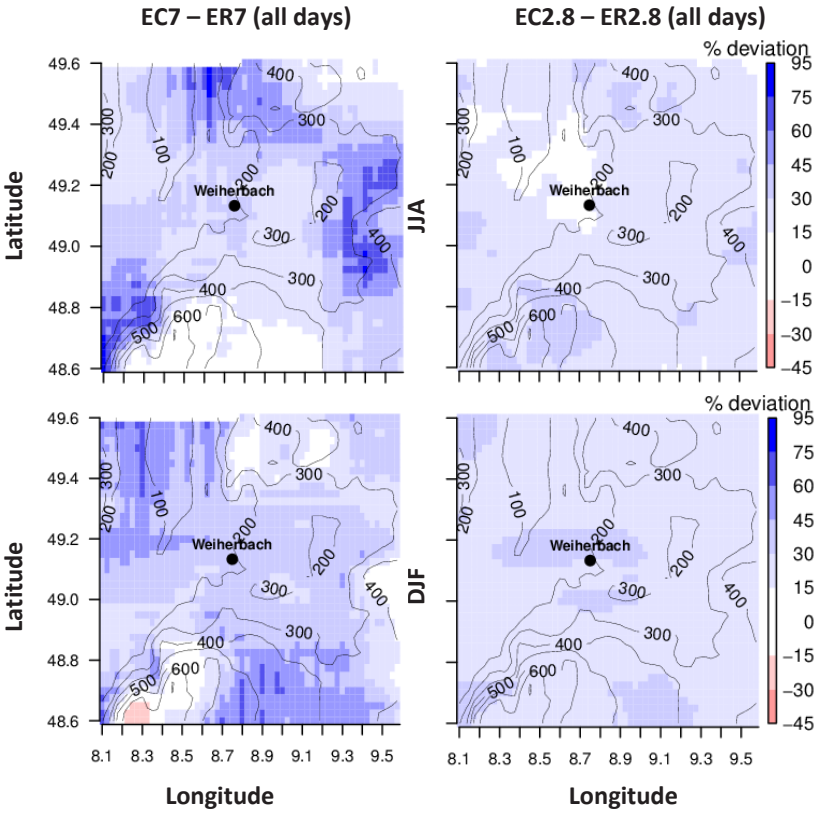

Figure 43: Spatial distribution of the differences (in percent) in daily mean precipitation between ECHAM5 and ERA40 driven simulations in JJA (top) and DJF (bottom) between 1971-2000 for 7 km (left) and 2.8 km resolution (right), when all days are included. Blue (red) grids show an increase (decrease) in mean precipitation in ECHAM5 driven simulation compared to ERA40 reanalysis data. The contour lines represent the orography.

In Figure 44 the wet biases disappear when removing drizzle (P<1 mm/d) proving that the bias is related to the overestimation of wet days. When considering only wet days, ERA40 driven simulations performed well compared to HYRAS except for ER2.8 in summer (Figure 29).

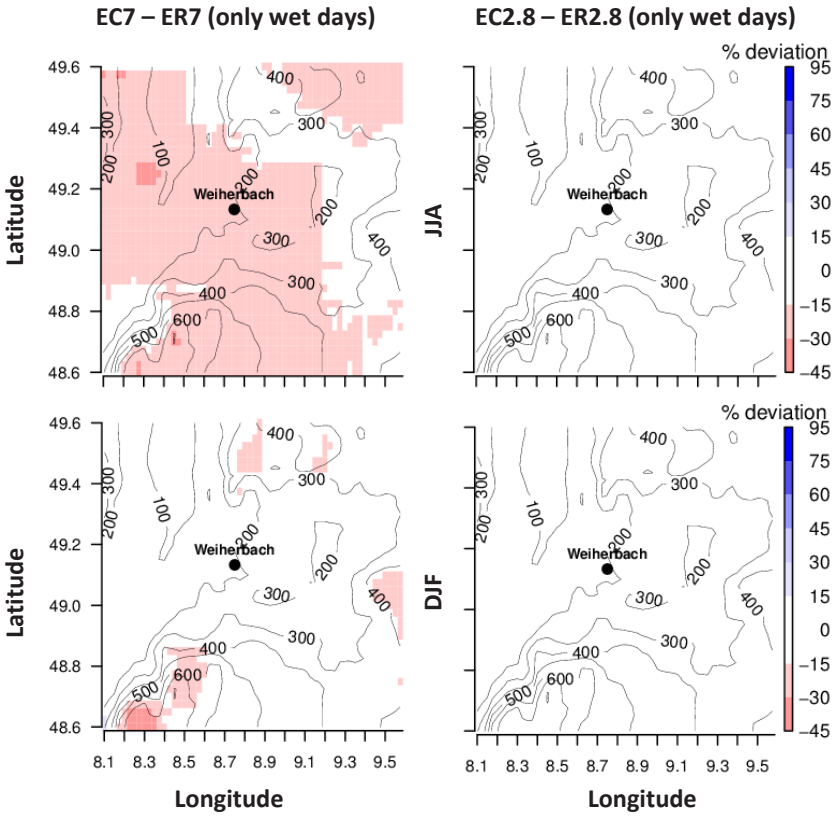

Figure 44: Spatial distribution of the differences (in percent) in daily mean precipitation between ECHAM5 and ERA40 driven simulations in JJA (top) and DJF (bottom) between 1971-2000 for 7 km (left) and 2.8 km resolution (right), when only wet days are included. Blue (red) grids show an increase (decrease) in mean precipitation in ECHAM5 driven simulation compared to ERA40 reanalysis data. The contour lines represent the orography.

On an hourly base, probability distribution of EC2.8 and ER2.8 almost overlap until 7 mm/h and 4 mm/hour respectively in summer and winter (Figure 45). Then, EC2.8 underestimates higher intensities compared to ER2.8 and thus compared to observations (Figure 32 in Chapter 5). A similar statement can be made for EC7 and ER7, but the differences are minor. As for the daily data (Table 11), ECHAM5 driven simulations present a reduced number of dry hours, which was already underestimated in ERA40 simulations especially in winter (Table 12 and Table 9 in Chapter 5).

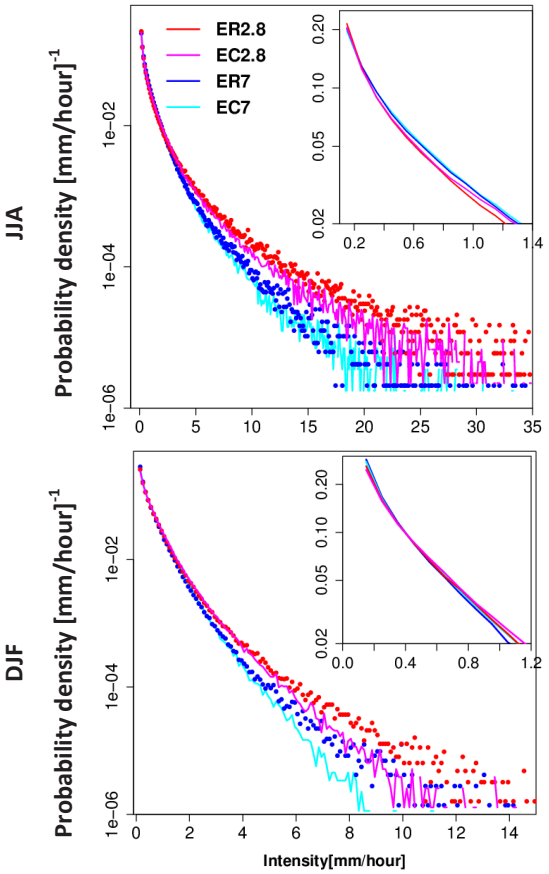

Figure 45: Probability density distribution of hourly data for the simulations ER2.8 (red dots), EC2.8 (pink line), ER7 (blue dots) and EC7 (light blue line). Top (bottom) panel refers to JJA (DJF) for the validation period 1971-2000. Note the logarithmic vertical axis.

Table 12: Percentage of dry hours (P <0. 1 mm/hour) for ER2.8, EC2.8, ER7 and EC7 in summer (top row) and in winter (bottom row).

Percentage of dry hours	ER2.8	EC2.8	ER7	EC7
JJA	89	86	85	82
DJF	57	47	50	39

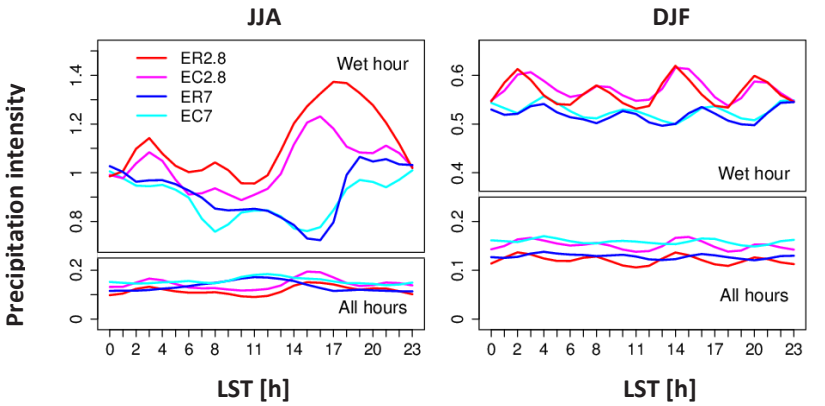

Figure 46: Diurnal cycle of precipitation for EC2.8 (pink), ER2.8 (red), EC7 (light blue), ER7 (blue) calculated considering all hours (bottom) and only wet hours (top). Results for JJA (left) and DJF (right) are shown.

These characteristics explain the different behaviour of the precipitation diurnal cycle whether or not dry hours are included in the calculation (Figure 46). In the first case, the diurnal cycle of precipitation has the same shape for ECHAM5 and ERA40 driven simulations, but the former has higher mean precipitation for both seasons and resolutions. In winter this overestimation vanishes if the dry hours are removed and the shape of the curves remains unchanged. Thus, the main effect of the change in the driving (ECHAM5 versus ERA40) lies in the overestimation of wet hours. Also in summer EC2.8 has higher (lower) mean values compared to ER2.8 when considering all (only

wet) hours. However, the differences between the two cases (all/wet hours) are much stronger than in winter. This leads to the conclusion that the higher precipitation intensities of ER2.8 account considerably in the calculation of the mean.

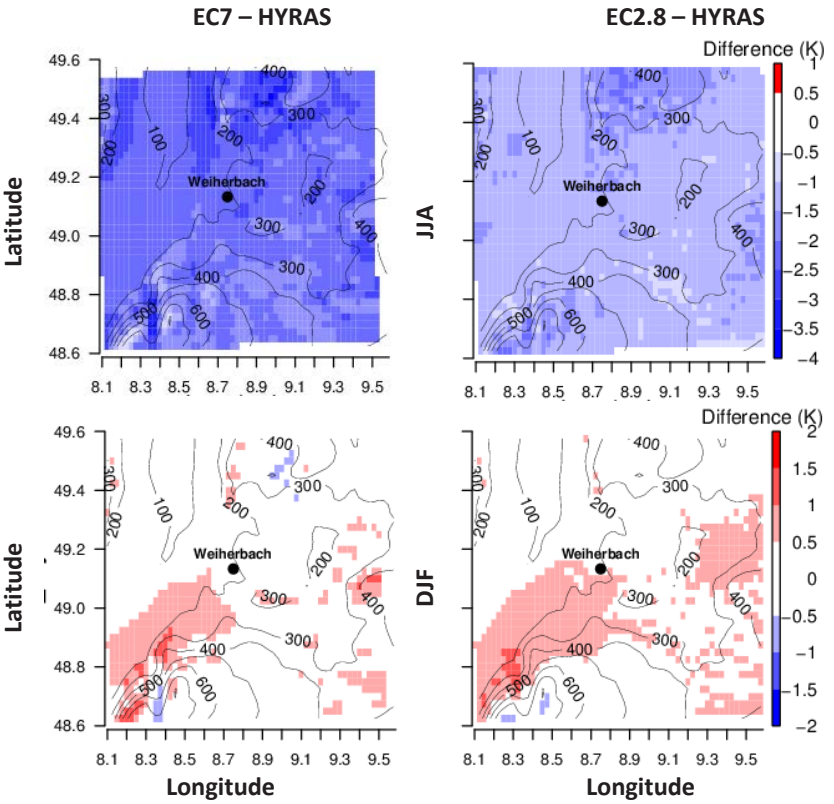

Figure 47: Spatial distribution of the differences in daily mean temperature at 2 m between ECHAM5 and HYRAS in JJA (top) and DJF (bottom) between 1971-2000 for 7 km (left) and 2.8 km resolution (right). Blue (red) grids show a cold (warm) bias in ECHAM5 driven simulation compared to the observational dataset. The contour lines represent the orography of the area.

In climate change studies, the most frequently considered variable beside precipitation is temperature. Thus, this variable is also considered in the validation process. Since Chapter 5 did not consider the bias maps of temperature, the comparison in Figure 47 is performed directly between ECHAM5 driven simulations and the HYRAS dataset for daily mean temperature. More details on the HYRAS dataset can be found in Chapter 3.1. In accordance with the findings from Berg et al. (2012), Figure 47 shows a cold bias between -2 and -3 K for EC7 in summer, while in winter the bias is limited to -0.5 K and 1 K. Comparing ERA40 with ECHAM5 driven simulations at different resolutions (namely 50 and 7 km), Berg et al. (2012) found that the ECHAM5 model introduces an additional cold bias compared to ERA40 driven simulations especially during summer, but the downscaling with CLM from 50 km to 7 km does not increase the original error. In this context, it is interesting to note that EC2.8 reduces the temperature bias in summer by 1.5 K. By contrast, in winter the performance of EC2.8 is comparable with coarser resolution. Thus, the possibility to switch off the convective parameterization leads to a better representation of daily mean temperature, probably due to the reduction at convection-permitting scale of the overestimation in cloud cover affecting coarser resolution (Fosser et al. 2014; Will and Woldt 2009).

6.4. Climate change signal in coarser and higher resolution

6.4.1 Climate change in winter

In winter, the spatial maps of daily mean precipitation show no strong differences between recent past and near future when all days are included in the analysis (Figure 48 top). The situation becomes slightly more interesting when considering only wet days. In fact, Figure 48 at the bottom, shows more extended areas with precipitation between 6 and 8 mm/day and an increase of ~2mm/day over the hills above 600m. In general, the precipitation

maintains its spatial pattern in all cases, i.e. plain areas are drier in comparison with the foothills where the precipitation concentrates. Note that Figure 48 refers to 2.8 km resolution, but similar results are also found for 7 km resolution. The main difference between the two resolutions in the bias maps is found over the hilly area above 600 m, where coarser resolution shows lower daily mean values.

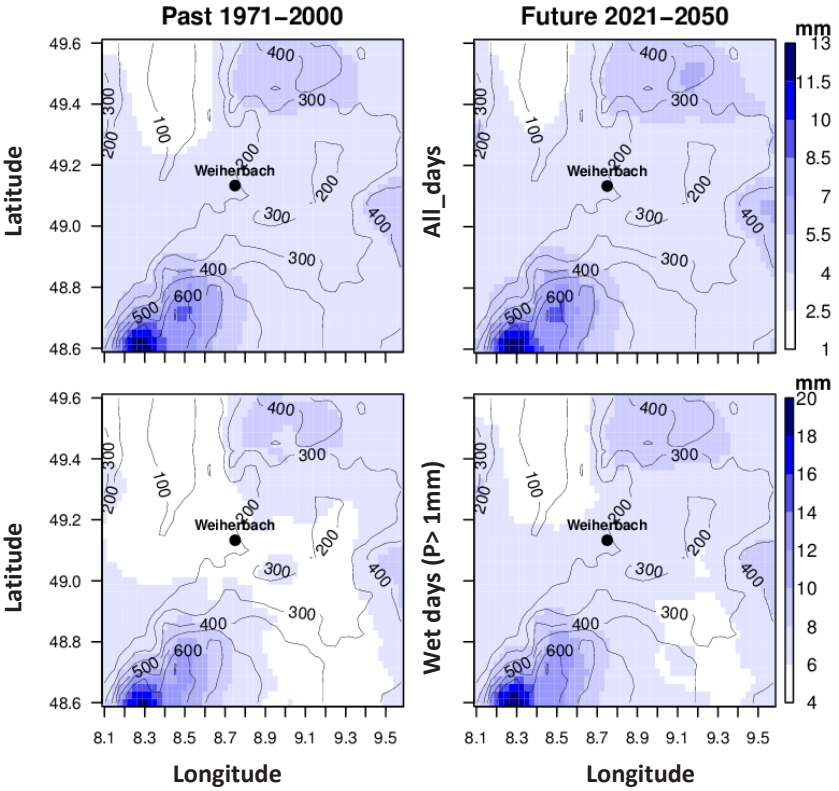

Figure 48: Spatial distribution of daily mean precipitation in winter for the recent past 1971-2000 (left) and near future 2021-2050 (right) at 2.8 km resolution. Top panels consider all days while the bottom ones only rainy days (precipitation above 1 mm/day). The contour lines represent the orography of the area. Note the different scale between top and bottom row.

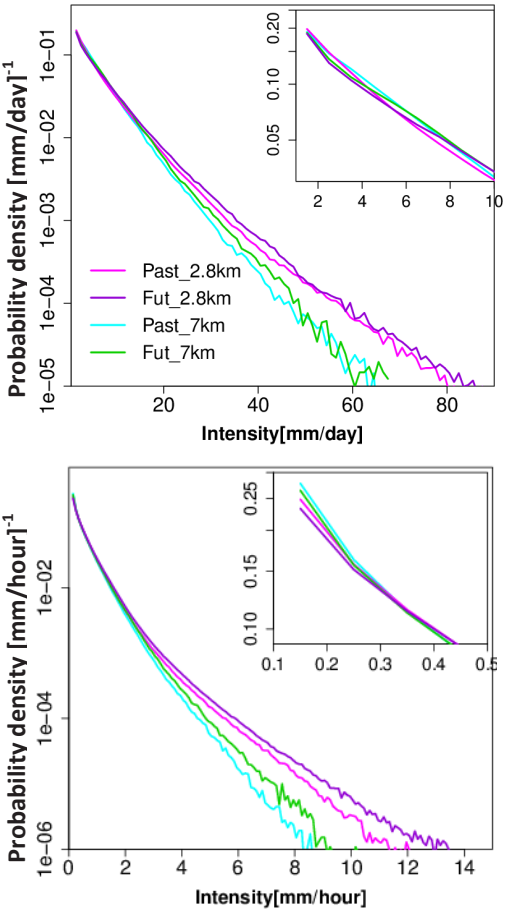

Figure 49: Probability distribution of daily (top) and hourly (bottom) precipitation in DJF for recent past 1971-2000 and near future 2021-2050 at 2.8 km and 7 km resolution; colours according to the legend. Note the logarithmic y-axis for both panels.

For future winters, Figure 49 top shows a slight increase (decrease) of intensities above (below) 5 mm/day. The number of days with heavy precipitation (i.e. P> 10 mm/day, Herrera et al. (2010) and Klein Tank et al. (2009)) will increase uniformly over the investigation area (not shown), while the increase in the number with very heavy precipitation (i.e. P> 20 mm/day, Herrera et al. (2010) and Klein Tank et al. (2009)) will concentrate in the areas above

300 m (not shown). This explains the above-mentioned changes in the spatial distribution of daily mean precipitation when considering only wet days (Figure 48).

For both resolutions, the percentage of dry days will increase by less than ~2% in the near future (Table 13). The augmentation is quite well spread over the whole investigation area with some peaks over the top of the hills (not shown). The changes in dry days and in the probability distribution compensate each other in the calculation of daily mean precipitation, including all days resulting in almost no difference between past and future (Figure 48, top).

Table 13: Comparison between the past (1971-2000) and future (2021-2050) winters for 2.8 km and 7 km spatial resolution of the percentage of dry days and hours, maximum number of consecutive dry days and number of dry periods. For the latter two, the minimum, the maximum and the mean value of the index over the investigation area are provided. A dry period is defined as at least five consecutive days without rain (Klein Tank et al. 2009).

	2.8 km		**7 km**	
	Past	**Future**	**Past**	**Future**
Percentage of dry days	47 %	49 %	39 %	41 %
Percentage dry hours	75 %	75 %	72 %	72 %
Maximum number of consecutive dry days	15-29 Mean 25	19-37 Mean 24	14-26 Mean 22	19-26 Mean 20
Number of dry periods	32-79 Mean 50	34-77 Mean 55	23-57 Mean 41	28-59 Mean 42

The dry periods will become slightly longer (Table 13) in the valleys up to a maximum of + 13 days, while there will be a general decrease anywhere else, more marked on the south-eastside of the domain (not shown). Note

that the maximum (minimum) values between past and future in Table 13 do not necessarily refer to the same grid point. Thus, it is possible to have a decrease in the maximum duration of a dry period although this index shows an increase of its minimum value in the future. The dry periods will also become more frequent, on average rising from 50 dry periods in the past to 55 in the future (Table 13). This trend will affect especially the foothills in the south (beginning of the Black Forest), while the hills in the northern part will be less affected by the change.

On an hourly base, the probability distribution shows a clear increase for the intensities above 0.35 mm/hour especially for higher spatial resolution (Figure 49 bottom). This means that in the near future precipitation will become heavier than in the past. Nevertheless, it is important to notice that the "extreme" precipitation in winter reaches a maximum of 24 mm/hour that is not so extreme compared with the summer maximum of 140 mm/hour (not shown in the graphs because of their extremely low probability). The increase in hourly intensities finds a correspondence in the diurnal cycle of precipitation. Figure 50 bottom shows a slight increase in magnitude from 12:00 and early morning (midnight) for 2.8 km (7 km) when all hours are included. For both resolutions, the trend becomes even more accentuated if taking into account only wet hours (Figure 50 middle). The diurnal cycle changes its shape from past to future when considering only hourly precipitation above 5 mm (Figure 50 top). In particular, for 2.8 km simulations the precipitation shows a strong maximum at 12:00. This, together with an increased water vapour (not shown) and temperature (Figure 51), might be an indicator of an increase in convective activities in line with the findings by Giorgi et al (2004) for future winters. However, due to the higher hourly threshold selected (i.e. 5 mm/hour), the amount of data used for the calculation of the latter diurnal cycles is strongly reduced compared

with the previous sampling especially for coarser resolution. Thus statistically the diurnal cycle could be not significant.

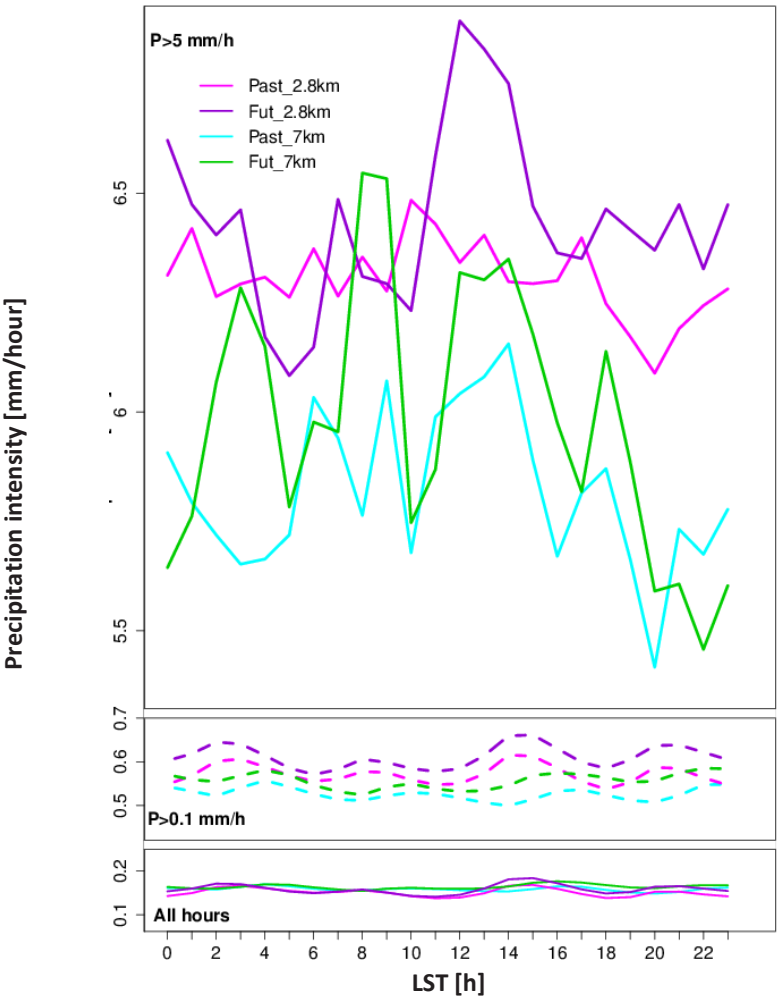

Figure 50: Diurnal cycle of precipitation calculated considering all hours (bottom), only wet hours (middle) and with precipitation intensity above 5 mm/hours (top) in DJF for recent past 1971-2000 and near future 2021-2050 at 2.8 km and 7 km resolution; colours according to the legend.

In agreement with previous literature, future winters will be 1-2 °C warmer than in the recent past (Wagner et al. 2012). The changes will affect the whole investigation area with the only exception for the hills above 700 m (Figure 51); similar findings are also found at 7 km resolution (not shown). Compared to the past, the diurnal cycle of temperature in the future will not change its shape (not shown). On the other hand, its magnitude will increase uniformly during the day with maximum temperatures around 13:00 equal to 4.6 °C in the future and 3°C in the past. Wagner et al (2012) found that the projected temperature change signal is mainly due to the forcing, with little impact from the RCM. However, the higher temperature could also be linked to a reduced cloud cover both at low and medium level (Figure 52), although there are no changes in either surface longwave or shortwave radiation (not shown). Note that the differences between 2.8 km and 7 km resolution in the representation of cloud cover are not related to the ECHAM5 forcing but to the higher resolution, as already pointed out in Chapter 5.4.2.

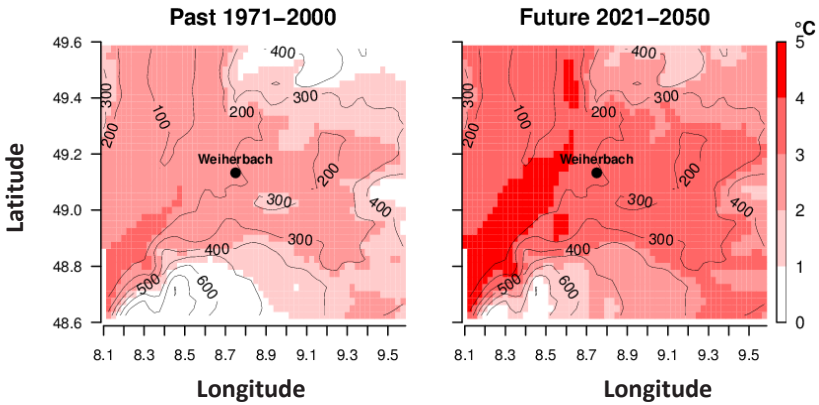

Figure 51: Spatial distribution of daily mean temperature at 2 m in winter for the recent past 1971-2000 (left) and near future 2021-2050 (right) at 2.8 km resolution. The contour lines represent the orography.

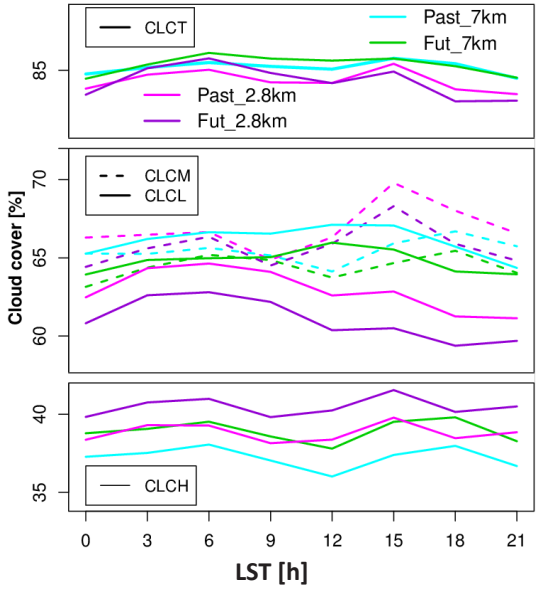

Figure 52: Diurnal cycle of cloud cover for total (CLCT, top panel), medium and low (CLCM and CLCL, middle panel), and high cloud (CLCH, bottom panel) in DJF for recent past 1971-2000 and near future 2021-2050 at 2.8 km and 7 km resolution; colours according to the legend.

6.4.2 Climate change in summer

Figure 53 shows the spatial maps of daily mean precipitation in summer for the recent past (left) and near future (right) at 2.8 km resolution. The spatial pattern of precipitation is very similar between past and future with or without considering dry days (respectively top and bottom panel in Figure 53). In the first case, a general reduction in mean intensities is visible in the whole investigation area and especially over the hills above 400 m. When considering only wet days, the situation reverses, with a general rise in mean precipitation from 7 mm/day to 8.5 mm/day and with maximum intensities over the hilly area equal to 19 mm/day (Figure 53, bottom).

A similar signal is found also at 7 km resolution (not shown), but the mean values are higher (lower) if all days (only wet days) are considered due to the strong overestimation of wet days at this resolution, as seen in Chapter 5

Figure 30, in Berg et al. (2012) and in Table 14. In order to understand the different signal when considering or not only wet days, it is important to evaluate the percentage of dry days as well as the probability distribution of precipitation intensities.

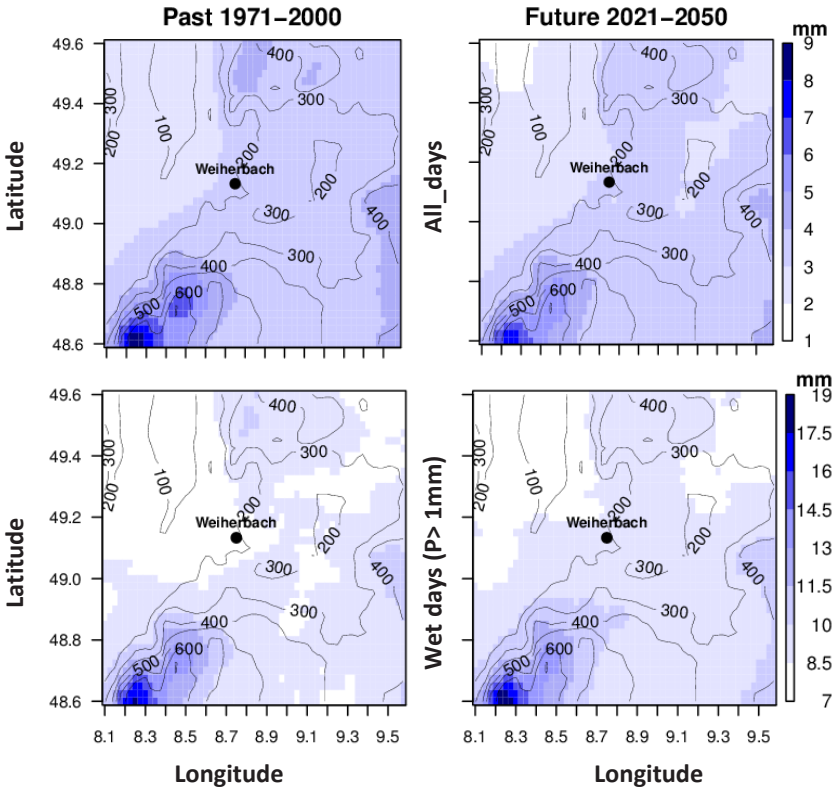

Figure 53: Spatial distribution of daily mean precipitation in summer for the recent past 1971-2000 (left side) and near future 2021-2050 (right side) at 2.8 km resolution. Top panels consider all days while the bottom ones only rainy days (precipitation above 1 mm/day). The contour lines represent the orography of the area.

In the near future, the number of dry days will rise by 4% (5%) at 2.8 km (7 km) resolution (Table 14). Although the increase is widely spread, the hills at the beginning of the Black Forest are the area mostly affected by the change (not shown). At 2.8 km resolution, the maximum number of consecutive dry days will increase uniformly over the investigation area from 23 to 30 days (Table 14). These values represent a mean over the whole investigation area while the table offers also the minimum and maximum values registered within the investigation area. The above-mentioned trend is confirmed by the increase in the number of dry periods, defined as periods of more than five consecutive dry days (Klein Tank et al. 2009; Wagner et al. 2012). On the other hand, the latter change will affect mainly the beginning of the Black Forest, where the number of dry periods will increase by 30% (not shown). Coarser resolution shows the same tendency as higher resolution (Table 14 and Wagner et al. 2012). However, at 7 km resolution the relative differences between past and future are higher, while the absolute values are lower compared to higher resolution.

Table 14: Comparison between the past (1971-2000) and future (2021-2050) summer for 2.8 km and 7 km spatial resolution of the percentage of dry days, maximum number of consecutive dry days and number of dry periods, defined as at least five consecutive days without rain (Klein Tank et al. 2009). For the latter two, the minimum, the maximum and the mean value of the index over the investigation area are provided.

	2.8 km		**7 km**	
	Past	**Future**	**Past**	**Future**
Percentage of dry days	62 %	66 %	51 %	56 %
Maximum number of consecutive dry days	17 - 41 mean 23	22 - 67 mean 30	13 - 27 mean 17	22 - 34 mean 29
Number of dry periods	67 - 122 mean 93	83 - 125 mean 103	36 - 86 mean 57	60 - 108 mean 77

In Figure 54a, the probability distribution of daily precipitation shows a slight increase of the lower intensities (below 4 mm/day) and a decrease of medium intensities between 4 and 15 mm/day. In addition, the spatial distribution of these types of events modifies in the near future. The number of heavy and very heavy precipitation days will decrease on the hills above 500 m while the valley will experience an increase in them (not shown).

Figure 54b shows that precipitation above 50 mm/day will be more frequent and reach higher intensities (more than 250 mm/day versus maximum 185 mm/day in the past). Previous chapters showed that 2.8 km tends to overestimate precipitation intensities above 20 mm/day when driven with ERA40 forcing (Chapter0 Figure 30) and that the error is reduced, but still present in ECHAM5 driven simulations (Chapter 6.3). The conclusions from Figure 54 are in good agreement with previous literature on coarser resolution (Feldmann et al. 2012). In fact, also in our case, 7 km resolution shows an increased probability of more extreme precipitation events although the absolute change is minor compared with higher resolution.

Stepping to an hourly scale, a signal similar to the daily scale is found in terms of dry hours (Table 15). Both resolutions show an increase in them of between 1 and 2% in the near future. Figure 55 shows a decrease in precipitation intensities between 0.5 mm/hour and 2 mm/hour in the near future and a light increase for medium intensities between 5 and 17 mm/hour for both resolutions. Above the latter threshold, no differences can be seen from Figure 55.

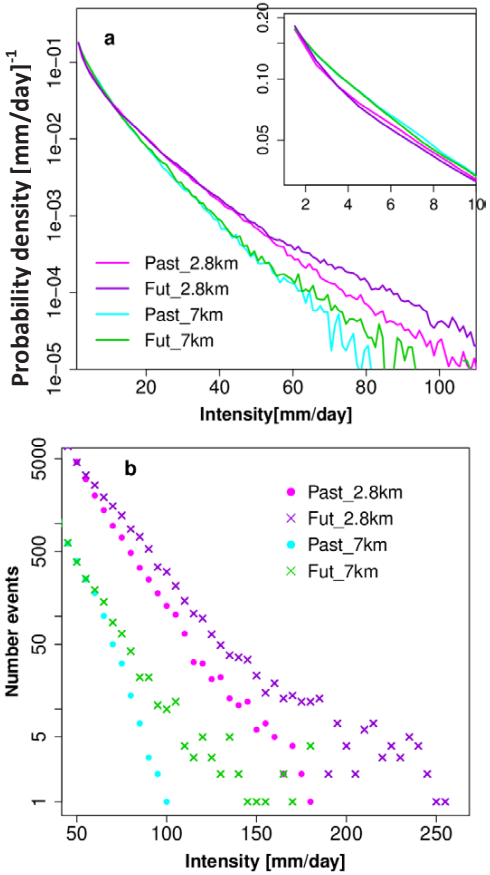

Figure 54: Panel a shows the probability distribution of daily precipitation for JJA comparing past and future at 2.8 km and 7 km spatial resolution (colour and symbols according to the legend). Panel b shows for the same datasets the number of events with higher intensities. Note the logarithmic y-axis for both panels.

Dry hours	Past	Future
2.8 km	87 %	88 %
7 km	83 %	85 %

Table 15: Percentage of dry hours in the recent past (1971-2000) and near future (2021-2050) for 2.8 km and 7 km spatial resolution.

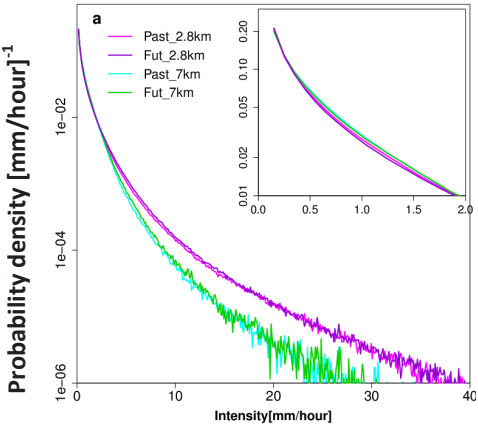

Figure 55: Probability distribution of hourly precipitation for JJA comparing past and future at 2.8 km and 7 km spatial resolution (colour and symbols according to the legend.

The following analysis based on the events tries to bridge the gap between the two temporal scales used up to now (i.e. day and hours). An event starts when the precipitation is above 0.1 mm/hour and it stops when it drops below this threshold. For the simulations at 2.8 km resolution, the duration and the amount of each event is calculated for each grid point for the summer season. The events are divided into sets according to their duration and amount of precipitation produced. Then, the number of events within each set is calculated. Note that this method could lead to an oversampling of large-scale events. In fact, this type of precipitation likely affects more than one grid point at the same time. Thus, the same events would be accounted twice in the calculation of contiguous grid points.

Figure 56 displays the number of events for each set for the past (left) and the future (right). The sets have a step of 10 mm/event and 5 hours for amount and duration respectively, i.e. the first set of events is characterised by an amount of precipitation between 0.1 and 10 mm produced within 5 hours; the events of the second set produce - in the same time (i.e. 5 hours) - an amount of precipitation between 11 and 20 mm and so on. The same is procedure is followed of increasing the duration with a step of 5 hours and

keeping the amount constant. Note that the scale represents the number of events registered in 30 years of simulation.

In the past, most of the events do not exceed 130 mm/event but they last a long time, up to a maximum of four days (Figure 56 left). By contrast, in the future the events will usually last no more than 2-3 days, but they will generate a higher amount (Figure 56 right). In addition, the model simulates for the future a branch of long events of more than two days producing a huge amount of precipitation of up to 540 mm/event in the worst case. On the other hand, their occurrence is limited to a maximum of 100 cases in 30 years and thus highly uncertain.

This type of analysis provides more information than a standard probability density distribution, where variations within a day can compensate each other and thus hide information. The probability distribution on daily data in Figure 54 showed no strong difference for intermediate intensities (i.e. 15-50 mm/day) between past and future. Now Figure 56 (bottom) using the event scale shows that differences between past and future also exist within a day (i.e. 24 hours in the figure) for these intensities. In particular, there will be a decrease in the number of short events with low intensities (0-10 hours with 0-60 mm/event; in red in Figure 56) accompanied by an increase of events lasting 10-20 hours with intensities between 20 and 90 mm/event (in blue in Figure 56). The tail of the probability distribution in Figure 54b finds a confirmation in Figure 56 with an increase of events above 90 mm/event and duration below 25 hours. Figure 56 shows also a strong reduction in the number of events longer than 30 hours, not visible in the probability distribution based on daily data. This could be linked to a reduction in large-scale precipitation in good agreement with previous findings (Giorgi et al. 2004).

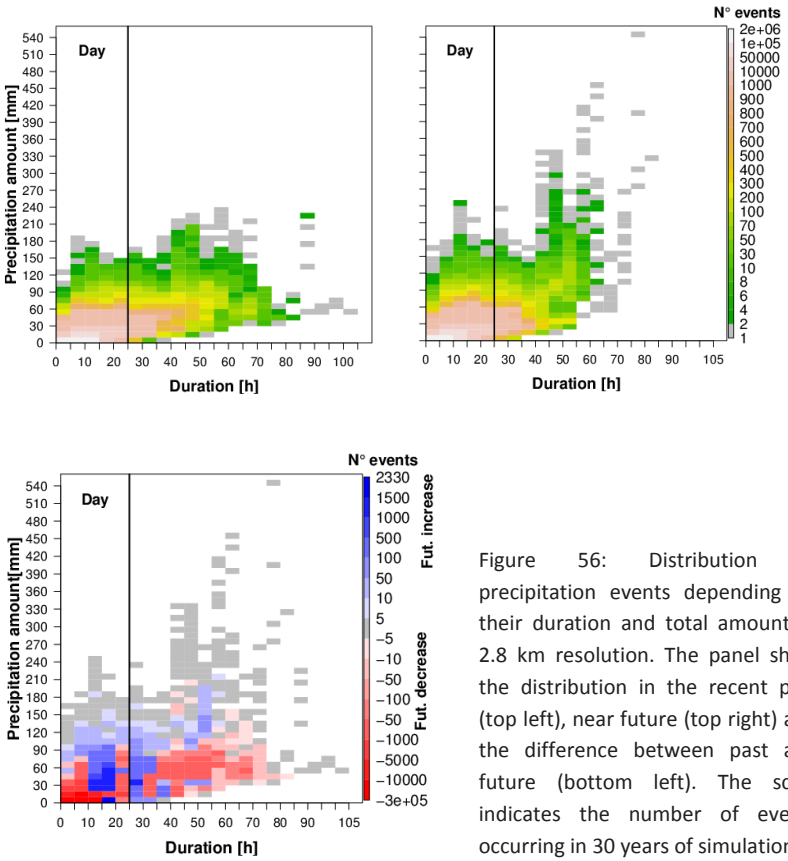

Figure 56: Distribution of precipitation events depending on their duration and total amount at 2.8 km resolution. The panel show the distribution in the recent past (top left), near future (top right) and the difference between past and future (bottom left). The scale indicates the number of events occurring in 30 years of simulation.

A very interesting change in the near future is the strong reduction of 14% in the total number of events. This decrease confirms the above-mentioned trend of longer and more frequent dry periods (Table 14). Moreover, the total amount of precipitation does not substantially reduce over the valley (only -300 mm in 30 years), as one might expect given the reduction in the total number of events. These findings lead to the conclusion that future precipitation will occur less frequently, the events will be shorter but more intense.

The analysis continues investigating how the diurnal cycle of precipitation and CAPE will change in the near future, in comparison with the recent past, for both spatial resolutions (i.e. 2.8 and 7 km) depending on the hourly threshold selected. For each grid point, where the hourly precipitation is above the selected threshold, both precipitation and CAPE data are selected and used for the calculation of their diurnal cycle. The cases analysed are for all hours (Figure 57 top row), wet hours (Figure 57 middle row) and hours with precipitation intensities above 5 mm/hour (Figure 57 bottom row). Note that at 7 km resolution the data above the higher threshold are substantially less than at higher resolution; therefore the results should be handled with care because they are highly uncertain.

At both resolutions, the shape of the diurnal cycles is in most of the cases retained in the future, but the intensities can change to some extent. Considering all hours (Figure 57, top row), the characteristic afternoon and morning peaks of 2.8 km resolution will attenuate in the future, while at 7 km the maximum will remain unchanged and the decrease will affect the rest of the curve. The diurnal cycle of CAPE does not shows any relevant difference between past and future apart from a slight decrease between 15:00 and 18:00, more accentuated at higher spatial resolution.

These findings are distorted by the lessening of 2% in the number of dry hours (Table 15). In fact, by removing them the above-mentioned future decrease in the precipitation intensities at convection-permitting scale disappears (Figure 57, middle left versus top left panel). By contrast, the future precipitation becomes more intense at 9:00 and 22:00 at higher resolution, while a systematic increase is found at coarser resolution.

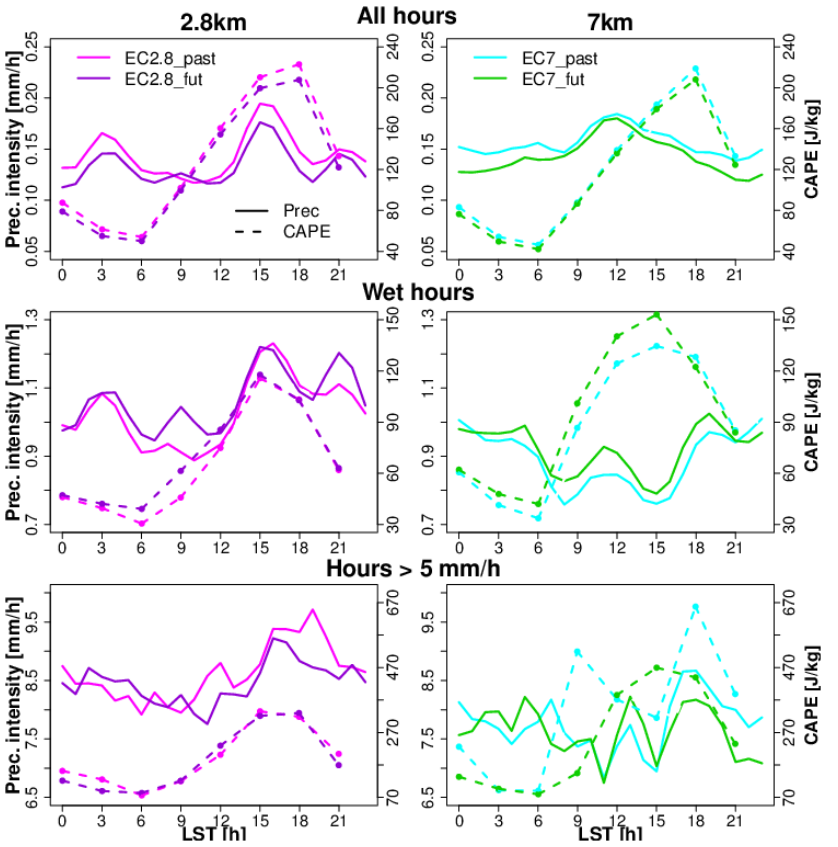

Figure 57: Diurnal cycle of precipitation (solid line) and CAPE (dashed line) calculated considering all hours (top), only wet hours (middle) and precipitation intensity above 5 mm/hours (bottom) in JJA at 2.8 km (left) and 7 km (right) resolution for recent past 1971-2000 (pink/light blue for 2.8 km/7 km) and near future 2021-2050 (purple/green for 2.8 km/7 km). Note that the model outputs precipitation and CAPE respectively every hour and every three hours.

Note that the diurnal cycle of the percentage of dry hours, both in the past and future (not shown), has the minima at 3:00 and 15:00 (between 11:00 and 15:00) at 2.8 km (7 km) resolution in correspondence with the precipitation maxima. At 2.8 km the maximum difference in the percentage of dry

hours between past and future is found in the early morning until 7:00 and then between 14:00 and 19:00. Thus, the future changes in the number of dry hours can justify the alteration of the precipitation pattern, - whether or not considering dry hours- in the early morning and afternoon but not completely the peaks at 9:00 and 22:00. These peaks are thus probably related to future higher intensities or more frequent precipitation during these hours. For the simulations at 7 km, the diurnal cycle of the dry hours cannot cause the changes in the precipitation diurnal cycle- whether or not considering dry hours- either in the past or in the future.

Focusing on hours with a precipitation above 5 mm/hour (Figure 57, bottom row), the findings are very interesting, both for the shape of the diurnal cycles of precipitation in the past and for its change in the future. First comparing the two resolutions in the past (Figure 57, bottom, pink/light blue for 2.8/7 km resolution), one can immediately notice that 2.8 km has mean precipitation spanning from 8 mm/h to more than 9.5 mm/h while 7 km never exceeds 8.5 mm/hour.

The higher values at convection-permitting scale are due to a better representation of hourly precipitation intensities (see Chapter 5 Figure 32). Comparing this precipitation diurnal cycle with those above at higher resolution (Figure 57, bottom left versus top and middle row, left column), the morning peaks disappear, while the afternoon maximum starts one hour later (i.e. 16:00) and continues until 19:00 when it reaches the maximum intensities. Thus, higher precipitation intensities seem to be related with convective activities in the afternoon.

Few similarities can be found with coarser resolution; 7 km also has a maximum in the afternoon around the same time as 2.8 km, but in addition it presents other two peaks around 7:00 and 13:00 (Figure 57, bottom right in

light blue). None of the peaks is prominent over the others as with the convection-permitting scale. For the near future, the shape of the precipitation diurnal cycle is similar to the past, for both resolutions. However, the afternoon peak will be weaker and shorter, while there will be an increase in the morning precipitation between 2:00 and 6:00, probably linked with large-scale weather patterns (Figure 57, bottom row). These findings disagree with the probability distribution on an hourly basis, which did not show any relevant change between past and future (Figure 55). However, the probability distribution for the morning hours (i.e. 00:00 to 11:00) shows an increase in precipitation intensities above 5 mm/hours (not shown). Similarly, considering the hours between 13:00 and 19:00, one can find a slight decrease in precipitation intensities above 15 mm/hour (not shown) only at convection-permitting scale. In fact, at coarser resolution, the opposite signal is found with an increase in precipitation intensities above 5 mm/hour. Thus, it is important not only to consider higher temporal scales for the analysis but also consider slices of a day.

Figure 57 also plots the diurnal cycle of CAPE calculated for the hours, which are characterized by a precipitation above the selected hourly thresholds. In both cases, for thresholds above 0.1 mm/hour and 5 mm/hour, there is a good correspondence between high CAPE and the occurrence of convective precipitation at 2.8 km, as already seen in Chapter 5.4.2. At this resolution, the diurnal cycle of CAPE is not modified in the future either in terms of shape or intensities. This, together with a decrease in the higher intensities of hourly precipitation between 11:00 and 19:00 (not shown), could mean that there will be no strengthening of convective activities in the near future. For the Mediterranean regions, Giorgi et al (2004) found that the convective precipitation fraction will decrease in future summers, but this effect will be counterbalanced by an increase in the amount of atmospheric water vapour thus generating higher precipitation intensities on a daily basis. The same

hypothesis could be applicable to our case (see increase in integrated water vapour in Figure 59). Interestingly, at 7 km resolution, CAPE values are higher than at the convection-permitting scale when considering precipitation thresholds of 0.1 mm/h and 5 mm/hour. However, these higher values of CAPE do not translate into higher precipitation amounts compared to higher spatial resolution. This could be linked to the parameterisation of convection, which to some extent decouples the status of the boundary layer with the occurrence of convection (Baldauf et al, 2011).

The precipitation diurnal cycles based on an hourly thresholds, displayed in Figure 57, do not account for the durations of the precipitation. A precipitation with low/medium hourly intensities but lasting longer can generate a large daily amount, which would not be visible in a diurnal cycle base on an hourly threshold. Moreover, calculating the diurnal cycle of CAPE base on the hours with a precipitation above a selected threshold (as in Figure 57) could be misleading. In fact, CAPE is usually higher before a convective event and not necessarily at the moment of its occurrence. Thus, the same type of analysis as for Figure 57 is performed, using a precipitation daily threshold. A direct correspondence between hourly and daily thresholds does not exist. Translating the 5 mm/hours limit on a daily basis by simply multiplying it for 24 hours would lead to a daily threshold of 120 mm/day, which is extremely high (see probability distribution on daily basis in Figure 54). Moreover, it is quite unlikely that it rains continuously for 24 hours with the same intensity, especially if high. The standard limit to distinguish between precipitation and drizzle is 1 mm/day; thus, this is the first selected daily threshold. The second, 50 mm/day, is a good compromise between an intense event on a daily (see Figure 54) and on an hourly scale (corresponding to a continuous precipitation with ~2 mm/hour intensity). Figure 58 shows the diurnal cycle of precipitation and CAPE for days with precipitation of above-mentioned daily limits (i.e. 1 mm/day and 50 mm/day).

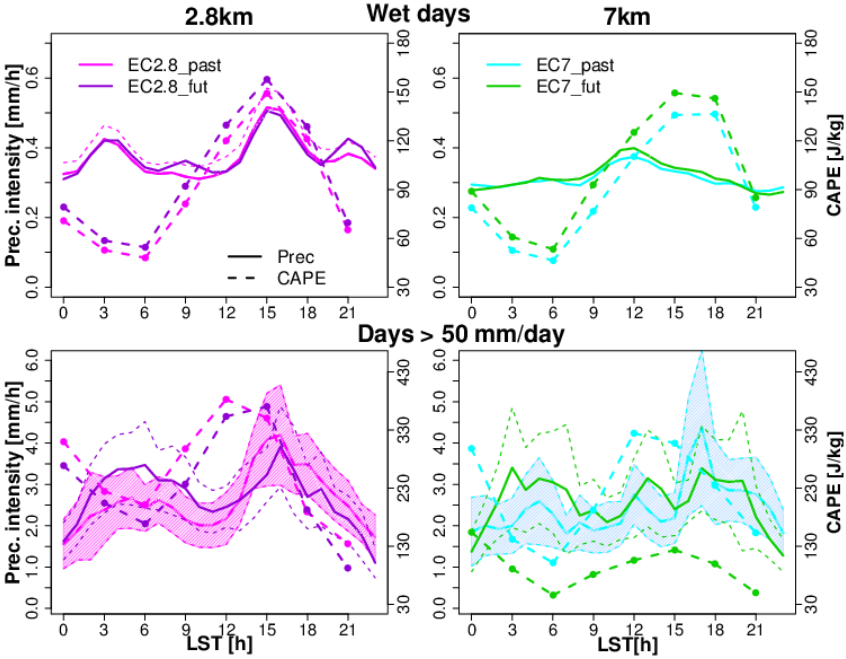

Figure 58: Diurnal cycle of precipitation (solid line) and CAPE (thick dashed line) calculated considering only wet days (top) and with precipitation intensity above 50 mm/day (bottom) in JJA at 2.8 km (left) and 7 km (right) resolution for recent past 1971-2000 (pink/light blue for 2.8 km/7 km) and near future 2021-2050 (purple/green for 2.8 km/7 km). Shaded areas and light dashed lines indicate the 95% confidence interval. Note that the model outputs precipitation and CAPE respectively every hour and every three hours.

At convection-permitting scale, the precipitation diurnal cycles have a similar shape both considering only wet hours (Figure 57 middle row left) and wet days (Figure 58 top left), but with lower values for a daily threshold. This is related to hourly intensities lower than 0.1 mm/hour that can exist within a day. By contrast, CAPE values are higher in Figure 57 than in Figure 58 because the hours before a convective event are also considered in this case. In terms of climate change, the signal is similar to that registered before in the case of an hourly threshold of 0.1 mm/h. The 7 km resolution is highly sensi-

tive to the selection of the threshold. Considering only wet days (Figure 58 top), the diurnal cycle of precipitation is very similar to the one considering all days (i.e. all hours, Figure 57 top right), while it changes substantially when considering only wet hours (Figure 57 middle right). This is probably linked to the overestimation of lower intensities at this resolution (see chapter 5.4.1).

The analysis now focuses on the comparison between the precipitation diurnal cycles at 2.8 km for the upper thresholds of 5 mm/hour and 50 mm/day (Figure 57 and Figure 58, bottom rows). For the past, in the latter case (i.e. 50 mm/day), the precipitation reaches its maximum intensity at 16:00 and decreases immediately afterwards, while for the case of the 5 mm/hour threshold the precipitation was peaking again at 19:00. These changes indicate that the events at 17:00 and 19:00 are short showers that do not generate high amounts on a daily basis but have high hourly intensity. Note in fact that the diurnal cycle based on an hourly threshold of 5 mm/hour has substantially higher precipitation intensities than in the case of a daily threshold of 50 mm/day. Moreover, the morning maximum has the same intensities as the afternoon one when considering a daily threshold. This is related to the combination of precipitation intensities and their duration. The morning precipitation, mainly related to large-scale processes, has usually lower hourly intensities but longer duration than convective precipitation. Thus it can generate high amounts of precipitation on a daily basis, which are not so evident when considering an hourly threshold. Thus, the changes in the daily threshold would affect the prominence of the morning precipitation in comparison with the afternoon maximum (e.g. lower (higher) thresholds than 50 mm/day would reduce (increase) the morning (afternoon) precipitation intensities in the diurnal cycle.

In the future, the precipitation diurnal cycle at 2.8 km simulation calculated for a daily threshold of 50 mm/day shows two main changes compared to the past (violet line versus pink line in Figure 58, bottom left). First, there is a net increase in the morning precipitation, which is most probably related to large-scale weather patterns since is also present at coarser resolution. Second, the afternoon maximum slightly decreases in intensity and duration. Although less evident, these changes were also present in the diurnal cycle for an hourly threshold of 5 mm/hour (Figure 57 bottom). Thus they do not depend on the selected threshold. It has to be underlined that the above-mentioned changes are not statistically significant. This could depend on the future period selected for the investigation, namely 2021-2050. In this period in fact the climate change signal is likely to be less strong than at the end of the century. Also at coarser resolution, Wagner et al. (2012) found that the seasonal changes between past and future were not statistically significant.

The CAPE values in the diurnal cycle are much higher when considering a daily precipitation threshold of 50 mm/day than for an hourly threshold of 5 mm/hour. The same was also found at convection-permitting scale in the comparison between wet days and wet hours (Figure 58 top left and Figure 57 middle left). In the latter case, the shape of the CAPE diurnal cycle did not change when selecting either an hourly or daily threshold. By contrast, using a 50 mm/day threshold at the convection-permitting scale causes the maximum CAPE three hours earlier (i.e. maximum between 12:00 and 15:00 (Figure 58 bottom left) than in the case of an hourly threshold of 5 mm/hour (i.e. maximum between 15:00 and 18:00; Figure 57 bottom left). This shifting is not in agreement with the diurnal cycle of precipitation, which has the maximum at 16:00. Thus, on the one hand, considering the hours before a convective event leads to higher value of CAPE; on the other, considering a daily threshold seems to lead to an incorrect diurnal cycle of CAPE due to the

inclusion in the calculation of days with high precipitation amount in the morning but not in the afternoon (i.e. not related with strong convective events). However, this could also depend on the fact that CAPE is output by the model every three hours while precipitation is output every hour. The diurnal cycles calculated for a precipitation threshold of 50 mm/day from 7 km simulations are highly uncertain because of the few data available above this threshold (see the large confidence interval in Figure 49). Nevertheless, it is interesting that 7 km resolution for this threshold provides similar conclusions to convection-permitting scale in terms of climate change signal, i.e. an increase (decrease) in morning (afternoon) precipitation (Figure 58, bottom right).

The comparison between the two resolutions in terms of climate change signal continues when considering other atmospheric variables, namely integrated water vapour, temperature and radiation fluxes (Figure 59). Already from a first look, one notices that there is no difference in the climate change signal between resolutions. Both of them show an increase in the integrated water vapour of ~2 kg/m^2 along with a rise of ~2 °C in temperature in line with previous findings (Giorgi et al. 2004). Philipona (2005) found that changes in the former are strongly connected with changes in the latter, with regions of warming experiencing increasing moisture and vice versa. The changes in both temperature (Figure 60) and integrated water vapour (not shown) show higher values in the Rhine valley. The simulations show a slight increase (decrease) in shortwave (longwave) net radiation. Note that the longwave radiation has a negative sign and thus to increase in the future, its value should become more negative. These latter changes seem to depend upon the rise in direct radiation. In turn, this is linked with the reduction of more than 5% in cloud cover, which is particularly relevant for low and medium clouds (Figure 61). Giorgi et al. (2004) suggested that the reduction in cloudiness depends on an enhancement of the precipitation efficiency (i.e.

the ratio of precipitation over the total cloud water column). Longer and more frequent dry periods will likely lead to a drier soil condition, which could explain the irrelevant differences in evapotranspiration between past and future (not shown); this hypothesis would need further investigation.

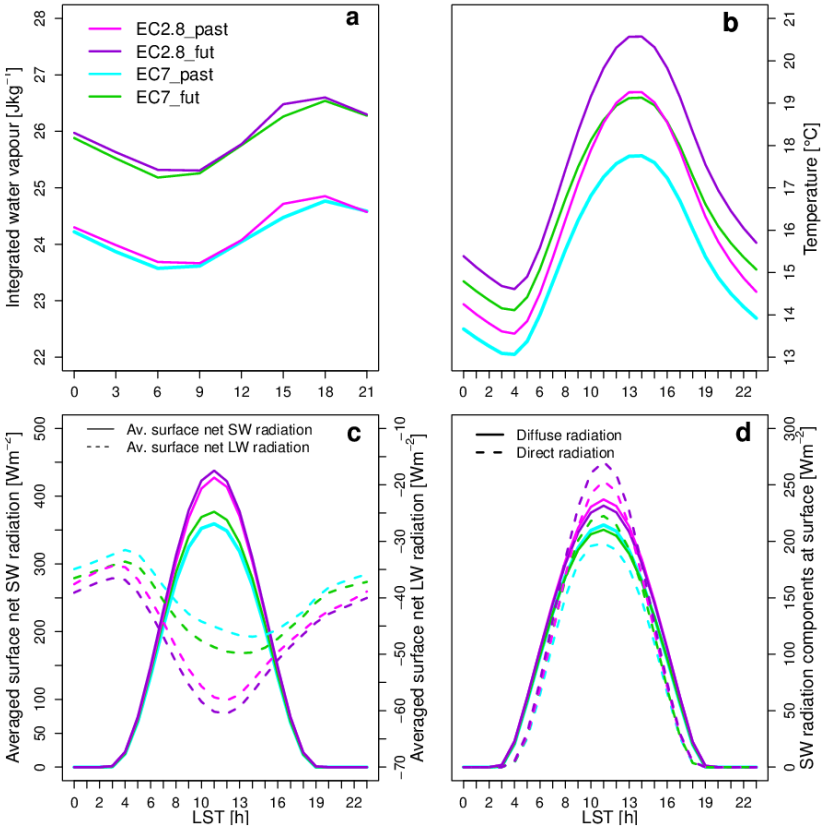

Figure 59: All the panels show the diurnal cycles for EC2.8_past (pink), EC2.8_fur (purple), EC7_past (light blue) and EC7_past (green) in JJA. The variables shown are respectively: panel a, integrated water vapour; panel b, temperature at 2 m from the surface; panel c, averaged surface net shortwave and longwave radiation (solid and dashed line respectively). Note that radiation is positive when directed downward. Panel d represents the surface shortwave radiation components for both diffuse (solid line) and direct (dashed line).

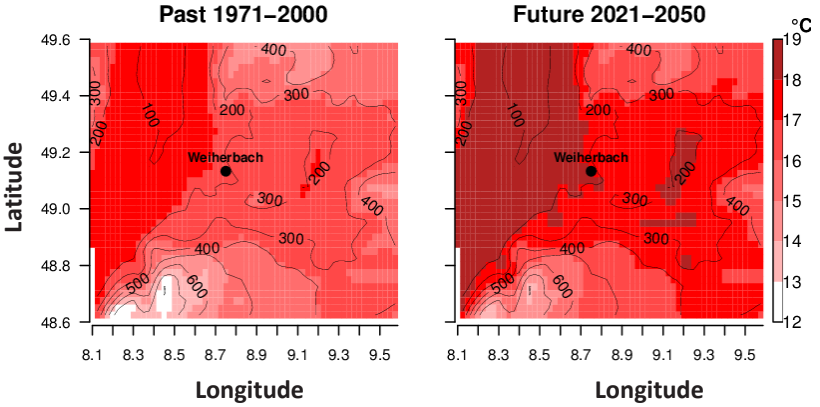

Figure 60: Spatial distribution of daily mean temperature at 2 m in summer for the recent past 1971-2000 (left) and near future 2021-2050 (right) at 2.8 km resolution. The contour lines represent the orography of the area.

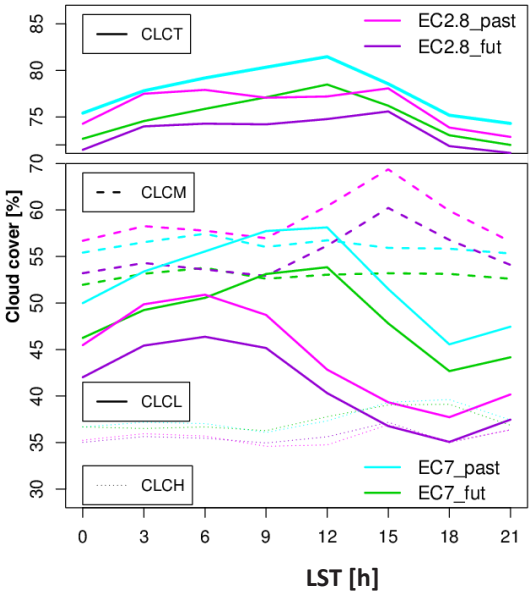

Figure 61: Diurnal cycle of cloud cover for total (CLCT, top panel), medium and low (CLCM and CLCL, middle panel), and high cloud (CLCH, bottom panel) in JJA for recent past 1971-2000 and near future 2021-2050 at 2.8 km and 7 km resolution; colours according to the legend.

6.5. Summary and conclusion

This chapter investigated the climate change signal at convection-permitting scale for the investigation area around Weiherbach. The first goal of this chapter was to determine if higher resolution simulations provide a climate change signal in line with coarser simulations. The second was evaluating if and to what extent increasing spatial scale can bring additional information on future changes in the precipitation pattern and eventually the reasons leading to them. In this context, the ECHAM5 model is used to force two climatological model simulations of 30 years in the recent past (1971-2000) and near future (2012-2050), at 7 km and 2.8 km resolution. The comparison between the two resolutions considers both winter and summer, when the climate change signal is more evident (Feldmann et al. 2012; Giorgi et al. 2004). However, a more detailed investigation is performed for the summer time since this is the period of the year when the added value of convection-permitting scale becomes evident (Fosser et al. 2014) and the climate change signal is more heterogeneous (Feldmann et al. 2012).

Before investigating the climate change signal, the effects of the change in the forcings (i.e. from ERA40 driven to ECHAM5 driven simulations) are evaluated for the period 1971-2000 at both resolutions. Consistent with previous findings by Berg et al. (2012) and Feldmann et al. (2008), ECHAM5 driven simulations highly overestimate the number of wet days especially in winter, which causes a strong bias in daily mean precipitation especially at coarser resolution. The probability distribution of daily precipitation intensities shows that the model is not sensitive to the change of the forcing in winter, while in summer differences can be found mainly at higher resolution. On an hourly basis, the use of ECHAM5 as forcing data leads to an underestimation of higher intensities compared to ERA40 driven simulations especially in winter and at higher resolution. This underestimation seems to have the strong-

est impact on erosion modelling. Using CATFLOW-SED model, Antonetti (2013) found that using ECHAM5 driven simulations, instead of ERA40 driven ones, leads to an underestimation of soil erosion by 20%. Similar results were found with the LISEM erosion model (personal communication with Mrs Kempf from GEOMER GmbH; De Roo et al. 1996).

Compared to the HYRAS dataset, ECHAM5 driven simulations present in winter a similar cold bias limited to 1 K. In summer, higher resolution reduces the cold bias of coarser resolution by ~2 K. This is in contrast with previous literature stating that downscaling ECHAM5 driven simulations from 50 km to 7 km does not modify the magnitude of the initial bias (Berg et al. 2012). Most probably this difference in the findings is due to different treatment of deep convection at 7 km and 2.8 km. Switching off the convective parameterization at convection-permitting scale reduces the overestimation in cloud cover affecting coarser resolution (Fosser et al. 2014; Will and Woldt 2009), and thus could lead to a better representation of daily mean temperature.

In winter, the climate change signal at convection-permitting scale projects an increase in the number of dry days. Moreover, the Rhine valley will experience longer dry periods while their frequency is projected to rise by 5% uniformly over the whole Weiherbach area. This drier climate will be accompanied by a warming of 1-2 °C, likely due to the forcing over most of the investigation area. The future increase in the intensities above 5 mm/day leads to an increase of ~2mm/day in daily mean precipitation especially over the hilly areas when considering only wet days. On an hourly basis, the simulations project a strong increase in precipitation intensities above 2 mm/hour, which seems to occur mainly around midday.

In summer the simulations in high resolution project an increase in the number of dry days (+4%) as well as in the length and frequency of the dry peri-

ods, in line with previous literature (Feldmann et al. 2012; Wagner et al. 2012). These trends will affect more the foothills of the Black Forest, where the number of dry period will increase by 30%. The probability distribution of daily precipitation shows a decrease in medium intensities (i.e. 4 - 15 mm/day) and an increase in intensities above 50 mm/day in good agreement with previous literature on coarser resolution (Feldmann et al. 2012). However, the spatial distribution of heavy and very heavy precipitation days seems to change in the near future, with an increase of them in the valley and an opposite trend over the hills above 500 m. The probability distribution of hourly precipitation intensities shows almost no differences between past and future especially for intensities above 17 mm/h. This underlines the importance of the selection of the temporal scale used to investigate the climate change signal. The event base analysis projects a decrease in short events with low intensities (0-10 hours with 0-60 mm/event) and an increase in those with intensities between 20 and 90 mm/event and lasting between 10 and 20 hours. Moreover, events longer than a day will reduce substantially. In addition, the climate change signal projects a reduction of 14% in the total number of precipitation events for the near future, compatible with the above-mentioned increase in dry days and periods. Thus, in future summers the precipitation will occur less frequently; the events will be shorter but more intense.

An analysis of the climate change signal is performed considering the diurnal cycle of precipitation for different hourly and daily thresholds. The most relevant future change appears when calculating the diurnal cycle for days with a precipitation above 50 mm considering higher hourly and daily precipitation thresholds in the calculation of the diurnal cycle. Selecting days with a precipitation above 50 mm/day, the ECHAM5 driven models project an increase in the morning precipitation (i.e. between 2:00 and 14:00) probably linked to future changes in the large-scale weather patterns. The same

trend, but less evident, is also present with the hourly threshold of 5 mm/hour). The projections at 2.8 km show a decrease in the afternoon precipitation and CAPE, with no relevant changes in magnitude compared to the recent past. Thus, it seems that there will be no strengthening of the afternoon convective processes in the near future.

Both resolutions shows an increase in the integrated water vapour of ~2 Kg/m^2 along with a rise of ~2 °C in temperature in line with previous findings (Giorgi et al. 2004). The warming affects mainly the Rhine valley, where the increase in humidity is more relevant. Shortwave net radiation is projected to slightly increase due to a rise in direct radiation, which in turn is linked with the reduction of more than 5% in cloud cover, especially at low and medium height.

In most of the cases, higher and coarser resolutions agree well on both the climate change signal and the relative magnitude of the changes, although they differ in absolute values. The only disagreement between resolutions in terms of climate change signal is found for the probability distribution of hourly precipitation between 13:00 and 19:00 in summer. Differences between resolutions remain in representation of the diurnal cycle of precipitation, CAPE and cloud cover. Although the latter differences are related to the possibility to resolve convection at 2.8 km, to have the diurnal cycle of precipitation correctly represented, at least in its shape, for the right reasons, makes the convection-permitting scale more reliable for investigating the climate change signal.

7. Final conclusion and outlook

The Fifth Assessment Report (AR5) of the Intergovernmental Panel on Climate Change made clear the consequences of the climate change and underlined the importance of adaptation strategies to deal with it (IPCC 2013). In this context, the KLIWA project "Bodenabtrag durch Wassererosion in Folge von Klimaveränderungen" aims to determine future soil erosion using climate modelling results for feeding erosion models. For this purpose, GCMs are too coarser and large uncertainties on the future climate remain for Central Europe (Christensen et al. 2007). RCMs can help to bridge the gap between coarse climate change information from global models and information needed at much higher resolution in certain region. However, at the moment, the highest spatial scale reached by most climate simulations is 7 km, which is still too coarse to simulate a process acting on small spatial and temporal scales like soil erosion (i.e. approx. 1km and < 1hour). Moreover, 7 km resolution shows strong deficiencies in the representation of convection, which is responsible for some of the most damaging weather phenomena (Brockhaus et al. 2008; Dai 2006; Dai and Trenberth 2004; Yang and Slingo 2001). Literature on model simulations in NWP mode proves that convection-permitting scale could be a viable way to have more reliable information for both past and future (Baldauf et al. 2011; Grell et al. 2000; Hohenegger et al. 2008; Lean et al. 2008; Mass et al. 2002; Miura et al. 2007; Richard et al. 2007; Schwartz et al. 2009; Weusthoff et al. 2010).

In this context, this research aims to achieve a deeper understanding of convection-permitting scale for simulations on climate scale (i.e. 30 years) and the benefit it can bring compared to coarser resolution. After defining the optimum model configuration to run long-term simulations at convection-permitting scale, this thesis analyses how the higher and coarser resolution represent convective precipitation and the atmospheric leading to it. The

climate change signal is then investigated at both resolutions to see if higher spatial scale can bring some additional information compared to coarser resolution.

The study focuses on the state of Baden-Württemberg in southwestern Germany with particular attention to the Weiherbach catchment, which has a high erosion risk. COSMO-CLM is used for the simulations and the HYRAS dataset as well as 45 measurement stations operated by DWD, for validation of the precipitation field.

Modelling at convection-permitting scale is highly computationally expensive in terms of both time and memory space required. Thus, a set of sensitivity studies at 2.8 km resolution was performed with the CLM model driven by ERA40 reanalysis data in order to determine the optimum simulation domain and model configuration for convection-permitting scale simulation. The analysis shows that a too small domain leads to an underestimation of the number of wet days and of heavy precipitation days. A more frequent update of the boundary conditions leads to a strong increase in the number of wet days and in the heavy precipitation, generating a remarkable excess of precipitation in the early morning. Moreover, modifications of the model's internal settings can lead to a wrong representation of physical processes related to convective precipitation. Those errors appear only at hourly resolution but they are hidden by the coarser temporal scale. Thus, it is of crucial importance to increase temporal scale together with the spatial scale to evaluate correctly the benefit of convection-permitting scale and thus avoid wrong conclusions.

Several studies proved the added value of convection-permitting scale in NWP mode or for seasonal simulations in climate mode (e.g. Prein et al 2013; Hohenegger et al. 2008), but none was performed on a climate scale.

In this context, 30 years at both a 7 km and a 2.8 km resolution were simulated with CLM to investigate the benefit of convection-permitting scale versus coarser resolution in the representation of the precipitation statistics and of convection. The results show that convection-permitting scale provides a representation of the diurnal cycle of precipitation in good agreement with observations, thus overcoming the well-known limitations of coarser resolution (e.g. Brockhaus et al. 2008). The improvement is linked to a more consistent representation of the atmospheric conditions leading to deep convection thanks to the possibility of switching off the parameterisation of deep convection at this spatial resolution. In addition, hourly statistics at higher resolution are very close to observations. On the other hand, convection-permitting scale simulation shows a problem on daily temporal scale due to the clustering of low intensities precipitation in too large events. Most probably this problem is also present at 7 km but hidden by the underestimates of hourly statistics. In winter, the dominance of large-scale circulation could explain the strong underestimation of dry days affecting both resolutions.

The ability of convection-permitting scale of correctly simulating precipitation on an hourly basis is of crucial importance for erosion models, which are more sensitive to heavy precipitation than to long durations (Antonetti 2013). In fact, 7 km resolution presents insufficiently strong events to generate erosion, while 2.8 km allows reaching a better agreement with observational data from field campaigns, at least for the Weiherbach area (Mrs Kempf, GEOMER GmbH, personal communication, April 17, 2013). Moreover, the possibility to have a correct simulation of the diurnal cycle for the right reasons allows a more sound analysis of the changes in precipitation extremes in the near future.

Feldmann et al. (2012) found that the climate change signal for precipitation over southwestern Germany is highly heterogeneous especially in summer. In this context, it was investigated if and to what extent convection-permitting scale and higher temporal resolution can clarify the climate change signal for this area and provide a better basis for effective adaptation strategies on the national scale. The ECHAM5 model is used as forcing for two RCM simulations of 30 years in the recent past (1971-2000) and near future (2012-2050), at 7 km and 2.8 km resolutions. Besides wet bias, especially relevant in winter for coarser resolution, the change of the forcing causes an underestimation of the higher intensities of hourly precipitation. The different clustering of hourly precipitation on event basis change seems to have a strong impact on erosion modelling, generating underestimation of soil erosion up to 20% (Antonetti 2013; Mrs Kempf, GEOMER GmbH, personal communication, June 27, 2013).

In terms of the climate change signal, the findings are mainly in line with previous literature and thus only the main differences are reported here. The probability distributions for daily and hourly scale provide opposite climate change signals, proving yet again that coarser temporal scale is not sufficient when dealing with high spatial resolution. Event base analysis is found to be a good methodology to bridge the large temporal gap between daily and hourly resolution. In this context, the convection-permitting simulations project a decrease in the number of short events with low intensities (0-10 hours with 0-60 mm/event) and an increase of those lasting between 10 and 20 hours with intensities between 20 and 90 mm/event. Moreover, events longer than 30 hours will reduce substantially in the near future. The total number of events will decrease by 14% in the near future and there will be a strengthening of the dry periods both in frequency and length. In addition, ECHAM5 driven models project an increase in mean precipitation between 2:00 and 14:00 for days with a precipitation above 50 mm, probably linked to

an intensification of large-scale weather patterns. The analysis projects no relevant changes for convective precipitation or even a decrease. In general, convection-permitting and coarser resolutions do not diverge in the sign of the climate change over the investigation area and also the magnitude of the relative changes between past and future is similar between resolutions. Differences between resolutions remain in representation of the diurnal cycle of precipitation, CAPE and cloud cover but they are related to the possibility of switching off the parameterisation of convection at 2.8 km.

Concluding, this doctoral research showed that convection-permitting scale brings important benefit when one is interested in studies on convection, extreme precipitation or detailed spatial representations of precipitation fields as input for further assessment models. Most probably the added value would also appear clearly when investigating the climate change signal if an increase in the hourly precipitation intensities or in convective activities was projected into the future.

8. APPENDIX: First experience with 1 km spatial resolution

Within the KLIWA project "Bodenabtrag durch Wassererosion in Folge von Klimaveränderungen", ECHAM5 driven simulations at 2.8 km resolution were downscaled at 1 km resolution with COSMO-CLM to be used as input for the erosion model LISEM. The purpose of this appendix is to determine the differences between 1 km and 2.8 km resolution in the representation of the precipitation field. Previous research proved that 2.8 km improves the probability distribution of hourly precipitation and the representation of more extreme precipitation events compared to coarser resolution (Fosser et al. 2014; Prein et al. 2013). Moreover, the shape of the precipitation diurnal cycle in summer is closer to the observations thanks to a more consistent representation of the atmospheric fields related with convection (Fosser et al. 2014). The added value of 2.8 km resolution is mainly due to the possibility of switching off the parameterisation of deep convection. Thus, 1 km resolution is also likely to represent correctly the hourly precipitation since the model at this resolution, as at 2.8 km, resolves deep convection. However, not much is known about 1 km resolution. Moreover, evaluating 1 km versus 2.8 km resolution can help understanding the findings of LISEM simulations.

Figure 62 shows in yellow solid (dashed) frame the investigation (simulation) domain for this resolution. The model internal settings are the same as for the simulations at 2.8 km resolution. The comparison between the two resolutions focuses on the investigation area around Weiherbach and it is based on three summers, namely 1985, 1996, and 1997, during which extreme precipitation events occurred. To compare the model outputs on equal terms, the simulations are remapped on a common 2.8 km grid according to the method by Jones (1999).

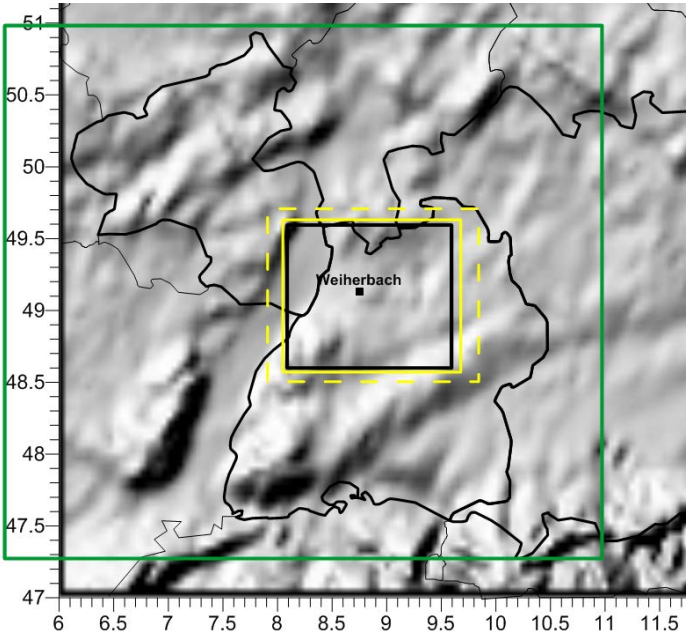

Figure 62: Map of southern part of Germany showing the simulation domain at 2.8 km resolution (green box) and the standard investigation area (black frame). The yellow solid (dashed) frame is the investigation (simulation) domains at 1 km resolution.

For this analysis, observations are not used here; however, Chapter 6.3 validated ECHAM5 driven simulations at 2.8 km resolution against observations for the recent past (1971-2000). The main results are summarised in Table 16. Knowing the failure of 2.8 km compared to observations can help understanding whether the differences between 2.8 km and 1 km are an improvement or not.

Table 16: Summary of the comparison between observations datasets and simulation at 2.8 km driven with ECHAM5 for the recent past (1971-2000) in JJA over the investigation area around Weiherbach.

Bias maps	Overestimation of daily mean precipitation by 15-30% both when all days and only wet days are considered
Percentage of dry days and dry hours	Underestimated by 2% and 6% respectively
Probability distribution on daily basis	strong underestimation of low intensities (below 4 mm/day) overestimation of intermediate and higher intensities (above 15 mm/day)
Probability distribution on hourly base	Underestimation of higher intensities
Precipitation diurnal cycle	correct representation of the shape of the precipitation diurnal cycle but overestimation of the amplitude

Figure 63 shows the spatial distribution of daily mean precipitation in summer at 1 km (left) and 2.8 km (right). When all days (Figure 63 top) are considered, 1 km resolution reduces mean precipitation uniformly over the investigation area, while the reduction concentrates mainly over the Black Forest if selecting only wet days (Figure 63 bottom). Since the 2.8 km resolution tends to overestimate precipitation by 15-30% compared to the HYRAS dataset (Table 16), the above-mentioned reduction at 1 km resolution can be seen as an improvement compared to 2.8 km resolution.

Table 17: Percentage of dry days and dry hours for the model simulations in summer (top row).

Percentage of	**1 km**	**2.8 km**
Dry days	67 %	63 %
Dry hours	88 %	87 %

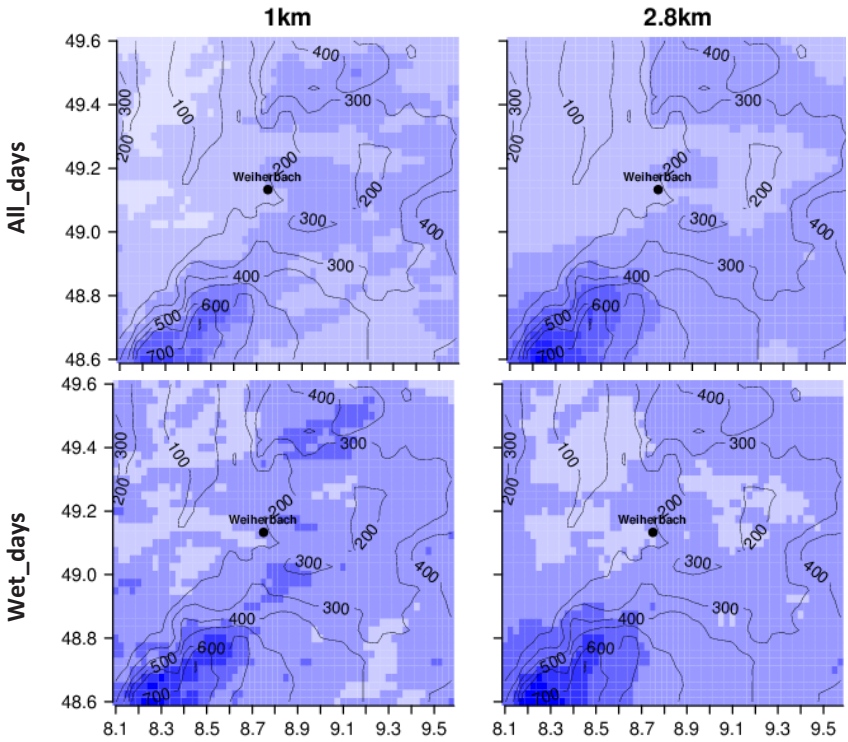

Figure 63: Spatial distribution of summer daily mean precipitation for 1 km (left) and 2.8 km resolution (right), when all days (top) and only wet days (bottom) are considered. The contour lines represent the orography of the area.

The percentage of dry days at 1 km is ~6% more than for the simulation at 2.8 km, which in turn is underestmating dry days by 2% compard to HYRAS (Table 17). The probability distribution of daily intensities in Figure 64 shows that 1 km compared to 2.8 km resolution has higher lower intensities (below 3 mm/day) and lower medium intensities between 3 and ~15 mm/day. Precipitation above the latter threshold has higher probablitity at 1 km than at 2.8 km resolution. Thus, 1 km resolutions improve the

representations of daily precipitation below 15 mm/day while it overestimates the intensities above this threshold (see Table 16).

Compared to observations, the 2.8 km simulation represented well most hourly precipitation, but it underestimated higher intensities (Table 16). The probability distributions on an hourly basis for 1 km and 2.8 km resolutions are very similar (not shown). The difference between them that is likely to affect erosion modelling the most concerns the higher intensities. Those are underestimated by 1 km resolution in comparison with 2.8 km resolution and thus with observations.

Lower maximum intensities at 1 km, together with an increase in the percentage of dry hours, lead to a reduction in the amplitude of the diurnal cycle of precipitation (Figure 65). The shape of the precipitation diurnal cycle is retained at higher resolution since both resolutions do not parameterise deep convection. This is crucial for erosion modelling as it guarantees that precipitation occurs on average at the right time.

Concluding, 1 km resolution generally agrees very well with 2.8 km resolution especially in terms of timing of the precipitation. Nevertheless, very higher spatial resolution tends to underestimate higher precipitation intensities on an hourly base compared to 2.8 km resolution and this could lead to an underestimation of soil erosion.

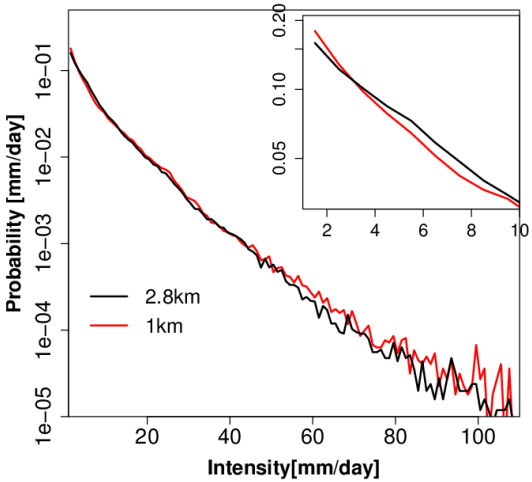

Figure 64: Probability distribution of summer daily precipitation. Note the logarithmic vertical axis.

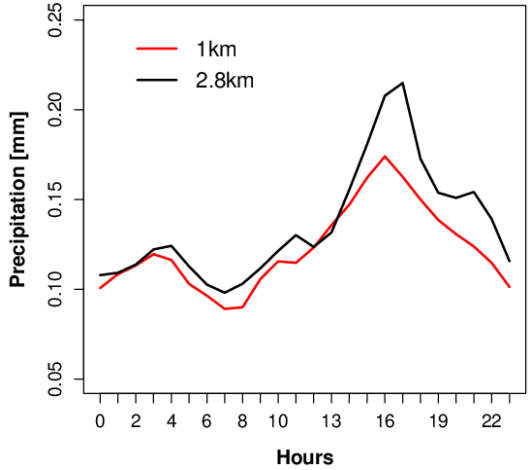

Figure 65: Diurnal cycle of summer precipitation for 1 km (light blue) and 2.8 km (pink).

Acronyms

CAPE	Convective Available Potential Energy
CIN	Convective Inhibition
COSMO-CLM (abbreviated in CLM)	COnsortium for Small scale Modelling model—in CLimate Model
DJF	Winter season (i.e. December-January-February)
DWD	Deutscher WetterDienst (German weather service)
EL	Equilibrium Level
GCMs	Global Circulation Models
IPCC	Intergovernmental Panel on Climate Change
JJA	Summer season (i.e. June-July-August)
LCL	Lifted Condensation Level
LFC	Level of Free Convection
LST	Local Standard Time
NWP	Numerical Weather Prediction
RCMs	Regional climate models
REGNIE	REGionalisierung der NIEderschlags-höhen (Eng. regionalised precipitation amount)

Bibliography

Abdullah M (1990) On a Robust Correlation Coefficient. J Roy Stat Soc D-Stat 39: 455–460

Alexandru A, de Elia R, Laprise R (2007) Internal Variability in Regional Climate Downscaling at the Seasonal Scale. Mon. Weather Rev. 135: 3221–3238. doi: 10.1175/MWR3456.1

Antonetti M (2013) Analysis of climate change impact on runoff and soil erosion in a small rural catchment. MSc thesis, Karlsruhe Intitute of Technology (KIT)

Bachner S, Kapala A, Simmer C (2008) Evaluation of daily precipitation characteristics in the CLM and their sensitivity to parameterizations. Meteorol. Z. 17: 407–419. doi: 10.1127/0941-2948/2008/0300

Baldauf M, Seifert A, Förstner J, Majewski D, Raschendorfer M, Reinhardt T (2011) Operational convective-scale numerical weather prediction with the COSMO model: description and sensitivities. Mon. Weather Rev. 139: 3887–3905. doi: 10.1175/MWR-D-10-05013.1

Bartels H, Dietzer B, Malitz G, Albrecht FM, Guttenberger J (2005) KOSTRA-DWD-2000 Starkniederschlagshöhen für Deutschland (1951–2000). Deutscher Wetterdienst, Offenbach

Barthlott C, Corsmeier U, Meißner C, Braun F, Kottmeier K (2006) The influence of mesoscale circulation systems on triggering convective cells over complex terrain. Atmos. Res. 81: 150–175. doi: 10.1016/j.atmosres.2005.11.010

Barthlott C, Schipper JW, Kalthoff N, Adler B, Kottmeier K, Blyth A, Mobbs S (2010) Model representation of boundary-layer convergence triggering deep convection over complex terrain: A case study from COPS. Atmos. Res. 95: 172–185. doi: 10.1016/j.atmosres.2009.09.010

Bechtold P, Chaboureau J-P, Beljaars A, Betts AK, Köhler M, Miller M, Redelsperger J-L (2004) The simulation of the diurnal cycle of convective precipitation over land in a global model. Q. J. Roy. Meteorol. Soc. 130: 3119–3137. doi: 10.1256/qj.03.103

Berg P, Haerter JO (2013) Unexpected increase in precipitation intensity with temperature — A result of mixing of precipitation types? Atmos. Res. 119: 56–61. doi: 10.1016/j.atmosres.2011.05.012

Berg P, Moseley C, Haerter JO (2013) Strong increase in convective precipitation in response to higher temperatures. Nat. Geosci. 6: 181–185. doi: 10.1038/ngeo1731

Berg P, Wagner S, Kunstmann H, Schädler G (2012) High resolution regional climate model simulations for Germany: part I—validation. Clim. Dynami. 40: 401–414. doi: 10.1007/s00382-012-1508-8

Betts AK, Ball JH, Beljaars ACM, Miller MJ, Viterbo PA (1996) The land surface-atmosphere interaction: A review based on observational and global modeling perspectives. J. Geophys. Resi. 101(D3): 7209-7225. doi: 10.1029/95JD02135

Blackadar AK (1962) The vertical distribution of wind and turbolent exchaneg in a neutral atmosphere. J. Geophys. Resi. 62: 3095–3102.

Boberg F, Berg P, Thejll P, Gutowski WJ, Christensen JH (2010) Improved confidence in climate change projections of precipitation further evaluated using daily statistics from ENSEMBLES models. Clim. Dynami. 35: 1509–1520. doi: 10.1007/s00382-009-0683-8

Boberg F, Berg P, Thejll P, Gutowski WJ, Christensen JH (2009) Improved confidence in climate change projections of precipitation evaluated using daily statistics from the PRUDENCE ensemble. Clim. Dynami. 32: 1097–1106. doi: 10.1007/s00382-008-0446-y

Brockhaus P, Lüthi D, Schär C (2008) Aspects of the diurnal cycle in a regional climate model. Meteorol. Z. 17: 433–443. doi: 10.1127/0941-2948/2008/0316

Brommundt J, Bárdossy A (2007) Advances in Geosciences Spatial correlation of radar and gauge precipitation data in high temporal resolution. Adv. Geosci. 10: 103–109. doi:10.5194/adgeo-10-103-2007

Brooks HE, Doswell CA, Wicker LJ (1993) STORMTIPE: A Forecasting Experiment Using a Three-Dimensional Cloud Model. Weather Forecast 8: 352–362. doi: 10.1175/1520-0434(1993)008<0352:SAFEUA>2.0.CO;2

Caya D, Biner S (2004) Internal variability of RCM simulations over an annual cycle. Clim. Dynami. 22: 33–46. doi: 10.1007/s00382-003-0360-2

Christensen JH, Christensen OB (2007) A summary of the PRUDENCE model projections of changes in European climate by the end of this century. Climatic Change 81: 7–30. doi: 10.1007/s10584-006-9210-7

Christensen JH, Hewitson B, Busuioc A, Chen A, Gao X, Held I, Jones R, Kolli RK, Kwon W-T, Laprise R, Magaña Rueda V, Mearns L, Menéndez CG, Räisänen J, Rinke A, Sarr A, Whetton P (2007) Regional Climate Projections. In: Climate Change 2007: The Physical Science Basis. Contribution of Working Group I to the Fourth Assessment Report of the Intergovernmental Panel on Climate Change [Solomon, S., D. Qin, M. Manning, Z. Chen, M. Marquis, K.B. Averyt, M. Tignor and H.L. Miller (eds.)]. Cambridge University Press, Cambridge, United Kingdom and New York, NY, USA

Colby FP (1984) Convective Inhibition as a Predictor of Convection during AVE-SESAME II. Mon. Weather Rev. 112: 2239–2252

Crook NA (1996) Sensitivity of Moist Convection Forced by Boundary Layer Processes to Low-Level Thermodynamic Fields. Mon. Weather Rev. 124: 1767–1785. doi: 10.1175/1520-0493(1996)124<1767:SOMCFB>2.0.CO;2

Dai A (2006) Precipitation Characteristics in Eighteen Coupled Climate Models. J. Climate 19: 4605–4630. doi: 10.1175/JCLI3884.1

Dai A, Trenberth K (2004) The diurnal cycle and its depiction in the Community Climate System Model. J. Climate 17: 930–951. doi: 10.1175/1520-0442(2004)017<0930:TDCAID>2.0.CO;2

Denis B, Laprise R, Caya D (2003) Sensitivity of a regional climate model to the resolution of the lateral boundary conditions. Clim. Dynami. 20: 107–126. doi: 10.1007/s00382-002-0264-6

Déqué M, Jones RG, Wild M, Giorgi F, Christensen JH, Hassell DC, Vidale PL, Rockel B, Jacob D, Kjellström E, de Castro M, Kucharski F, van den Hurk B (2005) Global high resolution versus Limited Area Model climate change projections over Europe: quantifying confidence level from PRUDENCE results. Clim. Dynami. 25: 653–670. doi: 10.1007/s00382-005-0052-1

Déqué M, Rowell DP, Lüthi D, Giorgi F, Christensen JH, Rockel B, Jacob D, Kjellström E, de Castro M, van den Hurk B (2007) An intercomparison of regional climate simulations for Europe: assessing uncertainties in model projections. Climatic Change 81: 53–70. doi: 10.1007/s10584-006-9228-x

Dickinson R (1984) Climate processes and climate sensitivity. In: Climate processes and climate sensitivity [Hansen JE, Takahashi T (eds.]), Geophysical Monograph vol 29. American Geophysical Union, Washington DC, USA

Dickinson RE, Errico RM, Giorgi F, Bates GT (1988) CAR Feasibility Study on: Modeling of historic, prehistoric and future climates of the great basin. Final Report to USGS/NNWSI

Dietzer B (2003) Berechnung von Gebietsniederschlags höhen nach dem Verfahren REGNIE. Deutscher Wetterdienst, Offenbach

Doms G (2011) Consortium for Small-Scale Modelling A Description of the Nonhydrostatic Regional COSMO-Model Part I: Dynamics and Numerics. Deutscher Wetterdienst, Offenbach

Doms G, Förstner J, Heise E, Herzog H-J, Mironov D, Raschendorfer M, Reinhardt T, Ritter B, Schrodin R, Schulz J-P, Vogel G (2011) A description of the nonhydrostatic regional COSMO model. Part II: Physical Parameterization. Deutscher Wetterdienst, Offenbach

Doswell CA (1987) The Distinction between Large-Scale and Mesoscale Contribution to Severe Convection: A Case Study Example. Weather Forecast 2: 3–16. doi: 10.1175/1520-0434(1987)002<0003:TDBLSA>2.0.CO;2

Doswell CA, Rasmussen EN (1994) The Effect of Neglecting the Virtual Temperature Correction on CAPE Calculations. Weather Forecast 9: 625–629. doi: 10.1175/1520-0434(1994)009<0625:TEONTV>2.0.CO;2

Eltahir EAB (1998) A Soil Moisture-Rainfall Feedback Mechanism: 1. Theory and observations. Water Resour Res. 34: 765–776. doi: 10.1029/97WR03499

Emanuel KA (1994) Atmospheric Convection. Oxford University Press

Favis-Mortlock DT, Savabi MR (1996) Shifts in rates and spatial distributions of soil erosion and deposition under climate change. In: Advances in hillslope processes: voleme 1 [Anderson MG, Brooks S. (eds)]. Wiley, Chichester, UK

Feldmann H, Früh B, Schädler G, Panitz H-J, Keuler K, Jacob D, Lorenz P (2008) Evaluation of the precipitation for South-western Germany from high resolution simulations with regional climate models. Meteorol. Z. 17: 455–465. doi: 10.1127/0941-2948/2008/0295

Feldmann H, Schädler G, Panitz H-J, Kottmeier C (2012) Near future changes of extreme precipitation over complex terrain in Central Europe derived from high resolution RCM ensemble simulations. Int. J. Climatol. 33: 1964-1977. doi: 10.1002/joc.3564

Fosser G, Khodayar S, Berg P (2014) Benefit of cloud-resolving climate model simulations in the representation of convective precipitation. Clim. Dynami.

Früh B, Feldmann H, Panitz H, Schädler G, Jacob D, Lorenz P, Keuler K (2010) Determination of precipitation return values in complex terrain and their evaluation. J. Climate 23: 2257–2274. doi: http://dx.doi.org/10.1175/2009JCLI2685.1

Gebhardt C, Theis SE, Paulat M, Ben Bouallègue Z (2011) Uncertainties in COSMO-DE precipitation forecasts introduced by model perturbations and variation of lateral boundaries. Atmos. Res. 100: 168–177. doi: 10.1016/j.atmosres.2010.12.008

Giorgi F (2006) Regional climate modeling: Status and perspectives. J. Phys. IV 139 :101–118. doi: 10.1051/jp4: 2006139008

Giorgi F, Bi X, Pal J (2004) Mean, interannual variability and trends in a regional climate change experiment over Europe. II: climate change scenarios (2071-2100). Clim. Dynami. 23: 839–858. doi: 10.1007/s00382-004-0467-0

Giorgi F, Marinucci MR, Bates GT (1993) Development of a Second-Generation Regional Climate Model (RegCM2). Part I: Boundary-Layer and Radiative Transfer Processes. Mon. Weather Rev. 121: 2794–2813. doi: 10.1175/1520-0493(1993)121<2794:DOASGR>2.0.CO;2

Giorgi F, Mearns LO (1999) Introduction to special section: Regional Climate Modeling Revisited. J. Geophys. Resi. 104: 6335-6352. doi: 10.1029/98JD02072

Grell GA, Schade L, Knoche R, Pfeiffer A, Egger J (2000) Nonhydrostatic climate simulations of precipitation over complex terrain. J. Geophys. Resi. 105(D24): 29595-29608. doi: 10.1029/2000JD900445

Haerter JO, Berg P (2009) Unexpected rise in extreme precipitation caused by a shift in rain type? Nat. Geosci. 2: 372–373. doi: 10.1038/ngeo523

Haerter JO, Berg P, Hagemann S (2010) Heavy rain intensity distributions on varying time scales and at different temperatures. J. Geophys. Resi. 115: D17102. doi: 10.1029/2009JD013384

Herrera S, Fita L, Fernández J, Gutiérrez JM (2010) Evaluation of the mean and extreme precipitation regimes from the ENSEMBLES regional climate multimodel simulations over Spain. J. Geophys. Resi. 115: D21117. doi: 10.1029/2010JD013936

Hewitt C (2005) The ENSEMBLES project: providing ensemble- based predictions of climate changes and their impacts. EGGS Newsl 22–25.

Hillel DJ (1980) Applications of soil physics. Academic Press, New York.

Hohenegger C, Brockhaus P, Bretherton CS, Schär C (2009) The Soil Moisture–Precipitation Feedback in Simulations with Explicit and Parameterized Convection. J. Climate 22: 5003–5020. doi: 10.1175/2009JCLI2604.1

Hohenegger C, Brockhaus P, Schär C (2008) Towards climate simulations at cloud-resolving scales. Meteorol. Z. 17: 383–394. doi: 10.1127/0941-2948/2008/0303

Houze RAJ (1993) Cloud Dynamics. Academic Press

IPCC, 2013: Summary for Policymakers. In: Climate Change 2013: The Physical Science Basis. Contribution of Working Group I to the Fifth Assessment Report of the Intergovernmental Panel on Climate Change [Stocker, T.F., D. Qin, G.-K. Plattner, M. Tignor, S. K. Allen, J. Boschung, A. Nauels, Y. Xia, V. Bex and P.M. Midgley (eds.)]. Cambridge University Press, Cambridge, United Kingdom and New York, NY, USA.

Jacob D, Podzun R (1997) Sensitivity studies with the regional climate model REMO. Meteorol. Atmos. Phys. 63: 119–129. doi: 10.1007/BF01025368

Jaeger EB, Anders I, Lüthi D, Rockel B, Schär C, Seneviratne SI (2008) Analysis of ERA40-driven CLM simulations for Europe. Meteorol. Z. 17: 349–367. doi: 10.1127/0941-2948/2008/0301

Jones PW (1999) First- and Second-Order Conservative Remapping Schemes for Grids in Spherical Coordinates. Mon. Weather Rev. 127: 2204–2210. doi: 10.1175/1520-0493(1999)127<2204:FASOCR>2.0.CO;2

Jones RG, Murphy JM, Noguer M (1995) Simulation of climate change over europe using a nested regional-climate model. I: Assessment of control climate, including sensitivity to location of lateral boundaries. Q. J. Roy. Meteor. Soc. 121: 1413–1449. doi: 10.1002/qj.49712152610

Kalthoff N, Adler B, Barthlott C, Corsmeier U, Mobbs S, Crewell S, Träumner K, Kottmeier C, Wieser A, Smith V, Di Girolamo P (2009) The impact of convergence zones on the initiation of deep convection: A case study from COPS. Atmos. Res. 93: 680–694. doi: 10.1016/j.atmosres.2009.02.010

Kalthoff N, Horlacher V, Corsmeier U, Volz-Thomas A, Kolahgar B, Geiß H, Möllmann-Coers M, Knaps A (2000) Influence of valley winds on transport and dispersion of airborne pollutants in the Freiburg-Schauinsland area. J. Geophys. Resi. 105 (D1): 1585-1597. doi: 10.1029/1999JD900999

Kendall MG (1962) Rank Correlation Methods, 3rd ed. Hafner Publishing Company, New York

Kessler E (1969) On the Distribution and Continuity of water substance in the atmospheric circulations. American Meteorological Society, Boston

Khodayar S, Kalthoff N, Schädler G (2013) Impact of soil moisture variability in seasonal climatic simulations of convective precipitation over a complex terrain. Part I: Validation, local feedbacks and realistic initialization. Meteorol. Z., 22: 507-526. doi: 10.1127/0941-2948/2013/0431

Khodayar S, Kalthoff N, Wickert J, Corsmeier U, Morcrette CJ, Kottmeier C (2010) The increase of spatial data resolution for the detection of the initiation of convection. A case study from CSIP. Meteorol. Z. 19: 179–198. doi: 10.1127/0941-2948/2010/0439

Klein Tank AMG, Zwiers FW, Zhang X (2009) Guidelines on Analysis of extremes in a changing climate in support of informed decisions for adaptation, Climate Data and Monitoring WCDMP-No. 72, WMO-TD No. 1500. 56 pp

Koßmann M, Fiedler F (2000) Diurnal momentum budget analysis of thermally induced slope winds. Meteorol. Atmos. Phys. 75: 195–215. doi: 10.1007/s007030070004

Koster RD, Suarez MJ (2003) Impact of Land Surface Initialization on Seasonal Precipitation and Temperature Prediction. J. Hydrometeorol. 4: 408–423. doi: 10.1175/1525-7541(2003)4<408:IOLSIO>2.0.CO;2

Kottmeier C, Kalthoff N, Barthlott C, Corsmeier U, van Baelen J, Behrendt A, Behrendt R, Blyth A, Coulter R, Crewell S, di Girolamo P, Dorninger M, Flamant C, Foken T, Hagen M, Hauck C, Höller H, Konow H, Kunz M, Mahlke H, Mobbs S, Richard E, Steinacker R, Weckwerth T, Wieser A, Wulfmeyer V (2008) Mechanisms initiating deep convection over complex terrain during COPS. Meteorol. Z. 17: 931–948. doi: 10.1127/0941-2948/2008/0348

Kunz M, Sander J, Kottmeier C (2009) Recent trends of thunderstorm and hailstorm frequency and their relation to atmospheric characteristics in southwest Germany. Int. J. Climatol. 29: 2283–2297. doi: 10.1002/joc.1865

Langhans W, Schmidli J, Fuhrer O, Bieri S, Schär C (2013) Long-term simulations of thermally-driven flows and orographic convection at convection-parameterizing and cloud-resolving resolutions. J. Appl. Meteor. Climatol. 52: 1490-1510. doi: 10.1175/JAMC-D-12-0167.1

Lean HW, Clark PA, Dixon M, Roberts NM, Fitch A, Forbes R, Halliwell C (2008) Characteristics of High-Resolution Versions of the Met Office Unified Model

for Forecasting Convection over the United Kingdom. Mon. Weather Rev. 136: 3408–3424. doi: 10.1175/2008MWR2332.1

Lenderink G, van Meijgaard E (2008) Increase in hourly precipitation extremes beyond expectations from temperature changes. Nat. Geosci. 1: 511–514. doi: 10.1038/ngeo262

Van der Linden P, Mitchell J (2009) ENSEMBLES: Climate Change and Its Impacts: Summary of research and results from the ENSEMBLES project. Met Office Hadley Centre, Exeter, UK

Mass CF, Ovens D, Westrick K, Colle BA (2002) Does Increasing Horizontal Resolution Produce More Skillful Forecasts? B. Am. Meteorol. Soc. 83: 407–430. doi: 10.1175/1520-0477(2002)083<0407:DIHRPM>2.3.CO;2

McGregor JL (1997) Regional climate modelling. Meteorol. Atmos. Phys. 63: 105–117. doi: 10.1007/BF01025367

Meißner C (2008) High-resolution sensitivity studies with the regional climate model COSMO-CLM. PhD thesis, Karlsruhe Intitute of Technology (KIT)

Meißner C, Schädler G, Panitz H-J, Feldmann H, Kottmeier C (2009) High-resolution sensitivity studies with the regional climate model COSMO-CLM. Meteorol. Z. 18: 543–557. doi: 10.1127/0941-2948/2009/0400

Meißner C, Kalthoff N, Kunz M, Adrian G (2007) Initiation of shallow convection in the Black Forest mountains. Atmos. Res. 86: 42–60. doi: 10.1016/j.atmosres.2007.03.003

Michael A, Schmidt J, Enke W, Deutschländer Th, Malitz G(2005) Impact of expected increase in precipitation intensities on soil loss—results of comparative model simulations. Catena 61: 155–164. doi: 10.1016/j.catena.2005.03.002

Miura H, Satoh M, Tomita H, Nasuno T, Iga S (2007) A short-duration global cloud-resolving simulation with a realistic land and sea distribution. Geophys. Res. Lett. 34: L02804. doi: 10.1029/2006GL027448

Moberg A, Jones PD (2004) Regional climate model simulations of daily maximum and minimum near-surface temperatures across Europe compared with observed station data 1961-1990. Clim. Dynami. 23: 695–715. doi: 10.1007/s00382-004-0464-3

Moncrieff MW, Miller MJ (1976) The dynamics and simulation of tropical cumulonimbus and squall lines. Q. J. Roy. Meteor. Soc. 373–394.

Nakicenovic N, Alcamo J, Davis G, de Vries B, Fenhann J, Gaffin S, Gregory K, Grübler A, Yong Jung T, Kram T, Lebre La Rovere E, Michaelis L, Mori S, Morita T, Pepper W, Pitcher H, Price L, Riahi K, Roehrl A, Rogner H-H, Sankovski A, Schlesinger M, Shukla P, Smith S, Swart R, van Rooijen S, Victor N, Dadi Z (2000) Special Report on Emissions Scenarios: A Special Report of Working Group III of the Intergovernmental Panel on Climate Change, Cambridge University Press,

Cambridge, U.K., available online at: http://www.grida.no/climate/ipcc/emission/index.htm

Pal JS, Small EE, Eltahir EAB (2000) Simulation of regional-scale water and energy budgets: Representation of subgrid cloud and precipitation processes within RegCM. J. Geophys. Resi. 105(D24): 29579–29594. doi: 10.1029/2000JD900415

Pan Z, Arritt RW, Gutowski WJ, Takle ES (2001) Soil moisture in a regional climate model: Simulation and projection. Geophys. Res. Lett. 28: 2947–2950. doi: 10.1029/2000GL012172

Pearson K (1920) Notes on the History of Correlation. Biometrika 13(1): 25–45

Perry M, Hollis D (2005) The generation of monthly gridded datasets for a range of climatic variables over the UK. Int. J. Climatol. 25: 1041–1054. doi: 10.1002/joc.1161

Philipona R (2005) Anthropogenic greenhouse forcing and strong water vapor feedback increase temperature in Europe. Geophys. Res. Lett. 32: L19809. doi: 10.1029/2005GL023624

Photiadou CS, Weerts AH, van den Hurk BJJM (2011) Evaluation of two precipitation data sets for the Rhine River using streamflow simulations. Hydrol. Earth Syst. Sci. 15: 3355–3366. doi: 10.5194/hess-15-3355-2011

Plate E, Zehe E (2008) Hydrologie und Stoffdynamik kleiner Einzugsgebiete. Prozesse und Modelle. Schweizerbartsche Verlagsbuchhandlung, Germany

Prein a. F, Gobiet A, Suklitsch M, Truhetz H, Awam NK, Keuler K, Georgievski G (2013) Added value of convection permitting seasonal simulations. Clim. Dynami. 41: 2655-2677. doi: 10.1007/s00382-013-1744-6

Raschendorfer M (2001) The new turbulence parametrization of LM. COSMO-Newsletter 1: 89–97

Rauthe M, Steiner H, Riediger U, Mazurkiewicz A, Gratzki A (2013) A Central European precipitation climatology – Part I: Generation and validation of a high-resolution gridded daily data set (HYRAS). Meteorol. Z., 22: 235-256. doi:10.1127/0941-2948/2013/0436

Reichler T, Kim J (2008) How Well Do Coupled Models Simulate Today's Climate? B. Am. Meteorol. Soc. 89: 303–311. doi: 10.1175/BAMS-89-3-303

Richard E, Buzzi A, Zängl G (2007) Quantitative precipitation forecasting in the Alps: The advances achieved by the Mesoscale Alpine Programme. Q. J. Roy. Meteor. Soc. 133: 831–846. doi: 10.1002/qj.65

Ritter B, Geleyn J-F (1992) A Comprehensive Radiation Scheme for Numerical Weather Prediction Models with Potential Applications in Climate Simulations. Mon. Weather Rev. 120: 303–325. doi: 10.1175/1520-0493(1992)120<0303:ACRSFN>2.0.CO;2

Roberts NM, Lean HW (2008) Scale-Selective Verification of Rainfall Accumulations from High-Resolution Forecasts of Convective Events. Mon. Weather Rev. 136: 78–97. doi: 10.1175/2007MWR2123.1

Roeckner E, Bäuml G, Bonaventura L, Brokopf R, Esch M, Giorgetta M, Hagemann S, Kirchner I, Kornblueh L, Manzini E, Rhodin A, Schlese U, Schulzweida U, Tompkins A (2003) The atmospheric general circulation model ECHM5. Part 1: Model description, Technical report No 349, Max Planck Institute for Meteorology, Hamburg

Roeckner E, Lautenschlager M, Schneider H (2006) IPCC-AR4 MPI-ECHAM5_T63L31 MPI-OM_GR1.5L40 20C3M run no.1: atmosphere 6 HOUR values MPImet/MaD Germany. World Data Cent Clim. doi: 10.1594/WDCC/EH5-T63L31_OM-GR1.5L40_20C_1_6H

De Roo APJ, Wesseling CG, Ritsema CJ (1996) LISEM: a single-event physically based hydrological and soil erosion model for drainage basins. i: theory, input and output. Hydrol Process 10: 1107–1117. doi: 10.1002/(SICI)1099-1085(199608)10:8<1107::AID-HYP415>3.0.CO;2-4

Schär C, Lüthi D, Beyerle U, Heise E (1999) The Soil–Precipitation Feedback: A Process Study with a Regional Climate Model. J. Climate 12: 722–741. doi: 10.1175/1520-0442(1999)012<0722:TSPFAP>2.0.CO;2

Schättler G, Doms G, Schraff C (2013) Consortium for Small-Scale Modelling A Description of the Nonhydrostatic Regional COSMO-Model Part VII: User's Guide. Deutscher Wetterdienst, Offenbach

Scherer U (2008) Prozessbasierte Modellierung der Bodenerosion in einer Lösslandschaft, PhD thesis, Karlsruhe Intitute of Technology (KIT)

Schrodin R, Heise E (2001) The multi-layer version of the DWD soil model TERRA-LM. COSMO Technical Report 2. Deutscher Wetterdienst, Offenbach

Schwartz CS, Kain JS, Weiss SJ, Xue M, Bright DR, Kong F, Thomas KW, Levit JJ, Coniglio MC (2009) Next-Day Convection-Allowing WRF Model Guidance: A Second Look at 2-km versus 4-km Grid Spacing. Mon. Weather Rev. 137: 3351–3372. doi: 10.1175/2009MWR2924.1

Schwitalla T, Bauer H-S, Wulfmeyer V, Zängl G (2008) Systematic errors of QPF in low-mountain regions as revealed by MM5 simulations. Meteorol. Z. 17: 903–919. doi: 10.1127/0941-2948/2008/0338

Seneviratne S, Pal J, Eltahir E, Schär C (2002) Summer dryness in a warmer climate: a process study with a regional climate model. Clim. Dynami. 20: 69–85. doi: 10.1007/s00382-002-0258-4

Seth A, Giorgi F (1998) The Effects of Domain Choice on Summer Precipitation Simulation and Sensitivity in a Regional Climate Model. J. Climate 11: 2698–2712. doi: 10.1175/1520-0442(1998)011<2698:TEODCO>2.0.CO;2

Smith RK (1997) The Physics and Parameterization of Moist Atmospheric Convection. Kluwer Academic Publishers, Dordrecht, the Netherlands

Sommer R, Sommer B (2002) A Practical Guide to Behavioral Research: Tools and Techniques, 5th ed. Oxford University Press, New York

Steppeler J, Doms G, Schättler U, Bitzer HW, Gassmann A, Damrath U, Gregoric G (2003) Meso-gamma scale forecasts using the nonhydrostatic model LM. Meteorol. Atmos. Phys. 82: 75–96. doi: 10.1007/s00703-001-0592-9

Suklitsch M, Gobiet A, Leuprecht A, Frei C (2008) High Resolution Sensitivity Studies with the Regional Climate Model CCLM in the Alpine Region. Meteorol. Z. 17: 467–476. doi: 10.1127/0941-2948/2008/0308

Tiedtke M (1989) A Comprehensive Mass Flux Scheme for Cumulus Parameterization in Large-Scale Models. Mon. Weather Rev. 117: 1779–1800. doi: 10.1175/1520-0493(1989)117<1779:ACMFSF>2.0.CO;2

Trenberth K, Dai A, Rasmussen R, Parsons D (2003) The changing character of precipitation. B. Am. Meteorol. Soc. 84: 1205–1217. doi: 10.1175/BAMS-84-9-1205

Uppala SM, Kållberg PW, Simmons a. J, Andrae U, Bechtold VDC, Fiorino M, Gibson JK, Haseler J, Hernandez A, Kelly GA, Li X, Onogi K, Saarinen S, Sokka N, Allan RP, Andersson E, Arpe K, Balmaseda MA, Beljaars ACM, Berg LVD, Bidlot J, Bormann N, Caires S, Chevallier F, Dethof A, Dragosavac M, Fisher M, Fuentes M, Hagemann S, Hólm E, Hoskins BJ, Isaksen L, Janssen PAEM, Jenne R, Mcnally AP, Mahfouf J-F, Morcrette J-J, Rayner N A, Saunders RW, Simon P, Sterl A, Trenberth KE, Untch A, Vasiljevic D, Viterbo P, Woollen J (2005) The ERA-40 re-analysis. Q. J. Roy. Meteor. Soc. 131: 2961–3012. doi: 10.1256/qj.04.176

Vidale PL, Lüthi D, Frei C, Seneviratne S, Schär C (2003) Predictability and uncertainty in a regional climate model. J. Geophys. Resi. 108: 4586. doi: 10.1029/2002JD002810

Wagner S, Berg P, Schädler G, Kunstmann H (2012) High resolution regional climate model simulations for Germany: Part II—projected climate changes. Clim. Dynami. 40: 415–427. doi: 10.1007/s00382-012-1510-1

Weusthoff T, Ament F, Arpagaus M, Rotach MW (2010) Assessing the Benefits of Convection-Permitting Models by Neighborhood Verification: Examples from MAP D-PHASE. Mon. Weather Rev. 138: 3418–3433. doi: 10.1175/2010MWR3380.1

Wicker LJ, Skamarock WC (2002) Time-Splitting Methods for Elastic Models Using Forward Time Schemes. Mon. Weather Rev. 130: 2088–2097. doi: 10.1175/1520-0493(2002)130<2088:TSMFEM>2.0.CO;2

Widmann M, Bretherton CS (2000) Validation of Mesoscale Precipitation in the NCEP Reanalysis Using a New Gridcell Dataset for the Northwestern United States. J.

Climate 13: 1936–1950. doi: 10.1175/1520-0442(2000)013<1936:VOMPIT>2.0.CO;2

Will A, Woldt M (2009) Comparison of COSMO-CLM results with CM-SAF products: radiation components ToA, at the surface and cloud properties. Technical Report IOP VS Study 16, Climate Monitoring Satellite Application Facility (CMSAF) at DWD, Offenbach,

Wu W, Dickinson RE (2004) Time Scales of Layered Soil Moisture Memory in the Context of Land–Atmosphere Interaction. J. Climate 17: 2752–2764. doi: 10.1175/1520-0442(2004)017<2752:TSOLSM>2.0.CO;2

Wulfmeyer V, Behrendt A, Bauer H-S, Kottmeier C, Corsmeier U, Blyth A, Craig G, Schumann U, Hagen M, Crewell S, di Girolamo P, Flamant C, Miller M, Montani A, Mobbs S, Richard E, Rotach MW, Arpagaus M, Russchenberg H, Schlüssel P, König M, Gärtner V, Steinacker R, Dorninger M, Turner DD, Weckwerth T, Hense A, Simmer C (2008) RESEARCH CAMPAIGN: The Convective and Orographically Induced Precipitation Study. B. Am. Meteorol. Soc. 89: 1477–1486. doi: 10.1175/2008BAMS2367.1

Yanai M, Esbensen S, Chu J-H (1973) Determination of Bulk Properties of Tropical Cloud Clusters from Large-Scale Heat and Moisture Budgets. J. Atmos. Sci. 30: 611–627. doi: 10.1175/1520-0469(1973)030<0611:DOBPOT>2.0.CO;2

Yang G, Slingo J (2001) The diurnal cycle in the tropics. Mon. Weather Rev. 129: 784–801. doi: 10.1175/1520-0493(2001)129<0784:TDCITT>2.0.CO;2

Zehe E, Maurer T, Ihringer J, Plate E (2001) Modeling water flow and mass transport in a loess catchment. Phys. Chem. Earth, Part B Hydrol Ocean Atmos 26: 487–507. doi: 10.1016/S1464-1909(01)00041-7

Zhang X, Alexander L, Hegerl GC, Jones P, Tank AK, Peterson TC, Trewin B, Zwiers FW (2011) Indices for monitoring changes in extremes based on daily temperature and precipitation data. WIREs Clim. Change 2: 851–870. doi: 10.1002/wcc.147

Acknowledgements

First of all, I would like to thank my son Pietro who always helps me in setting the right priorities.

Another special thank goes my Guru, because he is The Guru and everybody needs one. Many, many thanks to Samiro for sharing with me some of her knowledge about convection and especially for being a friend.

I would like especially to acknowledge Prof. Dr. Zehe for his support and availability during these three years. I would also like to thank very much Prof. Dr. Kottmeier.

I acknowledge funding, within the KLIWA-project "Bodenabtrag durch Wassererosion in Folge von Klimaveränderungen", from Bavarian State Ministry of the Environment and Public Health, Ministry of Economics, Climate Protection, Energy and Regional Planning of the German State Rheinland-Pfalz and Ministry of the Environment, Climate Protection and the Energy Sector Baden-Württemberg. I also acknowledge the GRACE program for the additional financial support.

The author is grateful to the German Weather Service (DWD) and to the State Institute for Environmental Protection Baden-Württemberg (LUBW) for data supply and cooperation.

Many thanks to my colleagues and friends who made me laugh even when I was not feeling like it!

A special Grazie goes to my family for their unconditional support and because I would never have had enough time to finish the PhD without them.

Wissenschaftliche Berichte des Instituts für Meteorologie und Klimaforschung des Karlsruher Instituts für Technologie (0179-5619)

Bisher erschienen:

Nr. 1: *Fiedler, F. / Prenosil, T.*
Das MESOKLIP-Experiment. (Mesoskaliges Klimaprogramm im Oberrheintal).
August 1980

Nr. 2: *Tangermann-Dlugi, G.*
Numerische Simulationen atmosphärischer Grenzschichtströmungen über langgestreckten mesoskaligen Hügelketten bei neutraler thermischer Schichtung.
August 1982

Nr. 3: *Witte, N.*
Ein numerisches Modell des Wärmehaushalts fließender Gewässer unter Berücksichtigung thermischer Eingriffe.
Dezember 1982

Nr. 4: *Fiedler, F. / Höschele, K. (Hrsg.)*
Prof. Dr. Max Diem zum 70. Geburtstag.
Februar 1983 (vergriffen)

Nr. 5: *Adrian, G.*
Ein Initialisierungsverfahren für numerische mesoskalige Strömungsmodelle.
Juli 1985

Nr. 6: *Dorwarth, G.*
Numerische Berechnung des Druckwiderstandes typischer Geländeformen.
Januar 1986

Nr. 7: *Vogel, B.; Adrian, G. / Fiedler, F.*
MESOKLIP-Analysen der meteorologischen Beobachtungen von mesoskaligen Phänomenen im Oberrheingraben.
November 1987

Nr. 8: *Hugelmann, C.-P.*
Differenzenverfahren zur Behandlung der Advektion.
Februar 1988

Nr. 9: *Hafner, T.*
Experimentelle Untersuchung zum Druckwiderstand der Alpen.
April 1988

Nr. 10: *Corsmeier, U.*
Analyse turbulenter Bewegungsvorgänge in der maritimen atmosphärischen Grenzschicht.
Mai 1988

Nr. 11: *Walk, O. / Wieringa, J.(eds)*
Tsumeb Studies of the Tropical Boundary-Layer Climate.
Juli 1988

Nr. 12: *Degrazia, G. A.*
Anwendung von Ähnlichkeitsverfahren auf die turbulente Diffusion in der konvektiven und stabilen Grenzschicht.
Januar 1989

Nr. 13: *Schädler, G.*
Numerische Simulationen zur Wechselwirkung zwischen Landoberflächen und atmophärischer Grenzschicht.
November 1990

Nr. 14: *Heldt, K.*
Untersuchungen zur Überströmung eines mikroskaligen Hindernisses in der Atmosphäre.
Juli 1991

Nr. 15: *Vogel, H.*
Verteilungen reaktiver Luftbeimengungen im Lee einer Stadt – Numerische Untersuchungen der relevanten Prozesse.
Juli 1991

Nr. 16: *Höschele, K.(ed.)*
Planning Applications of Urban and Building Climatology – Proceedings of the IFHP / CIB-Symposium Berlin, October 14-15, 1991.
März 1992

Nr. 17: *Frank, H. P.*
Grenzschichtstruktur in Fronten.
März 1992

Nr. 18: *Müller, A.*
Parallelisierung numerischer Verfahren zur Beschreibung von Ausbreitungs- und chemischen Umwandlungsprozessen in der atmosphärischen Grenzschicht.
Februar 1996

Nr. 19: *Lenz, C.-J.*
Energieumsetzungen an der Erdoberfläche in gegliedertem Gelände.
Juni 1996

Nr. 20: *Schwartz, A.*
Numerische Simulationen zur Massenbilanz chemisch reaktiver Substanzen im mesoskaligen Bereich.
November 1996

Nr. 21: *Beheng, K. D.*
Professor Dr. Franz Fiedler zum 60. Geburtstag.
Januar 1998

Nr. 22: *Niemann, V.*
Numerische Simulation turbulenter Scherströmungen mit einem Kaskadenmodell.
April 1998

Nr. 23: *Koßmann, M.*
Einfluß orographisch induzierter Transportprozesse auf die Struktur der atmosphärischen Grenzschicht und die Verteilung von Spurengasen.
April 1998

Nr. 24: *Baldauf, M.*
Die effektive Rauhigkeit über komplexem Gelände – Ein Störungstheoretischer Ansatz.
Juni 1998

Nr. 25: *Noppel, H.*
Untersuchung des vertikalen Wärmetransports durch die Hangwindzirkulation auf regionaler Skala.
Dezember 1999

Nr. 26: *Kuntze, K.*
Vertikaler Austausch und chemische Umwandlung von Spurenstoffen über topographisch gegliedertem Gelände.
Oktober 2001

Nr. 27: *Wilms-Grabe, W.*
Vierdimensionale Datenassimilation als Methode zur Kopplung zweier verschiedenskaliger meteorologischer Modellsysteme.
Oktober 2001

Nr. 28: *Grabe, F.*
Simulation der Wechselwirkung zwischen Atmosphäre, Vegetation und Erdoberfläche bei Verwendung unterschiedlicher Parametrisierungsansätze.
Januar 2002

Nr. 29: *Riemer, N.*
Numerische Simulationen zur Wirkung des Aerosols auf die troposphärische Chemie und die Sichtweite.
Mai 2002

Nr. 30: *Braun, F. J.*
Mesoskalige Modellierung der Bodenhydrologie.
Dezember 2002

Nr. 31: *Kunz, M.*
Simulation von Starkniederschlägen mit langer Andauer über Mittelgebirgen.
März 2003

Nr. 32: *Bäumer, D.*
Transport und chemische Umwandlung von Luftschadstoffen im Nahbereich von Autobahnen – numerische Simulationen.
Juni 2003

Nr. 33: *Barthlott, C.*
Kohärente Wirbelstrukturen in der atmosphärischen Grenzschicht.
Juni 2003

Nr. 34: *Wieser, A.*
Messung turbulenter Spurengasflüsse vom Flugzeug aus.
Januar 2005

Nr. 35: *Blahak, U.*
Analyse des Extinktionseffektes bei Niederschlagsmessungen mit einem C-Band Radar anhand von Simulation und Messung.
Februar 2005

Nr. 36: *Bertram, I.*
Bestimmung der Wasser- und Eismasse hochreichender konvektiver Wolken anhand von Radardaten, Modellergebnissen und konzeptioneller Betrachtungen.
Mai 2005

Nr. 37: *Schmoeckel, J.*
Orographischer Einfluss auf die Strömung abgeleitet aus Sturmschäden im Schwarzwald während des Orkans „Lothar“.
Mai 2006

Nr. 38: *Schmitt, C.*
Interannual Variability in Antarctic Sea Ice Motion: Interannuelle Variabilität antarktischer Meereis-Drift.
Mai 2006

Nr. 39: *Hasel, M.*
Strukturmerkmale und Modelldarstellung der Konvektion über Mittelgebirgen.
Juli 2006

Ab Band 40 erscheinen die Wissenschaftlichen Berichte des Instituts für Meteorologie und Klimaforschung bei KIT Scientific Publishing (ISSN 0179-5619).

Die Bände sind unter www.ksp.kit.edu als PDF frei verfügbar oder als Druckausgabe bestellbar.

Nr. 40: *Lux, R.*
Modellsimulationen zur Strömungsverstärkung von orographischen Grundstrukturen bei Sturmsituationen. (2007)
ISBN 978-3-86644-140-8

Nr. 41: *Straub, W.*
Der Einfluss von Gebirgswellen auf die Initiierung und Entwicklung konvektiver Wolken. (2008)
ISBN 978-3-86644-226-9

Nr. 42: *Meißner, C.*
High-resolution sensitivity studies with the regional climate model COSMO-CLM. (2008)
ISBN 978-3-86644-228-3

Nr. 43: *Höpfner, M.*
Charakterisierung polarer stratosphärischer Wolken mittels hochauflösender Infrarotspektroskopie. (2008)
ISBN 978-3-86644-294-8

Nr. 44: *Rings, J.*
Monitoring the water content evolution of dikes. (2009)
ISBN 978-3-86644-321-1

Nr. 45: *Riemer, M.*
Außertropische Umwandlung tropischer Wirbelstürme: Einfluss auf das Strömungsmuster in den mittleren Breiten. (2012)
ISBN 978-3-86644-766-0

Nr. 46: *Anwender, D.*
Extratropical Transition in the Ensemble Prediction System of the ECMWF: Case Studies and Experiments. (2012)
ISBN 978-3-86644-767-7

Nr. 47: *Rinke, R.*
Parametrisierung des Auswaschens von Aerosolpartikeln durch Niederschlag. (2012)
ISBN 978-3-86644-768-4

Nr. 48: *Stanelle, T.*
Wechselwirkungen von Mineralstaubpartikeln mit thermodynamischen und dynamischen Prozessen in der Atmosphäre über Westafrika. (2012)
ISBN 978-3-86644-769-1

Nr. 49: *Peters, T.*
Ableitung einer Beziehung zwischen der Radarreflektivität, der Niederschlagsrate und weiteren aus Radardaten abgeleiteten Parametern unter Verwendung von Methoden der multivariaten Statistik. (2012)
ISBN 978-3-86644-323-5

Nr. 50: *Khodayar Pardo, S.*
High-resolution analysis of the initiation of deep convection forced by boundary-layer processes. (2012)
ISBN 978-3-86644-770-7

Nr. 51: *Träumner, K.*
Einmischprozesse am Oberrand der konvektiven atmosphärischen Grenzschicht. (2012)
ISBN 978-3-86644-771-4

Nr. 52: *Schwendike, J.*
Convection in an African Easterly Wave over West Africa and the Eastern Atlantic: A Model Case Study of Hurricane Helene (2006) and its Interaction with the Saharan Air Layer. (2012)
ISBN 978-3-86644-772-1

Nr. 53: *Lundgren, K.*
Direct Radiative Effects of Sea Salt on the Regional Scale. (2012)
ISBN 978-3-86644-773-8

Nr. 54: *Sasse, R.*
Analyse des regionalen atmosphärischen Wasserhaushalts unter Verwendung von COSMO-Simulationen und GPS-Beobachtungen. (2012)
ISBN 978-3-86644-774-5

Nr. 55: *Grenzhäuser, J.*
Entwicklung neuartiger Mess- und Auswertungsstrategien für ein scannendes Wolkenradar und deren Anwendungsbereiche. (2012)
ISBN 978-3-86644-775-2

Nr. 56: *Grams, C.*
Quantification of the downstream impact of extratropical transition for Typhoon Jangmi and other case studies. (2013)
ISBN 978-3-86644-776-9

Nr. 57: *Keller, J.*
Diagnosing the Downstream Impact of Extratropical Transition Using Multimodel Operational Ensemble Prediction Systems. (2013)
ISBN 978-3-86644-984-8

Nr. 58: *Mohr, S.*
Änderung des Gewitter- und Hagelpotentials im Klimawandel. (2013)
ISBN 978-3-86644-994-7

Nr. 59: *Puskeiler, M.*
Radarbasierte Analyse der Hagelgefährdung in Deutschland. (2013)
ISBN 978-3-7315-0028-5

Nr. 60: *Zeng, Y.*
Efficient Radar Forward Operator for Operational Data Assimilation within the COSMO-model. (2014)
ISBN 978-3-7315-0128-2

Nr. 61: *Bangert, M. J.*
Interaction of Aerosol, Clouds, and Radiation on the Regional Scale. (2014)
ISBN 978-3-7315-0123-7

Nr. 62: *Jerger, D.*
Radar Forward Operator for Verification of Cloud Resolving Simulations within the COSMO Model. (2014)
ISBN 978-3-7315-0172-5

Nr. 63: *Maurer, V.*
Vorhersagbarkeit konvektiver Niederschläge: Hochauflösende Ensemblesimulationen für Westafrika. (2014)
ISBN 978-3-7315-0189-3

Nr. 64: *Stawiarski, C.*
Optimizing Dual-Doppler Lidar Measurements of Surface Layer Coherent Structures with Large-Eddy Simulations. (2014)
ISBN 978-3-7315-0197-8

Nr. 65: *Mahlke, H.*
Mechanismen der Auslösung hochreichender Konvektion im südwestdeutschen Mittelgebirgsraum. (2014)
ISBN 978-3-7315-0203-6

Nr. 66: *Fosser, G.*
Precipitation statistics from regional climate model at resolutions relevant for soil erosion. (2014)
ISBN 978-3-7315-0227-2

66

GIORGIA FOSSER

Precipitation statistics from regional climate model at resolutions relevant for soil erosion

Most regional climate models fail in representing convective precipitation, which is responsible for some of the most damaging weather phenomena, like heavy rainfall, large hail, and tornadoes. The parameterisation of convection is known to be a major source of uncertainty and errors as the misrepresentation of the diurnal cycle of summer precipitation. Increasing spatial resolution to the so-called convection-permitting scale allows switching off most of the convective parameterisations. Several studies prove the benefits of this spatial scale, but none of them is available on climatological time-scale (i.e. 30 years). This research bridges the gap between the numerical weather forecast knowledge on convection-permitting scale and real climate scale.

ISSN 0179-5619
ISBN 978-3-7315-0227-2